'Methane oxidation on supported gold catalysts'

Walther, Guido

Publication date:
2008

Document Version
Early version, also known as pre-print

Methane oxidation on supported gold catalysts

Guido Walther

Kongens Lyngby 2008

Preface

This thesis is submitted in partial fulfillment of the requirements for acquiring the PhD degree from the Technical University of Denmark (DTU). The work presented has been carried out at the Center for Atomic-scale Materials Design (CAMD), Department of Physics at DTU from August 2005 to July 2008 under supervision of Professor Sebastian Horch. Co-supervisor was Professor Ulrich Quaade from the Center for Individual Nanoparticle Functionality (CINF), Department of Physics at DTU.

This thesis deals with one of the greatest challenges for scientists in catalysis today —the direct formation of monocarbon oxygenates from methane— and is arranged in five chapters. In the first chapter, the emphasis is put on motivating the work carried out throughout this PhD thesis by introducing methane as a potential fuel and also highlighting heterogeneous catalysis, particularly with regard to methane oxidation on gold. The experimental setups to study the reaction kinetics and the techniques used to characterize the catalyst are described in Chapter 2. Chapter 3 is devoted to the competing side reactions to methane oxidation that take over and lead to full combustion. In Chapter 4, gold is characterized in terms of catalyzing methane oxidation. Finally, a conclusive discussion of the results obtained is given in Chapter 5.

The thesis consists of a summary report and three research articles written during the period 2005 – 2008.

Kongens Lyngby, July 2008

Guido Walther

Abstract

Methane (CH_4), a major compound of natural gas, has been suggested as a future energy carrier. However, it is also known to be a strong greenhouse gas. The use of CH_4 obtained from crude oil as an associated gas is often uneconomical, and it is thus burned off. Avoiding flaring and making the energy stored in the molecule available, is a major research challenge.

In this PhD thesis, CH_4 oxidation on nanoparticular gold is studied both experimentally and theoretically. In the course of this PhD project, CH_4 oxidation was experimentally found more likely to form CO_2 and H_2O than other low index hydrocarbon oxygenates, even at mild conditions (p = 1 bar, $\vartheta \leq 250°C$). This has been taken as an indication that CH_4 oxidation proceeds along a pathway of full combustion. Thus, it was decided to study the tail of the CH_4 oxidation pathway, which is given by CO and H_2 oxidation, in more detailed.

Extensive steady-state activity measurements were performed to obtain the reaction rates for CO and H_2 oxidation. These reactions were studied on three different gold particle sizes using either O_2 or N_2O as oxidation agents. Using particle size distributions obtained from TEM analysis, it was found that the CO oxidation rates follow the d^{-3} relationship proposed in [*Nano Today* **2**, 14 (2007)]. To corroborate the experimental findings, density functional theory (DFT) calculations on the Au$\{532\}$ surface and a Au_{12} cluster, which model corner sites, were used in a microkinetic model. This model reproduced the apparent activation energies for CO oxidation by both O_2 and N_2O. Interestingly, the apparent activation energy for small particles (< 5 nm) is **independent** on both particle size and oxidation agent.

CH_4 oxidation was studied comprehensively on nanoparticular gold under mild conditions (p = 1 bar, 30°C – 250°C). Different apparent activation energies lead to suggest that the barrier for CH_4 oxidation is **dependent** on the particle size. High-resolution TEM images clearly show that irrespectively to the particles size of the catalysts used, the gold particles adhere to the support via their (111) facet. In a similar fashion, CH_4 oxidation was studied with respect to a support effect. From both steady-state activity measurements and high-resolution TEM investigations on the particle's stability, TiO_2 was found to be the most appropriate support material for nanoparticulate gold. The experimental results are corroborated by further DFT calculations investigating the thermodynamics of CH_4 oxidation an a stepped Au$\{211\}$ surface.

These findings show a decrease in the apparent activation energy for CH_4 oxidation on gold as the gold's particle size decreases. For CO and H_2 oxidation, the apparent activation energies were found to be approximately the same. From this, it seems that the reaction of CH_4 oxidation and the oxidation of CO and H_2 occurs on different active sites. Further, if this trend continues for smaller particle sizes, the barrier for CO oxidation may become larger than that for CH_4. This would open a route for partial CH_4 oxidation.

Resumé

Metan (CH_4), en stor bestanddel af naturgas, er blevet foreslået som en fremtidig energibærer. Dog er den også kendt for at være en stærk drivhusgas. Brugen af CH_4 fra råolie som en tilhørende gas er ofte uøkonomisk, og bliver derfor ofte brændt af. En stor udfordring i forskningen er at undgå forbrændingen af CH_4 og i stedet drage nytte af energien lagret i molekylet.

I denne Ph.d. afhandling, bliver oxidation af CH_4 på guld studeret både eksperimentelt og teoretisk. I dette Ph.d. projekt, blev det eksperimentelt fundet at CH_4 oxidation med større sandsynlighed giver kuldioxid og vand end andre lav indeks iltholdige kulbrinter, selv under milde forhold (p = 1 bar, $\vartheta \leq 250°C$). Dette fortolkes som en indikation på at CH_4 oxidation følger en reaktionsvej mod fuld forbrænding. Derfor, skal halen af CH_4 oxidations reaktionsvejen, som er givet ved CO og H_2 oxidation, analyseres detaljeret.

I et detaljeret studie blev ligevægtsaktivitetsmålinger foretaget for at finde reaktionshastigheder for CO og H_2 oxidation. Disse reaktioner blev studeret på tre forskellige størrelser af guldpartikler vha. enten O_2 eller N_2O (lattergas) som oxidationsmidler. Fra Transmissions Elektron Mikroskopi (TEM) analyse følger CO oxidations hastighederne præsenteret det d^{-3} forhold foreslået i [*Nano Today* **2**, 14 (2007)]. For at understøtte de eksperimentelle resultater, blev der anvendt tæthedsfunktionalteori (DFT) beregninger på Au$\{532\}$ overfladen og Au_{12} klynger, som modellerer hjørner, i en mikrokinetisk model. Denne model reproducerer den tilsyneladende aktiveringsenergi og afhænger kun af guldnanopartiklernes størrelse. Interessant er, at den tilsyneladende aktiveringsenergi for små partikler (< 5 nm) er **uafhængig** af både partikelstørrelsen og oxidationsmiddelen.

CH_4 oxidation blev grundigt studeret på guldnanopartikler under milde reaktionsforhold (p = 1 bar, 30°C – 250°C). Forskellige tilsyneladende aktiveringsenergier ledte til at foreslå at barrieren for CH_4 oxidation **afhænger** af nanopartikel størrelsen. Højopløsnings TEM billeder viser tydeligt, at uanset anvendt partikelstørrelse i katalysatorerne, vedhæfter guld partikler til underlaget med (111) facetten nedad. CH_4 oxidation blev studeret på en lignende måde for at at undersøge underlagets effekt. Ved både ligevægtsaktivitetsmålinger og højopløsnings TEM undersøgelser af partiklernes stabilitet blev TiO_2 fundet som det mest velegnede materiale som underlag for guld nanopartikler. De eksperimentelle resultater er endvidere underbygget af DFT beregninger, som undersøger termodynamikken for CH_4 oxidation på en Au$\{211\}$ overflade.

Disse resultater viser en sænkning af den tilsyneladende aktiveringsenergier for CH_4 oxidation på guld eftersom guldets partikel størrelse aftager. For CO og H_2 oxidation blev de tilsyneladende aktiveringsenergier fundet tilnærmelsesvis lige store. Af dette virker det som om, CH_4 oxidation og oxidation af CO og H_2 foregår på forskellige aktive atomare steder. Endvidere, hvis denne tendens fortsætter til mindre partikelstørrelser, kan barrieren for CO oxidation muligvis blive større end den for CH_4. Det ville åben en rute for partielle CH_4 oxidation.

Acknowledgements

I am most grateful to my supervisor, Professor Sebastian Horch, for his open-minded guidance of my research as well as for his straightforward comments. I also owe a debt of gratitude to Professor Ulrich Quaade for all that he has taught me. I would like to acknowledge financial support provided by the Danish Strategic Research foundation and additional support in the form of catalysts that were provided by Project AuTEK.

During this work I have had the pleasure of working with many skillful scientists, without whom this comprehensive study would not have been possible. I am greatly indebted to my co-authors Dr. Glenn Jones, Dr. Duncan J. Mowbray and Tao Jiang for DFT calculations and Dr. Lionel Cervera-Gontard for HR–TEM analysis. It is always a good check of an experiment or an interpretation of an experiment to have a calculation for comparison. My colleagues at CAMD and CINF are thanked for having provided friendly and fruitful working atmospheres.

I also want to thank the staff of the workshop of the physics department, especially Hans Christian Sørensen and Dan Shacham, who have done a great job in precision mechanical manufacturing of new components.

Other people I would gratefully like to acknowledge for linguistic assistance and final proof reading are Dr. Duncan J. Mowbray, Dr. Ifan Stephans, Dr. Shane Murphy and Lasse B. Thomsen. My thanks go to all of you.

Warmest thanks go to my family and friends for their support.

Contents

CHAPTER 1

Introduction

The concept of catalysis dates back to Jöns Jakob Berzelius, who in 1835 introduced the term *catalysis* to describe various reactions that he had observed and realized from a number of isolated observations made by other investigators [1]. Over the last two centuries the field of catalysis has been developed and, since it is of great industrial and environmental importance, it has afforded three Nobel prizes: 1909 for Friedrich Wilhelm Ostwald, 1932 for Irving Langmuir and 2007 for Gerhard Ertl.

Besides the many catalyzed industrial processes, there are several other reactions to which no appropriate catalyst is commercially available. These include the direct oxygenation reactions of methane to methanol and to formaldehyde. This is due to the high stability of the methane molecule.

Within the last two decades gold has attracted much of attention in the field of catalysis. Beyond CO oxidation, that is usually applied as a test reaction, gold also shows activity for other reactions. In theory, the activity exhibited by a gold surface in adsorbing molecules is related to only two factors [2]. Thus one could inquire, whether gold is an appropriate catalyst for methane oxidation as well.

This chapter briefly introduces catalysis by gold for methane oxidation. Reasons are then given at to why there is a keen interest in converting methane into other —higher value— chemicals.

1.1 Heterogeneous Catalysis

Today, catalysis plays a key role in industry and daily life. Most chemical reactions, either for the synthesis of chemicals or for the conversion of environmentally unfriendly gases, are accelerated by using a catalyst. Perhaps the best known example is the catalytic converter of fossil fuel powered vehicles.

The general mode of action of a catalyst is based on the adsorption of one or more reactants, e.g. A and B. In heterogeneous catalysis, from now on only catalysis, these then form after dissociation an intermediate on the surface AB* that subsequently gives the final reaction product AB. The overall chemical reaction may be given by

$$\mathrm{A} + \mathrm{B} \quad \longrightarrow \quad \mathrm{AB}. \tag{1.R1}$$

When the product desorbs from the surface, the process regenerates the catalyst. The entire process can then be written in its elementary steps, where * denotes a free active site:

$$\mathrm{A} + * \quad \underset{k_1^-}{\overset{k_1^+}{\rightleftharpoons}} \quad \mathrm{A}* \tag{1.R1a}$$

$$\mathrm{B} + * \quad \underset{k_2^-}{\overset{k_2^+}{\rightleftharpoons}} \quad \mathrm{B}* \tag{1.R1b}$$

$$\mathrm{A}* + \mathrm{B}* \quad \underset{k_3^+}{\longrightarrow} \quad \mathrm{AB}* + * \tag{1.R1c}$$

$$\mathrm{AB}* \quad \underset{k_4^+}{\longrightarrow} \quad \mathrm{AB} + * \tag{1.R1d}$$

Thus, a good catalyst must neither bind the reactants nor the product too tightly. This basically means that a catalyst only affects the kinetics of a chemical reaction that is in equilibrium. An energetically unfavorable reaction will —due to thermodynamics— still be unfavorable in the presence of a catalyst.

1.1.1 Concept of Catalysis

For the elementary steps (1.R1a) and (1.R1b) listed at the beginning of this Section, it has been assumed that the adsorbates and the surface are in thermal equilibrium before they react to form AB*. According to the Langmuir–Hinshelwood formalism, the reaction rate r for (1.R1a) can then be formulated in the rate equation

$$r = k_1^+ p_\mathrm{A} \theta_* - k_1^- \theta_\mathrm{A}. \tag{1.1}$$

Here, k_1^+ and k_1^- denote the forward and the backward rate constants, respectively, p_A the pressure of species A in the gas phase, θ_* the coverage of unoccupied active sites and θ_A the fraction of

sites with specie A adsorbed. Assuming that the reaction product desorbs quickly, meaning that (1.R1d) proceeds fast, it follows that (1.R1c) is the rate determining step of the reaction. Hence, bearing these assumptions in mind, the reaction rate of the entire reaction is given by

$$r \approx \frac{k_3^+ \, K_1 K_2 \, p_\mathrm{A} \, p_\mathrm{B}}{(1 + K_1 \, p_\mathrm{A} + K_2 \, p_\mathrm{B})^2}, \tag{1.2}$$

with the equilibrium constants $K_i = k_i^+ \,/\, k_i^-$ for the species $i \in \{\mathrm{A}, \mathrm{B}\}$.

Setting aside the kinetic picture that has been used to introduce the concept of catalysis, it shall henceforward be focused on the potential energy picture (Figure 1.1) and how these two concepts are correlated with each other.

A reactant that approaches a surface and binds to it will equilibrate with the surface. This means that the potential energy of the adsorbate reaches a minimum. In Figure 1.1 this is illustrated by the quantum well of the initial state. The other quantum well indicates the final state of a reaction product that may still be adsorbed on the surface after reaction. The reaction itself is associated with an energy barrier, that assigns a transition state at its apex. To let the reaction proceed along the reaction coordinate, an activation energy $E_\mathrm{a} = E_\mathrm{TS} - E_\mathrm{IS}$ is required to overcome this barrier.

In terms of kinetics, the initial and final state are assumed to be in equilibrium with the transition state. For the elementary step (1.R1c), this may be expressed as $\frac{\mathrm{d}}{\mathrm{d}t}\theta_{\mathrm{AB_{TS}}^{**}} = 0$. The forward rate constant k_3^+ can be found to be

$$k_3^+ = \frac{k_\mathrm{B} \, T}{h} \, \frac{q_{\mathrm{AB_{TS}}^{**}}}{q_{\mathrm{A}^*} \, q_{\mathrm{B}^*}} \, \mathrm{e}^{-E_\mathrm{a} \,/\, k_\mathrm{B} \, T}, \tag{1.3}$$

by applying transition state theory [3]. The pre-exponential factor of the Arrhenius-like Equation (1.3) refers to the partition functions q_i of the intermediate $\mathrm{AB}_{TS}{}^{**}$ in the transition state and those of the adsorbed reactants A* and B*. Additionally, the Arrhenius equation gives the temperature dependence of the rate constant and makes it possible to compare rates from theoretical

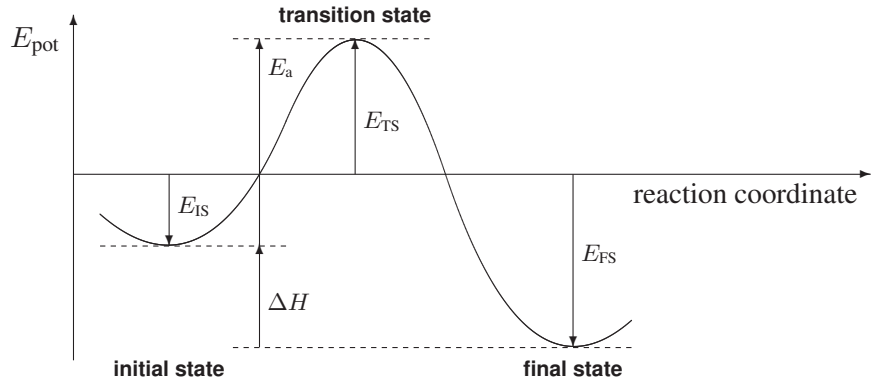

Figure 1.1: Potential energy diagram of an elementary step: the quantum wells illustrate the binding energies for the initial state and the final state. The transition state in between marks the barrier for the reaction to proceed via the reaction coordinate. A measure of the driving force for a reaction is the enthalpy ΔH.

expressions with experimental data.

Including the backward rate constant k_3^- to determine the equilibrium constant K_3, it becomes clear that the energy difference between the initial state and the final state —namely the reaction enthalpy ΔH— is a measure of the driving force for the reaction. This cannot be changed by the catalyst, since

$$K_3 \equiv \frac{k_3^+}{k_3^-} = \frac{q_{\mathrm{AB}*}}{q_{\mathrm{A}*}\, q_{\mathrm{B}*}}\, \mathrm{e}^{\Delta H \,/\, k_\mathrm{B} T} = \mathrm{e}^{\Delta S \,/\, k_\mathrm{B}}\, \mathrm{e}^{\Delta H \,/\, k_\mathrm{B} T}. \tag{1.4}$$

A third approach for introducing catalysis uses the picture of chemical bonding. This picture is the key to understand catalysis in terms of orbital theory. It is based on the d band model [4] that links together changes in the electronic structure of transition metal surfaces with changes in the chemical reactivity.

It begins with the adsorbate-surface interaction, when an adsorbate approaches a transition metal surface and forms a chemical bond. This is illustrated schematically in Figure 1.2. First, when the adsorbate valence levels interact with the metal s states, the sharp atomic states of an adsorbate in gas phase are broadened and shifted down. These renormalized states interact then with the narrow d band of the transition metal and form covalent bonding and antibonding states. These states are below and above the initial adsorbate and surface state, respectively. From this picture, the binding energy ΔE of a chemical bond may be determined by contributions from a coupling with the broad metal s band and with the narrow d band [4],

$$\Delta E_{\mathrm{bond}} = \Delta E_s + \Delta E_d. \tag{1.5}$$

Even though the main contribution is associated with the coupling to the metal s band, the vari-

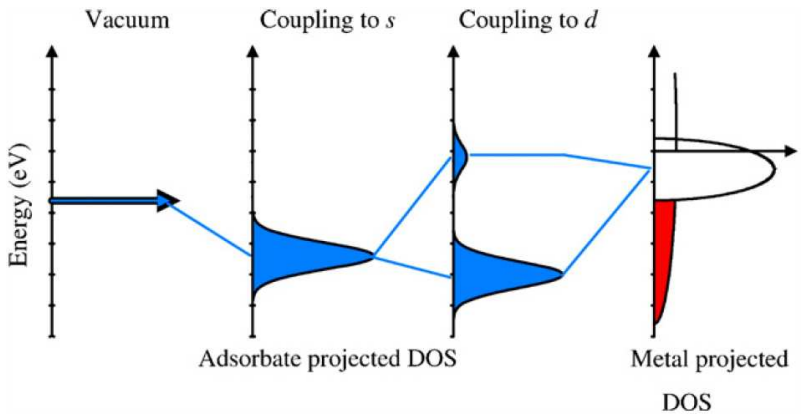

Figure 1.2: Schematic illustration of the energy levels for an adsorbate away from the surface (in vacuum), when it couples to the *s* orbital and to the *d* states as well as the partly filled *d* band of the transition metal. Adopted from [5].

ation of d band accounts for the variation in binding energy, when going from one element to the next in the Periodic Classification. This may in fact be assumed since most of the d elements have a half filled s band. Thus any contribution from s electrons is in the first approximation constant [6].

The small perturbation of the binding energy caused by the coupling of the adsorbate states to the metal d band is, according to the d band model, dependent on a few parameters:

1. The degree of filling f of the d band,
2. The coupling matrix element between the adsorbate and the surface states V_{sd},
3. The energy difference between the energy levels of the adsorbate states and the center of the d band, $\varepsilon_\mathrm{a} - \varepsilon_\mathrm{d}$.

The latter point becomes more clear when considering the case in which an adsorbate couples to a specific kind of transition metal atom. Then, ε_a and V_{sd} are constant; only the density of states projected onto the metal atoms that are in contact with the adsorbate, $n_d(\varepsilon)$, will vary. Thus, the center of the d band, ε_d, is deemed to be a simple descriptor for the variations in the adsorption energies. Hence, the energy contribution to a chemical bonding from the sd coupling of an adsorbate to a d metal surface is given by

$$\Delta E_d = -(1-f)\frac{2V_{sd}^2}{\varepsilon_\mathrm{a} - \varepsilon_\mathrm{d}} + 2(1+f)\alpha V_{sd}^2. \tag{1.6}$$

The first term is attractive while the last one represents the repulsion, in which α denotes the overlap matrix element [2, 4].

Variations in the center of the d band are often coupled to variations in shape and width of the projected density of d states, $n_d(\varepsilon)$. For example, when considering tensile strain at the d metal surface, the coupling, V_{dd}, of the metal d states to the neighboring metal d states is smaller. This leads to a decrease in the band width ($W \sim \mid V_{dd} \mid$). To maintain the number of d electrons when the band width shrinks, the d band center, ε_d, needs to be shifted up (*cf.* Figure 1.3). This leads to a stronger interaction with an energy level of an adsorbate and thus to a stronger chemisorption bond. In a similar fashion it may be argued that a shrinking of the band width occurs when the

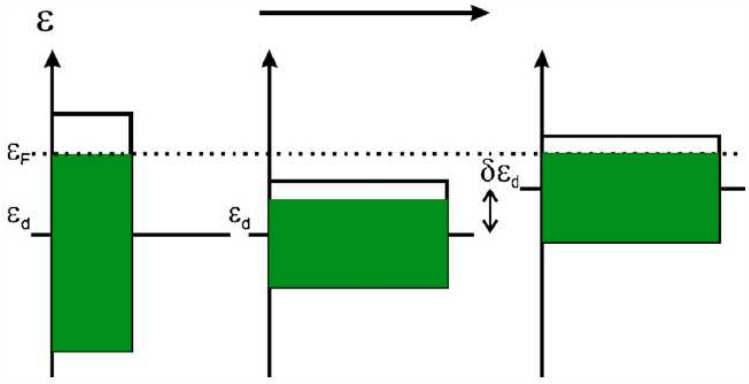

Figure 1.3: Illustration of the correlation between the center of the *d* band, ε_d, and the band width *W* of a transition metal. Adopted from [5].

number of neighboring atoms is reduced. This is the case at low coordination sites, such as steps, edges, corners and kinks.

1.1.2 Properties of a Catalyst

Activity, stability and selectivity are the properties of a catalyst that are used to describe how suitable a catalyst is for an industrial process. Not all of these have the same impact, while the financial aspects also play a key role. Thus, selectivity has highest priority in industry, simply because byproducts are unwanted and often expensive to remove post-reaction. With respect to running expenses and perhaps amortization costs for a catalyst that are given by the catalyst's lifetime, stability is the next most important issue for industry to choose when considering whether a certain material will be used as catalyst for an industrial process or not. However, the activity of a catalyst is of minor importance, since a required product yield may still be realized by scaling-up a reactor of a plant.

The selectivity of a reaction is a measure of the preference of a catalyst for one reaction proceeding over others that cause side reactions and form byproducts. For a desired product P, the selectivity S_P is given by the fraction of the mol-volume of product P to the sum of the mol-volumes of all the products,

$$S_\mathrm{P} = \frac{V_\mathrm{P}}{\sum_i V_i}. \tag{1.7}$$

For industrial processes it is thus of great importance to aim for a selectivity $S_\mathrm{P} = 1$.

A catalyst can be affected by chemicals, e.g. decomposition or poisoning, thermally or even mechanically. These effects may have an influence on the size and shape of catalytic active nanoparticles through sintering, for example. In the case of both sintering and poisoning, an accompanying deactivation determines the lifetime and thereby the stability of a catalyst.

The activity characterizes how fast a reaction proceeds in the presence of a catalyst. This may, for example, be expressed by the reaction rate r that is determined by the quantity of products formed per unit of catalyst mass and time. Comparing different catalysts, there is a keen interest in normalizing the quantity of products converted to the number of active sites rather than the catalyst mass, which is called turn over frequency (TOF). But even though the TOF is a more sophisticated way to express the activity of a catalyst, many prudent scientists omit reporting a TOF, because the rate may have been changed due to mass or heat transfer [7]. Moreover, the identification of the active sites is not trivial, and is the subject of ongoing debate. Instead, the activity of a catalyst may instead be expressed by the rate constant k and the activation energy E_a, as defined in (1.3).

1.1.3 Accompanying Limitations of a Catalyst

During operation, a catalyst can easily run into limitations. To avoid this, the reactions (1.R1a) – (1.R1d) shall again be considered. These represent in a more sophisticated way the catalytic cycle

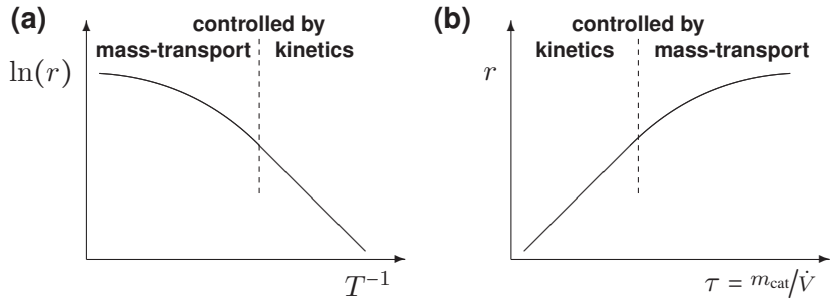

Figure 1.4: Parameters that control the mode of operation of a catalyst: (a) Arrhenius plot illustrates that heat supplied results in more heat that leads the catalyst to be run under mass-transport control. (b) A catalyst behaves in similar fashion, when increasing the amount of active material m_{cat} or decreasing the flow rate of the products $\dot{V}$. τ represents the contact time of an adsorbate with an active site. Adapted from [8].

for the reaction of A + B $\longrightarrow$ AB.

When a catalyst is being operated in a regime that is close to the condition at which self-ignition of the reaction occurs, the catalyst inevitably runs *mass-transport controlled*. At this point the conversion reaches 100 % and in the Arrhenius plot saturation occurs in the reaction rate. This, illustrates the inefficient use of a catalyst, *cf.* Figure 1.4(a). A mass-transport controlled regime also appears when the reaction product does not desorb at a sufficent rate. The surface of the catalyst bacomes inactive while active sites are vacant [8]. Other parameters that lead a catalyst to run into mass-transport controlled conditions are the flow rate of the products $\dot{V}$ and the the amount of active material m_{cat}, which determine the contact time τ of an adsorbate with an active site. The relationship to the reaction rate is illustrated in Figure 1.4(b).

With the assumptions made at the beginning of this chapter, the catalyst has already been considered to be operated under *kinetic control*. Even though it might be more desirable to run a catalyst under conditions that allow one to achieve a conversion close to 100 %, it is in fact more common to choose a kinetically controlled regime. Thus it was tried in all experiments presented to keep the conversion below the point of self-ignition.

1.2 General Aspects of Methane

Oil, natural gas and coal are our primary fossil fuels. All of these are mixtures of hydrocarbons, indicating that their compounds are composed of carbon and hydrogen. Natural gas consists mainly of methane (CH_4), the simplest saturated alkane, with only one carbon atom and four hydrogen atoms that are bonded to it forming a tetrahedral molecule. Natural gas also contains higher homologous alkanes (ethane, propane, butane). Since natural gas comes from different types of wells (oil wells, gas wells, and condensate wells), the CH_4 concentration depends on the location where it is exploited. For gas wells the CH_4 concentration is 80–90% [9].

Table 1.1: Comparison of hydrocarbons' H : C ratio

Methane (CH_4)	4.0
Natural gas[†]	3.8
Ethane (C_2H_6)	3.0
Propane (C_3H_8)	2.7
Butane (C_4H_{10})	2.5
Ethene (C_2H_4)	2.0
Petroleum crude[†]	1.8
Tar sand bitumen[†]	1.5
Bituminous coal[†]	0.8

[†] taken from [9]

1.2.1 Properties of the Simplest Hydrocarbon

Since CH_4 is a very stable molecule, a temperature of 782°C is required to decompose CH_4 into its elements. On the other hand, for liquefaction CH_4 needs to be cooled to its boiling point at $-164°C$ at a pressure of one atmosphere [10].

Comparing the elemental composition of higher saturated alkanes (C_nH_{2n+2}) or even unsaturated hydrocarbons such as alkenes (C_nH_{2n}) or cyclic hydrocarbons (benzene) with CH_4, it is obvious that CH_4 is a much more suitable fuel source concerning its higher atomic ratio of H : C, *cf.* Table 1.1. In fact this is obvious, since burning CH_4 produces less CO_2 for each unit of heat released. For full combustion,

$$CH_4 + 2\,O_2 \longrightarrow CO_2 + 2\,H_2O, \tag{1.R2}$$

the liberated heat of reaction is $\Delta H^0 \approx$ -802.3 kJ mol^{-1}. Although this is less energy than any other hydrocarbon releases, due to the small molecular mass of CH_4 (16 g mol^{-1}), it actually yields the greatest amount of heat per unit mass.

1.2.2 Methane – Pollutant, Fuel or Feedstock

Natural gas that comes along with oil, is termed 'associated gas' [11]. Although separation is practiced, natural gas needs to be shipped in a liquified state of aggregation. Since these natural gas sources are so remote from the consumers, transportation of LNG (liquified natural gas) is often uneconomical. This is due to the fact that CH_4 has such a low boiling point. Instead, natural gas is usually flared. With more than 20 billion cubic meters burned annually, this practice has a significantly detrimental effect on the environment [12]. However, this is less harmful to the environment than to let CH_4 simply escape into air, because CH_4 is a more than 20 times stronger greenhouse gas than CO_2.

With the growing demand for energy, especially for transportation, hydrocarbons and their transformations play a major role in our everyday life. With diminishing oil resources, CH_4 has been proposed to be a feedstock for alternative fuels, such as methanol (CH_3OH) [13] and dimethyl ether (DME) [14]. Bioethanol (C_2H_5OH) has also been proposed as an alternative fuel, but since it can be synthesized by the fermentation of biomass [15], it will not be considered in more detail. CH_3OH is the raw material for many chemicals, including DME, and is one of the seven building blocks of the organic chemical industry [16].

Considering energy sources beyond fossil fuels, it is clear that even if at some point in the future the natural gas reservoirs are running empty, CH_4 can still be synthesized from renewable energy sources, such as biomass. Thus, there is a keen interest in finding a good catalyst for converting CH_4 into higher value chemicals [17, 18].

1.2.3 Oxidation of Methane

The conversion of CH_4 into higher value chemicals presents two main challenges. First, the oxygenation products are more reactive than CH_4 itself, and second, the most favorable reaction proceeds by complete combustion into CO_2 and H_2O, as may be seen from the enthalpies ΔH^0 in (1.R3) – (1.R6).

$$\mathrm{CH_4 + \tfrac{1}{2}\,O_2 \longrightarrow CH_3OH;} \qquad \Delta H^0 \approx -126.4\ \mathrm{kJ\ mol^{-1}} \tag{1.R3}$$

$$\mathrm{CH_4 + \ \ O_2 \longrightarrow HCHO + 2\,H_2O;} \qquad \Delta H^0 \approx -284.2\ \mathrm{kJ\ mol^{-1}} \tag{1.R4}$$

$$\mathrm{CH_4 + \tfrac{3}{2}\,O_2 \longrightarrow CO + 2\,H_2O;} \qquad \Delta H^0 \approx -519.3\ \mathrm{kJ\ mol^{-1}} \tag{1.R5}$$

$$\mathrm{CH_4 + 2\,O_2 \longrightarrow CO_2 + 2\,H_2O;} \qquad \Delta H^0 \approx -802.3\ \mathrm{kJ\ mol^{-1}} \tag{1.R6}$$

However, currently the most widely used process to form CH_3OH proceeds via highly endothermic steam reforming of CH_4 over a Ni catalyst to first form synthesis gas that is then hydrogenated over a Cu/ZnO catalyst. Both catalysts are supported by Al_2O_3. In the second step it is mainly CO_2 that forms CH_3OH and H_2O via the $\Delta H^0 \approx$ -49.5 kJ mol^{-1} exothermically driven reverse CH_3OH steam reforming reaction [19]. About one third of the annual CH_3OH production is needed to respond to the HCHO demand. However, HCHO is finally made by oxidative dehydrogenation of CH_3OH over a granular crystalline Ag catalyst. Equation (1.R7) illustrates the entire process. This is indeed inefficient in the sense that CH_4 is first oxidized, then reduced and finally oxidized again to form HCHO.

$$\mathrm{CH_4} \xrightarrow[\mathrm{Ni}]{\mathrm{H_2O}\ \searrow\ \nearrow\ 3\,H_2} \{\mathrm{CO, CO_2}\} \xrightarrow[\mathrm{Cu/ZnO}]{3\,\mathrm{H_2}\ \searrow\ \nearrow\ \mathrm{H_2O}} \mathrm{CH_3OH} \xrightarrow[\mathrm{Ag}]{1/2\,\mathrm{O_2}\ \searrow\ \nearrow\ \mathrm{H_2O}} \mathrm{HCHO} \tag{1.R7}$$

A more efficient process would be the direct formation of CH_3OH or even HCHO from CH_4. Unfortunately, no good catalyst is known so far that satisfies the requirements for direct CH_3OH

production on a large scale. Therefore, oxidation of CH_4 into monocarbon oxygenates is considered to be one of the greatest challenges for scientists in catalysis.

Many attempts have been undertaken to find an appropriate catalyst for partial CH_4 oxidation and these have been reviewed in quite detail [18, 20]. An early work that was already carried out and patented by Dowden *et al.* in 1971, showed a very high selectivity for CH_3OH over a $(MoO_3)_3{\cdot}Fe_2O_3$ catalyst at about 50 bar and a temperature of between 430°C and 500°C. However, the conversion was too poor to achieve a breakthrough [21].

A more recent theoretical study focuses on CH_4 oxidation on MoO catalysts [22]. Therein, peroxide species adsorbed on reduced MoO centers were identified to react with CH_4 to form HCHO. Vanadium, as another representative d element with a less than half filled d band, was used in a V_2O_5 catalyst and shown to be active for CH_4 oxidation as well. The selectivity to HCHO was reported to be accompanied by a very low conversion [23].

Further investigations on a number of noble metal based catalysts have been carried out to determine their potential for the partial oxidation of CH_4 to CO and H_2. Between 300°C and 500°C, extinction and ignition temperature rates as well as selectivities were reported to be identified [24]. A few yeas ago, Iglesia *et al.* studied the reaction of different gas mixtures containing CH_4, CO_2 and labeled CO over supported Pt clusters [25]. Since identical ^{13}C fractions in CO and CO_2 were determined at temperatures in a range of 600°C – 800°C, Iglesia *et al.* concluded that CO_2 activation is quasi-equilibrated and kinetically irrelevant. In contrast, recent studies suggest that the mechanism of CH_4 reforming is condition-dependent: At lower temperatures CO formation is dominant, while at higher temperatures CH_4 activation takes over [26].

In 2006, Hutchings *et al.* reported alkane combustion on reduced metal oxide supported Au catalysts. Since Au/CoO_x did not show a deactivation after 48 h, that catalyst was proposed to be the most promising one, even though it is more favorable to catalyze CO oxidation. In that study it was also pointed out that CO and alkane oxidation take place on different active sites [27].

From calculations based on density functional theory (DFT), the formation of CH_xO species on $Ni\{111\}$ facets was found. On that catalyst, CH_3OH dissociates catalytically —as with the catalysts discussed above— at lower temperatures than partial CH_4 oxidation occurs. However, the calculations showed that when Ni was alloyed with Au the formation of CH_3OH is promoted [28].

1.3 Catalysis by Gold

At a first glance, the nobility of gold would intuitively suggest that it would be a poor catalyst. Since gold is the only metal with an endothermic chemisorption energy, it does not even adsorb reactive molecules such as O_2 [29]. From the basic concepts of catalysis, adsorbates are required to

be able to bind to the catalyst's surface. Thus gold has to be made less noble. In point of fact, when gold is nanosized it shows activity for CO oxidation and many other reactions that have a strong tendency towards CO_2 formation. With focus on the physical and chemical properties of gold, a thorough understanding of the nature of gold's catalytical properties shall now be presented.

1.3.1 Properties of Gold

Gold exhibits a quite unique character that has fascinated mankind over millennia. For example its color, no other metal has such a beauty. Gold together with copper and silver, which are referred to as the coinage metals, share the 11th group of the Periodic Classification. Another property of gold is it ability to form both aurous compounds (Au^{I}) and auric complexes (Au^{III}), something that no other coinage metal can do. Both pure gold and very stable aurous and auric alloys may be found in nature [30]. Due to the rareness of gold (approximately 3 ppb in the earth's crust), it is known to be a precious metal and therefore mainly used as bullion and in jewelry. Besides that, gold is used for medical instrumentation and in electronic devices. It has both a high thermal and electrical conductance. Also unique is the inertness of gold. Moisture, oxygen and ordinary acids do not affect gold at all, but it can be attacked by halogens and does not resist aqua regia, the only acid that is able to dissolve the *king* of the metals.

In 1988, Pyykkö *et al.* showed that several of these phenomena are assigned to a relativistic effect on the mass of the $1s$ electrons. For heavier elements the relativistic effect leads in addition to the lanthanide contraction to orbital contraction and consequently to shrinking of the outer s and to a lesser extent of the p shells as well, on the other hand the d and f electrons are not significantly affected [31]. This effect is very pronounced for gold and allows optical transitions from the $5d$ level to the (essentially $6s$) Fermi level at $h\nu$ = 2.38 eV (521 nm) that corresponds to the characteristic yellow color [31] as well as stabilizing the higher oxidation states +III and +V of gold [32, 33]. However, a comparison of the coinage metals with the superheavy element 111, röntgenium (Rg), shows that with an even larger relativistic effect even the electronic configuration from completely filled d orbitals of the coinage metals changes to $6d^9 7s^2$ for Rg [8, 34]. Finally, the atomic radius of the elements increases down the groups of the Periodic Classification, but Pt and Au are exceptions to this trend — again a result of a relativistic effect, *cf.* Figure 1.5.

Hammer and Nørskov [2] demonstrated a concept that enables us to illustrate the nobleness of gold in terms of its ability to only make a weak coupling between the electronic states of an adsorbate and the metal d band. From the d band model [4], introduced in Section 1.1.1, the bonding energy E_{bond} for any atomic adsorbate on gold is given by

$$E_{\text{bond}} = E_s - (1 - f)\frac{2V_{sd}^2}{\varepsilon_{\text{a}} - \varepsilon_{\text{d}}} + 2(1 + f)\alpha V_{sd}^2. \tag{1.8}$$

The latter (repulsive) term weakens the bonding when the degree of filling increases and it thus dominates the contribution of the d band to the bonding [3]. With a view to gold, it can be concluded that besides vanishing the attractive term in (1.8) due to a completely filled d band, the d orbitals become more localized on the atom. The overlap of d orbitals then increases and they thus behave more like core levels. Hence they do not take part in chemistry that happens on the surface.

Another parameter that illustrates the nobleness of d metals is the cohesive energy. It is a measure of the energy required to remove one atom from the solid. For d elements such as Ir or Pt, the cohesive energy is largest. As a function of the filling degree its maximum lies at elements which have only a half filled d band. In this particular behavior the cohesive energy follows the same trend as the melting point [3], which becomes of importance when discussing stability.

To illustrate that gold is outstanding in the Periodic Classification, the properties discussed above, are summarized in Figure 1.5 for ease of comparison.

1.3.2 On the Path towards Catalysis by Gold

In the past, gold was not believed to be catalytically active, and was even called "the noblest of all the metals" [2]. However, the discovery by Haruta *et al.* [37] that nanoparticulate gold is catalytically active for CO oxidation, provoked an academic *gold rush*. This is evidenced by the

[Ar]$3d^6 4s^2$	[Ar]$3d^7 4s^2$	[Ar]$3d^8 4s^2$	[Ar]$3d^{10} 4s$	[Ar]$3d^{10} 4s^2$
6 3 2 0 -2	5 4 3 2 1 0 -1	4 3 2 1 0 -1	4 3 2 1	2
4.28 1.59 -6.30	4.39 1.34 -5.07	4.44 1.16 -3.90	3.49 1.00 -2.51	1.35 0.46 n.a.
$_{26}$**Fe** 1808 7.87	$_{27}$**Co** 1768 8.89	$_{28}$**Ni** 1726 8.91	$_{29}$**Cu** 1356.6 8.92	$_{30}$**Zn** 692.73 7.14
bcc 124.1	hcp 125.3	fcc 124.6	fcc 127.8	hcp 133.5
[Kr]$4d^7 5s$	[Kr]$4d^8 5s$	[Kr]$4d^{10}$	[Kr]$4d^{10} 5s$	[Kr]$4d^{10} 5s^2$
8 6 4 3 2 0 -2	5 4 3 2 1 0	4 3 2 0	3 2 1	2 1
6.74 3.87 -4.62	5.75 3.32 -4.03	3.89 2.78 -1.20	2.95 2.26 -0.65	1.16 1.58 n.a.
$_{44}$**Ru** 2583 12.45	$_{45}$**Rh** 2239 12.41	$_{46}$**Pd** 1825 12.02	$_{47}$**Ag** 1235.1 10.49	$_{48}$**Cd** 594.1 8.64
hcp 132.5	fcc 134.5	fcc 137.6	fcc 144.5	hcp 148.9
[Xe]$4f^{14} 5d^6 6s^2$	[Xe]$4f^{14} 5d^7 6s^2$	[Xe]$4f^{14} 5d^9 6s$	[Xe]$4f^{14} 5d^{10} 6s$	[Xe]$4f^{14} 5d^{10} 6s^2$
8 6 4 3 2 0 -2	6 4 3 2 1 0 -1	6 5 4 2 0	5 3 2 1 -1	2 1
8.17 5.13 n.a.	6.94 4.45 -4.65	5.84 3.90 -2.17	3.81 3.35 +0.54	0.67 2.64 n.a.
$_{76}$**Os** 3318 22.61	$_{77}$**Ir** 2683 22.65	$_{78}$**Pt** 2045 21.45	$_{79}$**Au** 1337.6 19.32	$_{80}$**Hg** 234.28 13.55
hcp 133.8	fcc 135.7	fcc 137.3	fcc 144.2	rhomb 150.3

Figure 1.5: Extraction of the Periodic Table with a focus on gold, its vicinity and other elements that are of importance in catalysis. Physical and chemical properties of the elements are included as well as the important factors that describe nobleness, as discussed in the text. The filling degree of the *d* band may be taken from the electronic configuration. The data is taken from: electronic configuration [35], oxidation state [30, 35], cohesive energy E_{coh} [36], coupling matrix element V_{sd}^2 relative to Cu [4], chemisorption energy E_{chem} [29], melting point T_{melt}, density ρ, atomic radius r_{atom} [10] and structure [30], as shown to the right.

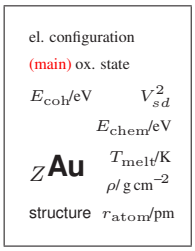

exponential increase in publications on catalysis by gold since the early 1990s [8, 29, 38, 39].

Several experimental studies have been performed to understand gold's activity for CO oxidation. These investigations span changes of the particle's morphology [40, 41], a structure–activity relationship [42, 43, 44], the activity of unsupported nanoporous bulk gold [45, 46] and the influence of the support on the activity [47]. CO oxidation has also been used as a test reaction in many intensive theoretical studies based on density functional theory (DFT) [2, 29, 48, 49, 50, 51, 52, 53]. Besides CO oxidation, many other reactions have been studied on gold catalysts, including the oxidation of hydrocarbons [8, 27, 54, 55, 56, 57] and oxygen-containing hydrocarbons [8, 38, 39, 54, 58] as well as the catalysis of hydrogenation of unsaturated organic compounds [8, 39, 59].

The reason for this surprising activity is still under debate: After the pioneering work of Haruta [60], the activity of gold has been linked to several different effects, e.g. a quantum-size effect [42], support-induced strain [48], charge transfer from the small gold particles to adsorbed oxygen [61] and the role of low-coordinated gold atoms [29, 48, 50, 51, 52, 53]. It is clear from these alternative perspectives that more work is required to find the definitive answer to this debate. However, it is entirely probable that any of the perspectives are correct under a given set of reaction conditions, and that the reported results are sometimes the results of experimental or theoretical conditions and the probe being used.

Different mechanisms for the CO oxidation reaction have been proposed to explain the effects observed. Mechanisms that involve the support material are a perimeter model in which the gold is assumed to be all over in a metallic state [60, 62, 63], and the so-called Bond–Thompson model in which gold is deemed to be cationic [64]. According to both concepts, the adsorbates meet and react at the periphery of the gold particle. Another mechanism that only considers the gold itself as the catalyst, is based on a metastable CO—O_2 intermediate instead of first dissociating O_2 into highly reactive atomic O [65]. This alternative pathway was originally proposed by Liu *et al.* in 2002 [49]. From that, Hu *et al.* proposed recently a catalytic cycle where the reaction via the metastable CO—O_2 intermediate proceeds at the Au–TiO_2 interface [66]. In this model O_2 is bonded to the support.

However, Nørskov *et al.* have recently shown that gold particle activity on different supports for CO oxidation follows a $1/d^3$ relation [51]. This strongly suggests that the CO oxidation reaction tends to occur at corner sites on small gold nanoparticles (d < 5 nm). During the last half decade the original picture has been corroborated by many other experimental and theoretical studies [29, 44, 52, 53].

Another issue when using gold as a catalyst is the stability of nanoparticulate gold. Since gold has a low melting point, gold nanoparticles become mobile even at low temperatures [67, 68, 69], and are observed to sinter into larger particles [68]. An effective support which is able to keep the gold particles well dispersed is TiO_2. However, more study is needed to understand how this works, and to comprehend fully how the particles change during reactions.

CHAPTER 2

Experimental Equipment

This study deals with synthesizing and characterizing gold catalysts, which were then tested experimentally in terms of their catalytic activity for CH_4 oxidation. Various gold catalysts were prepared, either by chemical methods such as deposition-precipitation of unconjugated gold colloids on anatase TiO_2 powder, or by physical methods to deposit size selected nanoparticles into microreactors using a cluster source. In microreactors, the catalysts were exposed to the reactants, which were supplied and controlled in gas flow by mass flow controllers. The reaction products were analyzed either using a gas chromatograph or by mass spectrometry. Before and after these experiments on the catalytic activity, the size and shape of the gold particles were characterized using transmission electron microscopy (TEM). To ensure results that are based on impurity-free samples, the catalysts were subjected to an examination for elemental analysis using X-ray fluorescence (XFR).

This chapter is devoted to the preparation of the gold catalysts, the instrumentation used and the methods used to characterize and to test the catalysts. The concept of microreactors is defined as well as the arising question, *i.e.* whether this technique is academic.

2.1 Preparation of Gold Catalysts

Commercial gold catalysts as well as "home-made" powder catalysts produced in the laboratory were tested. 2.0 nm AURO*lite*™ gold catalysts from AuTEK [70] and 3.3 nm gold reference catalysts from the World Gold Council [71] were used as representatives of catalysts that are commercially available. These catalysts have a gold concentration of between 1.0 wt% and 1.5 wt%.

Larger gold particles were prepared by deposition-precipitation of unconjugated 5.0 nm gold colloids (Ted Pella, Inc.) on anatase TiO_2 powder (Millennium Inorganic Chemicals). For ease of comparison, the gold concentration of the in-house catalysts was carefully adjusted to those of the commercially available samples. The preparation was performed at $\vartheta \leq 50°C$ to evaporate the solvent. After the catalyst had been dried, it was calcined at 200°C.

2.2 The Experimental Setup

The experimental setup was based on a micro-fabricated continuous flow reactor, that was connected to a gas supply and various analysis methods. For steady-state activity measurements, the microreactor was heated resistively using a piece of silicon that was clamped below. The temperature was measured with a K-type thermocouple and controlled using a PID-controller (Eurotherm) from the top of the reactor. Figure 2.1(a) illustrates the aluminum interface block that the microreactor is mounted on. The two inlets for the feed gases and the gas outlet were designed to use $1/16$ " Swagelok fittings and stainless steel tubing, whereas the direct connection to the vacuum chamber for mass analysis utilized a copper sealed $1/4$ " VCR fitting. To maintain the vacuum in the vacuum chamber, the microreactor has a sniffer hole in the exhaust gas channel, *cf.* Section 2.2.1.2. The reactants were supplied and controlled using mass flow controllers (Bronkhorst), operating in the range from 0.02 to 1.00 ml min^{-1} with a precision of 0.02 ml min^{-1}. The total gas flow was kept constant for all measurements at 0.50 ml min^{-1}.

Beside the analysis of the reaction products using a Baltzers quadrupole mass spectrometer, an Agilent gas chromatograph was used to confirm the activity measured. In this case, gas samples were directly taken from the exhaust gas line. To avoid condensing water, formed by the catalytic reactions, the tubing between the microreactor and the analyzer was kept at a temperature of 100°C.

An initial attempt was made to seal the microreactors with a borosilicat glass lid. However, this turned out to be unsuitable for gold catalysts, because the low melting point of gold leads to sintering during the bonding process of the glass lid and makes the catalyst inactive. Therefore a Viton sheet was instead pressed on the microreactor. Figure 2.1(b) illustrates the changed setup, that was simply heated using a hotplate.

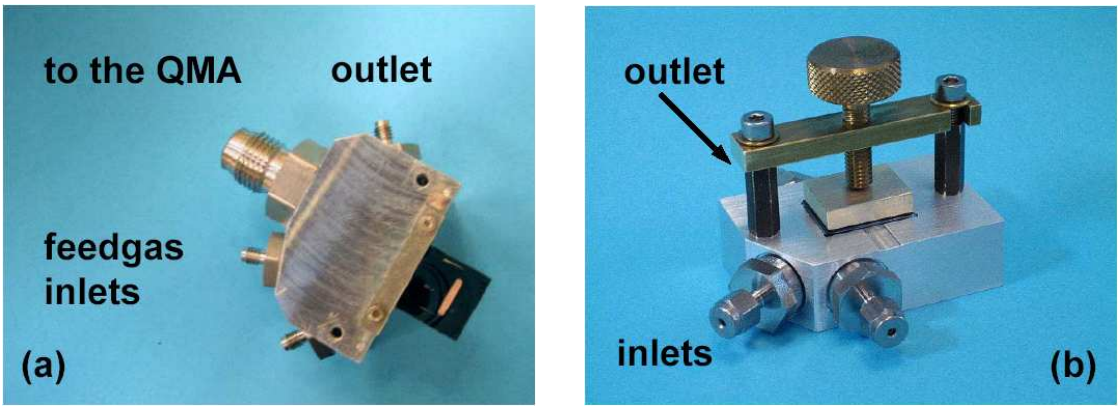

Figure 2.1: Aluminum interface block for microreactors that are directly mounted to a vacuum chamber (a) and for viton sealed microreactors (b).

Moreover, for CH_4 oxidation, gold is not as active as for CO oxidation. Thus, more catalyst is required to obtain signals that are resolvable close to the lower detection limit of the analysis methods used. Therefore steady-state activity measurements of metal-oxide supported gold catalysts were also performed in a mini-reactor. The mini-reactor is basically a quartz glass tube that was heated using a hotplate. Glass wool prevented the catalyst from being blown out.

2.2.1 Microreactors

Micro-structured devices are more commonly associated with fabrication techniques that were originally developed for electronic circuits. It is widely accepted that the smallest units of such miniaturized systems are sub-millimeter scaled. For reaction engineers, microreactors are small tubular reactors for catalyst screening and testing of the catalyst's performance. These are either continuous flow or batch-type reactors. Such continuous flow devices were already developed in the late 1980s [72, 73, 74].

When building a microreactor up in its structural hierarchy, the smallest unit is the catalyst that connects the fluid with the support in the reactor chamber. However, a unit cannot be operated alone. A microreactor also needs a *housing* that allows connection to externals periphery and micro-structured channels to and from the reactor chamber.

2.2.1.1 Why micro? — Is small better?

The main distinctions between microreactors and traditional chemical reactors are directly related to their size. Besides a larger ratio of surface area to volume, microreactors also allow one to drive highly exothermic reactions while avoiding hot-spot formation, since they have a high heat transfer rate [73, 74, 75]. With respect to a quick response to the heat supply, it has recently been reported that forced temperature oscillation enhances the rate for CO oxidation on a Pt/Al_2O_3 catalyst [76].

Moreover, the avoidance of mass-transfer limitation is the main objective in the development of microreactors [72, 75].

In contrast to the advantages of microreactors discussed, disadvantages and limitations of this technique shall also be addressed. The main challenge when microreactors are used in heterogeneous catalysis is to introduce the catalyst into the reactor. Quite a few systems reviewed recently are based on silicon and designed to introduce the catalyst before sealing using anodic bonding [75, 77]. However, such systems do not afford any access to the catalyst for post-analysis. Additionally, in some cases, the catalyst deactivates already due to the heat required to accomplish anodic bonding, e.g. gold nanoparticles.

To maintain conditions of molecular flow that allow us to assume that the continuum theory is valid, a critical length scale representing a physical length L —the width of the channels— needs to be defined. The Knudsen number $Kn = \lambda/L$ is a measure for whether statistical $(Kn \gg 1)$ or continuum mechanics $(0 < Kn \leq 10^{-3})$ is the better approach to formulate the fluid dynamics [78]. λ represents herein the mean free path for gases at standard temperature and pressure (6×10^{-8} m). Assuming $Kn < 10^{-3}$, the characteristic width of the channels would be > 60 µm.

2.2.1.2 The Microreactor Layout

The microreactors used within this PhD project were based on a silicon wafer and fabricated in the clean-room facilities of DANCHIP A/S [79] in collaboration with the Department of Micro and Nanotechnology [80], which are both located at the Technical University of Denmark. A more detailed description of the fabrication process, is provided in Appendix A.

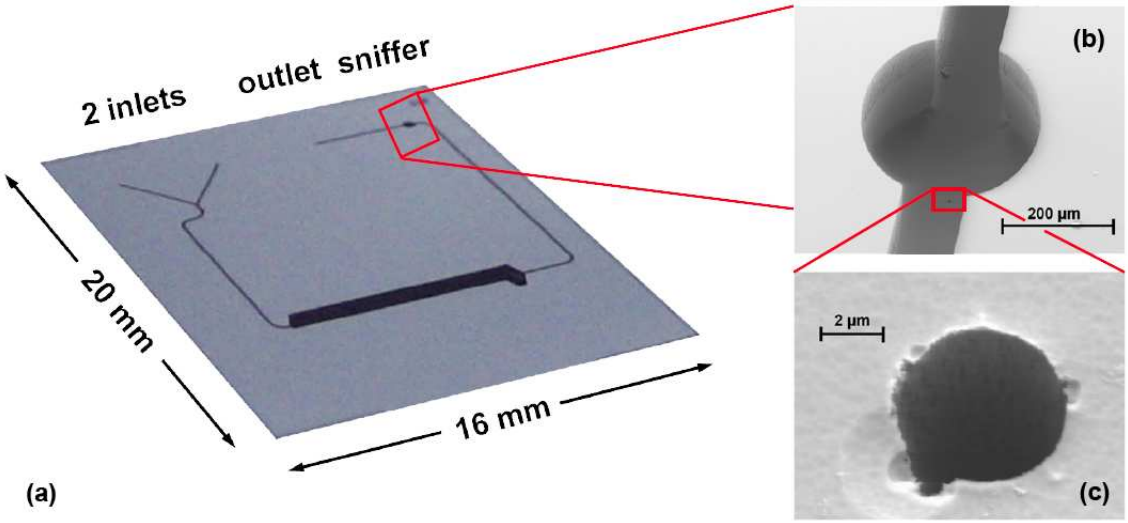

Figure 2.2: Unloaded silicon microreactor with two inlets to mix gases *on the chip*, a ($8.0 \times 1.5 \times 0.2$) mm^3 sized reactor chamber, a sniffer hole and a single outlet.

Figure 2.2(a) illustrates the 280 µm deep capillary system consisting of two inlets, a sniffer hole and one outlet. This allows mixing of undiluted gases *on the chip* without any danger of explosion. The dimensions of the reactor chamber are (8.0 × 1.5 × 0.2) mm^3. The whole device measures 20 mm × 16 mm × 0.35 mm and is sealed with a Pyrex glass lid using anodic bonding. The inlet and outlet holes as well as the sniffer hole are sealed with Viton O-rings to an aluminum interface block that connects the tubing to the microreactor. The microreactor is connected to a quadrupole mass spectrometer (QMA) via the sniffer hole in order to analyze the reaction products. Figures 2.2(b) and 2.2(c) show a zoom-in on the 3 µm sniffer hole, that allows direct mounting of the microreactor to a vacuum chamber.

Sufficient sealing of the microreactors may be obtained using anodic bonding. At about 300°C, sodium ions from the glass become displaced from the bonding surface, when a high DC potential (up to >1 kV) is applied. Since a depletion of sodium ions near the surface of the glass appears, the reactive glass surface forms a chemical bond with the silicon wafer.

In practice, a Viton sheet was pressed onto the microreactor instead of sealing it by a glass lid. This is because nanoparticulate gold has been found to sinter into larger particles at the temperatures required for anodic bonding [67, 69].

2.2.1.3 From the Setup to the Algorithm that derives the Oxidation Rate

The microreactors used fulfill the dimensional requirements for Knudsen conditions. It may thus be assumed that all gases are ideal. Hence the flux f of a gas flow $\dot{V}$ is given by

$$f = \dot{V} \frac{p}{k_B T}. \tag{1.1}$$

The oxidation rate r_{ox} is proportional to the flux of products formed during the reaction (e.g. CO_2 when considering (1.R2)), denoted as f_{CO_2}. Considering $f_{total} = f_{in} \simeq f_{out}$, the concentration of a product c_i that is either measured using a gas chromatograph or a mass spectrometer, is proportional to the flux of the product f_i. However, it has to be noted that f_{in} only equals f_{out}, when the amount of molar quantity of reactants equals the molar quantity of gas exiting the reactor. This is the case for CH_4 oxidation (*cf.* (1.R2)), but is not so for CO oxidation. Thus experiments shall carefully be conducted at low conversions and the mole ratio of entering and exiting gas shall be taken into account. Finally, the oxidation rate may be expressed as

$$\begin{aligned} r_{ox}(\vartheta) &= m_{cat}^{-1} f_{CO_2}(\vartheta), \\ &= m_{cat}^{-1} c_{CO_2}(\vartheta) \dot{V}_{total} \frac{p}{k_B T}. \end{aligned} \tag{1.2}$$

It should be noted that the absolute temperature T in (1.2) is constant, since it describes the ideal gas at the inlet. On the other hand, ϑ denotes the temperature at which the experiment was carried out.

2.2.1.4 Are Microreactors for Academic Studies Only?

Users of microreactors benefit primarily from the inherent safety during the reactor operation and the quick response to heat supply. Furthermore, microreactors afford with their small reactor volume the use of smaller amounts of catalyst. The ultimate extrapolation of this approach would be to study catalysis on an individual particle.

Beyond academic studies, microreactors have been used in recent years as a novel tool in commercial processes. Their use has been primarily in niche applications that could immediately benefit from the technology [75, 77]. To increase the throughput without suffering a pressure drop, microreactors are numbered-up to an assembly of microreactors, rather than scaled-up [72].

2.2.2 Mini-Reactors

A problem when using microreactors is that for some reactions the molar quantity of products is below the sensitivity of the detector. To increase the molar ratio of products to reactants, either the flow rate should be lowered or the amount of catalyst increased, while staying under thermodynamic conditions (*cf.* 1.2). Since the flow rate had already been minimized, increasing the amount of catalyst required a new setup. Instead of numbering up microreactors, mini-reactors were used.

Figure 2.3 shows a loaded mini-reactor. These reactors are made of quartz glass which is melted to Swagelok fittings. The fitting at the reactor inlet allows a connection to the gas supply in a manner that the reactants were first mixed in the reactor. The reactor volume is approximately 250 mm^3. This corresponds to 100 times the volume of the microreactors. However, it was not necessary to use the mini-reactors fully loaded.

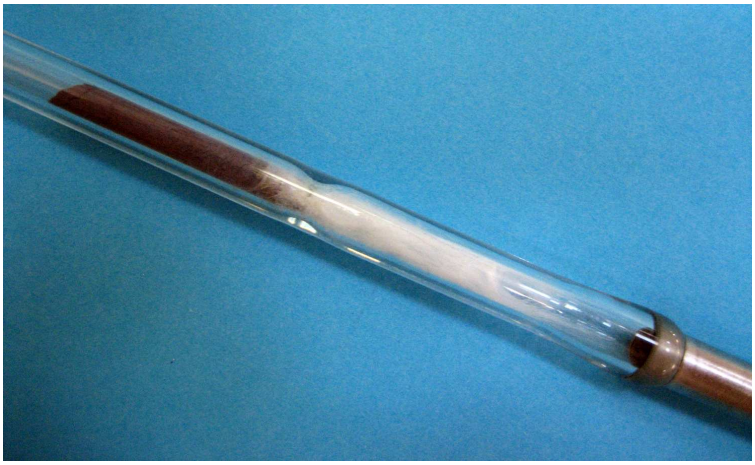

Figure 2.3: TiO_2 supported gold loaded quartz mini-reactor with an inner diameter of 3 mm. Glass wool prevents the catalyst from being blown out. The amount of catalyst shown here corresponds to ca. 62 fully loaded microreactors.

2.2.3 Gas Chromatograph — GC

Gas chromatography is an analytic method that allows separation of volatile substances of a complex gaseous sample and analysis of the concentration of each substance the sample contains. The analytical tool for the analysis of a gaseous sample is a module of a gas chromatograph.

2.2.3.1 Operation of a Gas Chromatograph

The basic parts of a module are a heated injector, a sample column, a reference column and a detector. A module also includes units for pressure and temperature control. Usually, a gas chromatograph contains two or more columns to detect heavier and lighter molecules at reasonable retention times. The principal operation of a gas chromatograph may be given in three major steps: injection, separation and detection.

A gaseous sample that the GC has sniffed enters a vessel where the temperature and pressure desired for injection are regulated before it is injected into the column. A vacuum pump helps to draw the gas through the system.

The gas injected is carried by a mobile phase (inert gas) at up to 6 bar through a narrow capillary lined with a thin polyimide layer, known as the stationary phase. Some columns are quasi-solid and filled with many parallel micropores, so called PLOT columns. This capillary represents the separation unit of a gas chromatograph and is kept isothermal to achieve a substantial separation of the substances.

At the outlet of the column, the substances pass a detection unit that identifies the substances by retention time. A more quantitative analysis may for example be achieved by a thermal conductivity detector (TCD). Here, the carrier gas and the substances pass different hot filaments. The power of the filament that is in the stream of the carrier gas, will remain constant, whereas the power of the filament in the sample stream requires regulation to keep the filament isothermal. This is in fact due to the different thermal conductivity of the substances. The difference in power required to keep the filaments isothermal is a measure of the output signal. The integral under the peak of the output signal is proportional to the concentration of the substance. The factor needs to first be determined by calibration with high purity (calibration) gases.

Other common detectors are flame ionization detector (FID) and quadrupole mass analyser (QMA). The combination of a GC with a QMA makes the detection of substances even more sensitive and an element-specific analysis is feasible.

2.2.3.2 The Agilent 3000 Micro-GC

Within this thesis, the instrument used to analyze the compounds of the exhaust gas was an Agilent Gas Chromatograph (3000 Micro-GC). This GC has combined columns of a molecular sieve 5A 10 m × 0.32 mm and a PLOT U 3 m × 0.32 mm pre-column with 1.0 µl back-flushing, which

allows simultaneous analysis of all the gases used and formed by a TCD. The settings of the carity-method are listed in Table B.1 in Appendix B.

It should be noted that with these settings and argon as the carrier gas, the GC is 15 times more sensitive to H_2 than to CO. Hypothetically, considering CO formation due to partial CH_4 oxidation, twice as much H_2 would be formed as CO, making its identification more convenient.

2.2.4 Mass Spectrometer — MS

Mass spectrometry is a very sensitive method for the analysis of residual gas compounds under high vacuum or even ultra high vacuum conditions. For the purpose of this PhD thesis, a Balzers quadrupole mass spectrometer (QMA 125) was used.

A QMA basically measures partial pressures of the residual gas. At the entrance of the QMA, electron bombardment from a hot filament ionizes a fraction of the residual gas molecules. They then pass through the oscillating electric field of a quadrupole where the ionized molecules become mass selected due to their mass-to-charge ratio, before they are detected by the secondary electron multiplier. The ion current obtained is a measure of how many ions hit the secondary electron multiplier and is consequently proportional to the partial pressures of the residual gas.

The actual output of ions after the ionization process contains not only ions that are single charged, but also multiple charged ions and even dissociated or cracked ionized derivatives of the original molecules. In the mass spectrum, these additional peaks appear as *fraction patterns*. Besides the ionization process, the fraction patterns are also dependent on the power of the filament and the geometry of the analyzer. During the analysis, the filament was operated with an ionization energy of 70 eV.

However, since this thesis deals with catalyzed reactions of monocarbon (C_1) chemistry, strongly overlapping peaks in the fraction pattern of the different C_1 derivatives made deconvolution of the spectra challenging. Thus, the QMA was only used to confirm the data that had been obtained using the gas chromatograph.

2.3 Additional Analysis Methods

2.3.1 Transmission Electron Microscopy — TEM

The analysis of physio-chemical information of industrial heterogeneous catalysts, such as the size distribution and the particle shape, is challenging [81]. When the catalytic active material has to be promoted by a support, usually the concentration of the catalyst is only a few weight percent. Bulk analysis methods such as X-ray diffraction (XRD) are probably too insensitive to

determine the average particle size. Even though scanning tunneling microscopy (STM) would provide information about the particle size, the position and the morphology can only be applied to a small subset of the sample geometries. An alternative technique is transmission electron microscopy (TEM). This was used to study the stability of the powder catalyst by comparing TEM images of specimens taken before and after the activity measurements.

2.3.1.1 Conventional TEM imaging

In conventional TEMs, a highly energetic electron beam that passes an electron lens system between the electron source (field emission electron gun) and the specimen to ensure an incident plane wavefront of the electron beam, is focused on the specimen. When the specimen is thinner than the mean free path of electrons λ_{mfp} the main part of the incident electron beam can penetrate the specimen without being affected. Figure 2.4(a) shows that these electron wave functions are

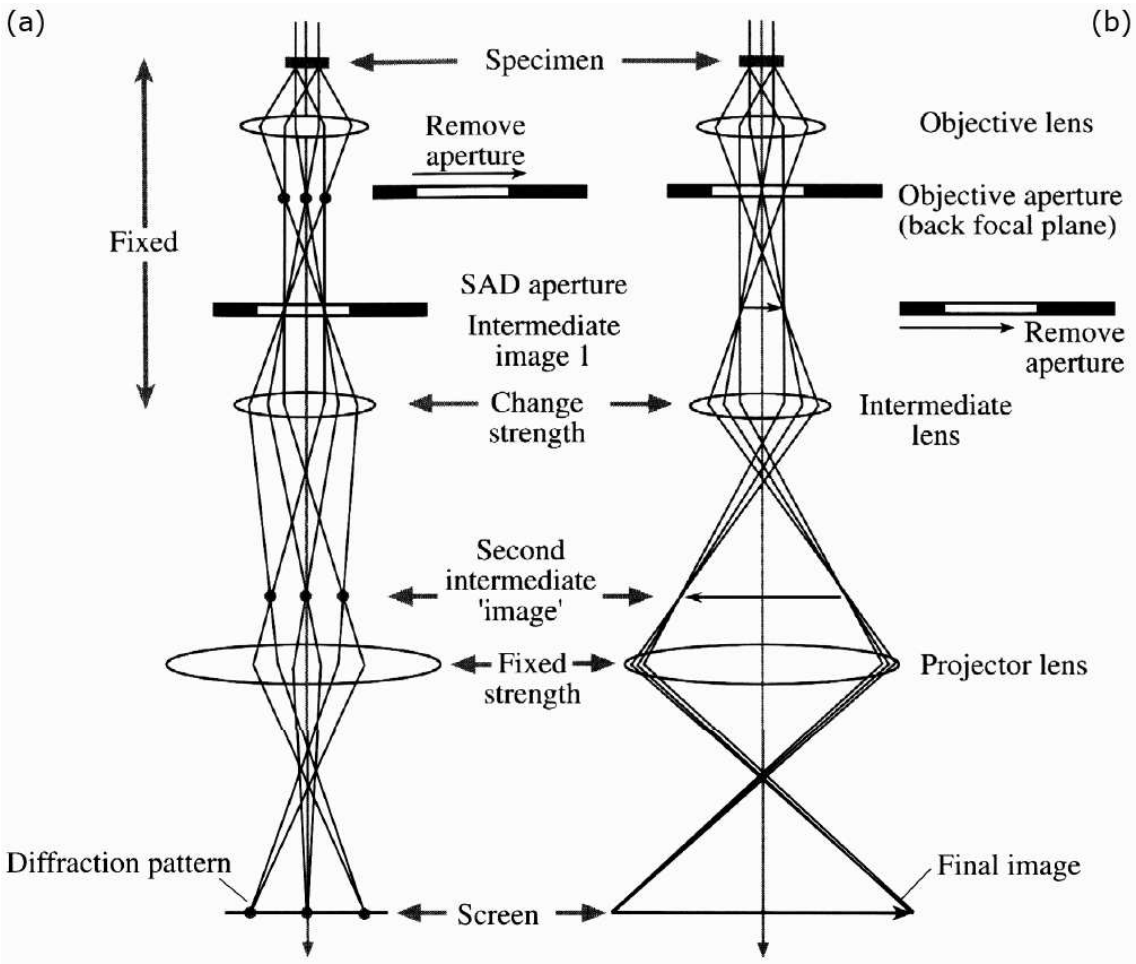

Figure 2.4: Scheme of the diffraction (a) and imaging (b) electron beam in a TEM. Adopted from [82].

spotted along the optical axis on the back focal plane, whereas electrons that have interacted with the specimen and also penetrated it are spotted beside the optical axis on the back focal plane. Moving the SAD aperture so that only the unaffected electrons contribute to form an image at the detector, the TEM is operated in the *bright field* (BF) mode. An image recorded of a diffracted electron beam is a *dark field* (DF) image [83].

2.3.1.2 High-Resolution TEM imaging

The principal of high-resolution TEM, HR-TEM, involves the superposition of BF and low-order DF imaging. Figure 2.4 shows the optical path to record the diffraction pattern as well as the final image. The contrast arises from the interference of the electron wave with itself in the back focal plane. Since the electron optics between the specimen and the detector have abberations (e.g. astigmatism, defocus of the objective lens, etc.), the transmitted electron wave undergoes further phase changes. The relationship between the electron wave $\psi(\mathbf{k})$ and the image wave is highly non-linear and is in a crude approximation described by the contrast transfer function, that is determined by the abberation of the microscope (mainly the objective aperture $\mathcal{A}(\mathbf{k})$, the effect of coherence $\mathcal{E}(\mathbf{k})$ and the phase distortion $\chi(\mathbf{k})$), so that

$$\mathcal{T}(\mathbf{k}) = 2\,\mathcal{A}(\mathbf{k})\,\mathcal{E}(\mathbf{k})\,\sin\chi(\mathbf{k}), \tag{1.3}$$

where $\mathbf{k}$ refers to the spatial frequencies [84].

The phase distortion function $\chi(\mathbf{k})$ strongly depends on the spherical abberation coefficient C_S, a quality parameter of the objective lenses that, as can be seen in Equation 1.4, is responsible for a phase shift.

$$\chi(\mathbf{k}) = \pi\Delta f\lambda\mathbf{k}^2 + \tfrac{1}{2}\pi C_S\lambda^3\mathbf{k}^4 \tag{1.4}$$

Herein, Δf denotes the defocus of the objective lens. Under conditions of underfocus, the imaging system is optimized with respect to $\mathcal{T}(\mathbf{k})$. The first passband is widest. Scherzer proposed the value of defocus to be

$$\Delta f_{\text{Scherzer}} = -1.2\sqrt{C_S\lambda}. \tag{1.5}$$

The effect of $\chi(\mathbf{k})$ on the contrast transfer function is shown in Figure 2.5(a). The objective aperture is chosen to eliminate all the radiation scattered at higher angles, for which the contrast transfer function $\mathcal{T}(\mathbf{k})$ is oscillatory [86]. However, the envelope function $\mathcal{E}(\mathbf{k})$ dampens the signal of the electron wave scattered at higher angles and determines the information limit of the microscope. As contributions to the envelope function, there are two major factors which impose the limit on the resolution of the microscope [84]. First, the temporal coherency envelope function, which is dependent on the chromatic aberration and takes the form

$$\mathcal{E}_c(\delta,\,\mathbf{k}) = \exp\left(-\tfrac{1}{2}(\pi\lambda\delta^2)\mathbf{k}^4\right) \tag{1.6}$$

with standard deviation δ. Second, the spatial coherency, which is defined by the convergence of the electron beam α. It is given by the envelope function

$$\mathcal{E}_s(\alpha,\,\mathbf{k}) = \exp\left(-(\pi\alpha)^2(\Delta f\mathbf{k} + C_S\lambda^2\mathbf{k}^3)^2\right). \tag{1.7}$$

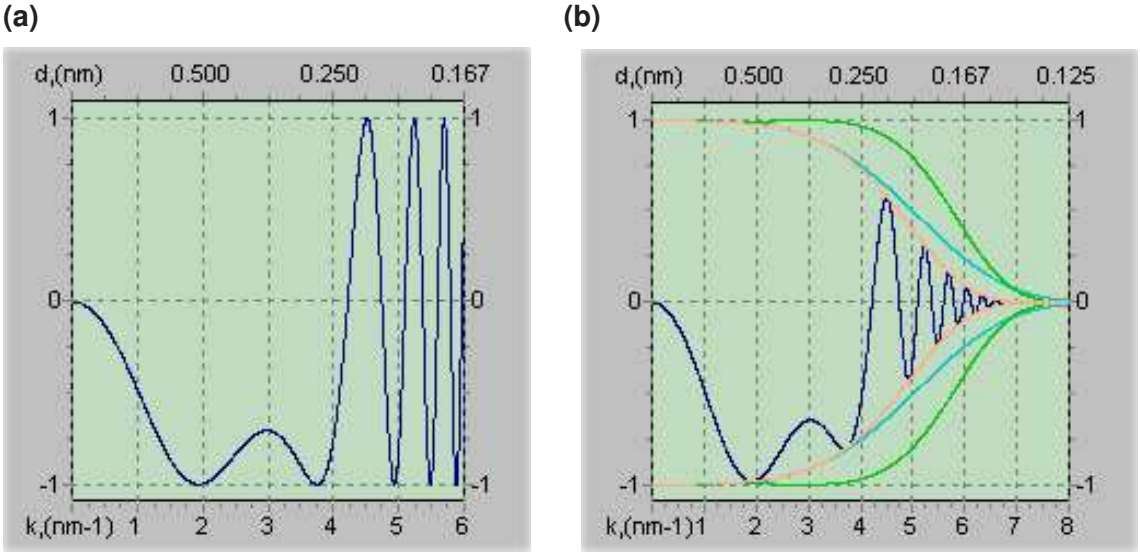

Figure 2.5: CTF at Scherzer defocus 1.2 for a Tecnai 20T microscope operated at 200 kV and for C_S = 0.5 mm in ideal case (a) and with included envelopes that show the limitation to the resolution by the spatial coherency (green line), the temporal coherency (blue line) and the superposition of both (orange line) (b), adopted from [85].

In Figure 2.5(a) the contrast transfer function is plotted as a function of the spatial frequencies $\mathbf{k}$ in an ideal case. At the point where $\mathcal{T}(\mathbf{k})$ crosses the abscissa, point resolution occurs and indicates the information limit of an interval of the spatial frequency. Figure 2.5(b) shows how abberations influence $\mathcal{T}(\mathbf{k})$.

Finally, the intensity of a recorded image may be described by the norm of the Fourier transformation of the wave function that has been influenced when passing through the objective lens system of the microscope,

$$I(\mathbf{k}) = \left|\mathcal{F}^{-1}[\mathcal{T}(\mathbf{k}) \circ \psi(\mathbf{k})]\right|^2 . \tag{1.8}$$

2.3.2 X-Ray Fluorescence — XRF

X-ray fluorescence is a non-destructive element-specific analysis technique. It is highly accurate in the determination of major elements (~ 0.1 %) and is thus suitable for proving whether a catalyst is contaminated, e.g. by surfactant used during the preparation process.

2.3.2.1 The X-Ray Fluorescence Process

The principle of XRF is based on the emission of characteristic X-rays from the sample material, that has previously been excited by high energy photons (X-rays with $h\nu \geq 1$ kV). Figure 2.6(a) sketches the ejection of a K electron from the atom by the external excitation X-ray. The vacancy formed in the K shell is due to the unstable electron configuration being filled by an electron from

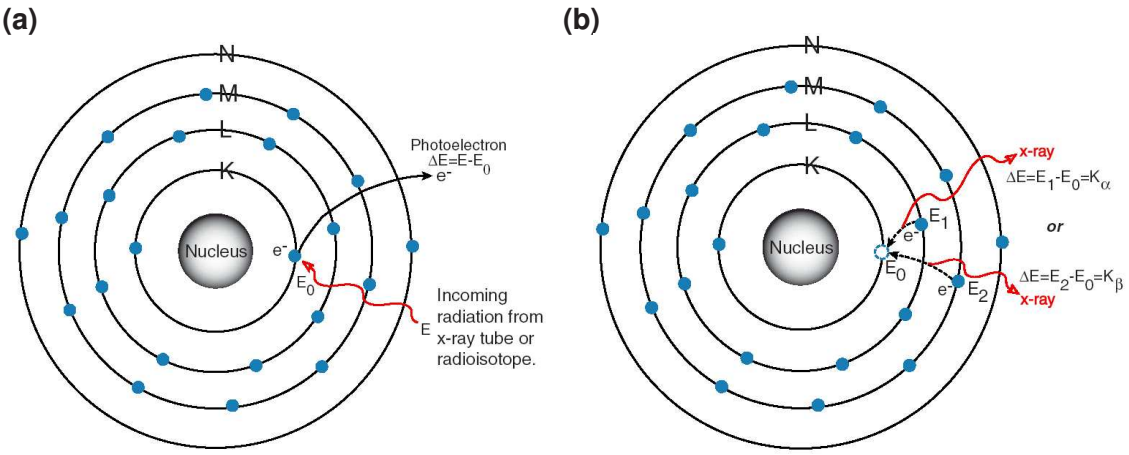

Figure 2.6: Example of the XRF process on a titanium atom. Absorption of high-energetic radiation leads to ejection of an electron in the K shell (a) and results in re-emission of lower energy radiation, when the vacancy formed in the K shell is being filled by an electron from a higher orbital (b) [87].

a higher orbital (L or M shell). The associated energy loss leads to the emission of a secondary X-ray (*cf.* Figure 2.6(b)) which is characteristic of the element. The intensity of secondary photons emitted is proportional to the concentration of the element.

2.3.2.2 The MiniPal 4 X-Ray Spectrometer

For elemental analysis of the catalysts, a MiniPal 4 X-ray spectrometer (PANalytical B.V.) was used. This compact energy dispersive X-ray spectrometer operates at 30 kV using a rhodium anode. A sample may be in solid, liquid or in gas phase. With a 2048 channel analyzer board, incident X-ray photons are detected with a resolution that allows elemental analysis from sodium to uranium. For an improved sensitivity for elements of low atomic numbers ($_{11}$Na – $_{19}$K), measurements require a helium atmosphere [88].

CHAPTER 3

CO and H_2 Oxidation on Gold

The oxidation of CH_4 favors a reaction pathway that proceeds to form CO_2 by full combustion. This reaction has been studied extensively with the purpose of the removal of hydrocarbon pollutants from the global environment [8]. From the thermodynamic point of view, monocarbon oxygenates and CO are much more reactive than CH_4. Perhaps during the course of CH_4 oxidation, such species are formed and immediately post-oxidized to CO_2. Then, such post-oxidative reactions are competing side reactions of possible reaction products.

This chapter deals with such side reactions and focuses on the two most likely ones, the oxidation of CO to CO_2 and the oxidation of H_2 to H_2O. These reactions were studied on three different sizes of gold catalysts using either O_2 or N_2O as the oxidation agent. Steady-state activity measurements were performed in microreactors. To corroborate the experimental findings, the reaction rate for CO oxidation was modeled also using DFT calculations on the stepped Au$\{532\}$ surface and on a Au_{12} cluster in a microkinetic model. The findings suggest that such a model quantitatively describes the kinetics of CO oxidation using small Au nanoparticles (d < 5 nm).

Besides the reaction kinetics that the chapter focuses on, the catalysts are also analyzed in terms of their stability for these reactions.

3.1 Study of the Effect of Particle Size

As it has been outlined in the introduction, the activity of gold is strongly size dependent for CO oxidation. The common oxidation agent for CO oxidation, used in all the studies mentioned so far was oxygen. Very few studies deal with other oxidation agents, such as nitrous oxide, and they focus on the decomposition and reduction of N_2O [89]. Since N_2O is known to readily dissociate into adsorbed atomic O and gas phase N_2 in the presence of CO, the oxidation of CO by N_2O involves atomic O. On the other hand, CO oxidation using O_2 has been shown to also occur via an alternative pathway, which does not include O_2 dissociation [49, 90]. By using these two different oxidation agents, the activity of nanoparticulate gold shall experimentally be compared for two different CO oxidation pathways.

With respect to associatively formed H_2O during CH_4 oxidation, H_2 oxygenation shall also be analyzed. Thus, in this experimental study four reaction shall be considered:

$$CO + N_2O \longrightarrow CO_2 + N_2 \qquad \Delta H^0 \approx \text{-200.9 kJ mol}^{-1} \qquad \text{(3.R1)}$$

$$CO + {}^1\!/_2\, O_2 \longrightarrow CO_2 \qquad \Delta H^0 \approx \text{-283.0 kJ mol}^{-1} \qquad \text{(3.R2)}$$

$$H_2 + N_2O \longrightarrow H_2O + N_2 \qquad \Delta H^0 \approx \text{-159.8 kJ mol}^{-1} \qquad \text{(3.R3)}$$

$$H_2 + {}^1\!/_2\, O_2 \longrightarrow H_2O \qquad \Delta H^0 \approx \text{-241.8 kJ mol}^{-1} \qquad \text{(3.R4)}$$

These reactions were studied on three different catalysts in a low-temperature regime (ϑ = 30 – 160°C):

(A) $Au_{2.0\,nm}/TiO_2$ (1.02 wt% Au), supplied by Project AuTEK [70],
(B) $Au_{3.3\,nm}/TiO_2$ (1.56 wt% Au), supplied by the World Gold Council [71],
(C) $Au_{5.0\,nm}/TiO_2$ (1.60 wt% Au), home-made as described in Section 2.1.

Temperature-programmed activity measurements of these catalysts were performed in microreactors, which were connected to a GC. The gases applied had a purity of 4.8N (CO), 5.0N (H_2), 3.5N (O_2) and 2.5N (N_2O). Due to the high sensitivity of the GC to H_2, the reactants in (3.R3) and (3.R4) were diluted with 50% argon with the total flow kept constant at 1.00 ml min^{-1} for all reactions.

To minimize the contribution of self-heating of the catalyst during an exothermic reaction, all experiments were performed with a maximum of 10% conversion, except for CO oxidation where 15% was achieved at 60°C on Catalyst A and more than 40% at 80°C on Catalyst B. The greatest amount of heat liberated during the reactions was 26.0 mW.

For all measurements the following scheme was followed to ensure reproducibility. First, all catalysts were activated. Catalysts B and C, containing the larger particles, were pretreated over 20 hours at 80°C to ensure steady-state activity measurements. On the other hand, due to its high activity and the possibility of sintering, Catalyst A was pretreated for 20 hours at 50°C. These

pretreatments were done under stoichiometrically supplied CO and O_2, for the reaction CO + $^1/_2$ $O_2 \longrightarrow CO_2$, and a total gas flow of 1.00 ml min^{-1}. The CO conversion decreased by 33%, 17%, and 5% before stabilizing for the powder Catalysts A, B, and C, respectively. Temperature programmed activity measurements were then performed in the following sequence of reactions for each catalyst: (3.R2), (3.R1), (3.R3), (3.R4), (3.R2), (3.R1).

Since the maximum temperature reached under these reactions (120°C on Catalyst B and 160°C on Catalyst C) was higher than the temperature of the pretreatment (80°C), the last two steps (remeasurement of (3.R2) and (3.R1)) were performed to ensure that the catalysts had not changed during the preceding reactions. Furthermore, to exclude any influence of the applied gases (by e.g. catalyst reduction), the reaction sequence was also conducted in reversed order —starting with (3.R2)— on a fresh and deactivated catalyst from the same batch. Hereby, the rate differed for each of the reactions (3.R1) – (3.R4) studied, but the proportions between (3.R2) and (3.R1), and between (3.R4) and (3.R3) were similar.

Transmission electron microscopy (TEM) was used to study changes in size of the gold particles. For each catalyst, specimens were taken as the catalysts were supplied, after the pretreatment and after measurements of all four catalytic reactions. The specimens were then prepared on a carbon TEM grid by dropping a suspension of catalyst in ethanol on the grid. These were analyzed using a JEOL 3000F field emission electron microscope, which was operated at 300 kV with a LaB_6 filament as an electron source.

3.1.1 Preliminary Investigations

It shall first be focused on the thermodynamically unstable N_2O, when it is applied to the catalyst and to the bare support material only. At temperatures below 160°C no dissociation of N_2O could be measured on either Catalyst B, Catalyst C or bare TiO_2 (Degussa P25). However, in the presence of a reducing agent, e.g. H_2 or CO, N_2O could be reduced over the catalysts, but not over the bare support material. This has also been reported by Nieuwenhuys *et al.* [89].

Additionally, CO and O_2 were applied to bare TiO_2 in a stoichiometric ratio of 2:1 to check whether (3.R2) proceeds on the bare support. This was not the case.

3.1.2 Steady-state Activity Measurements

Figure 3.1(a) shows Arrhenius plots for (3.R1) – (3.R4) on Catalyst A. Surprisingly, the activation energies obtained were all approximately 37 kJ mol^{-1}, as may be seen from the parallel linear fits. Table 3.3 summarizes these and the following activation energies. However, for CO oxidation the reaction rate differs by a factor of 2.7, when comparing the different oxidation agents with each other. For hydrogen oxidation, the catalyst behaves similarly. The linear fits run parallel and the reaction rate differs by 3.2. On the Au particles of Catalyst B, which were sintered to 5.7 nm, the trend depicted on Catalyst A continues, but is even more distinct, as shown in Figure 3.1(b). There is approximately one order of magnitude between the rates of CO oxidation and for H_2 oxidation,

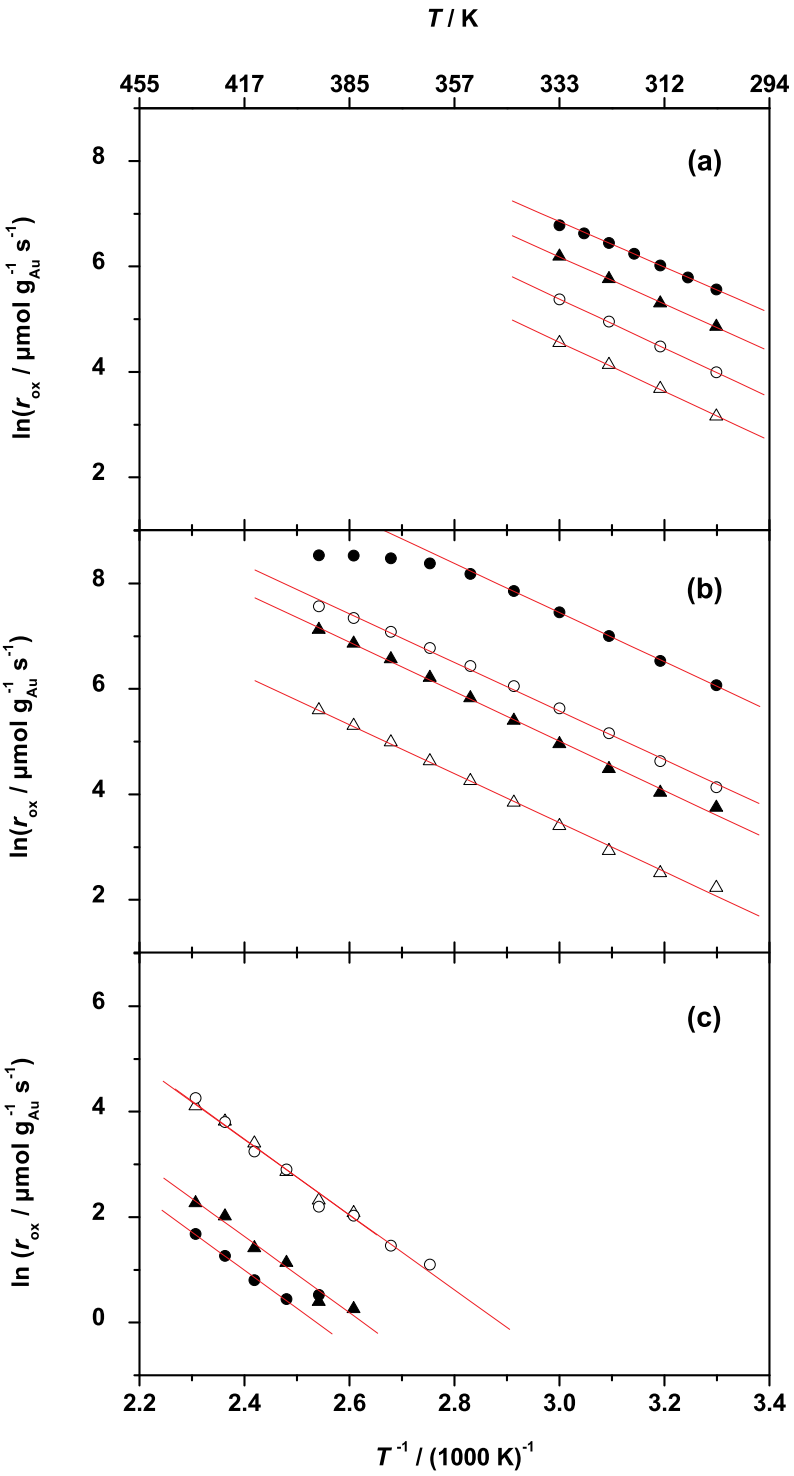

Figure 3.1: Arrhenius plots of the activation energies for the four reactions on TiO_2 supported gold particles of Catalyst A (a), Catalyst B (b) and Catalyst C (c): CO + ½ O_2 (•), CO + N_2O (▲), H_2 + ½ O_2 (○) and H_2 + N_2O (△). An overview of the activation energies is given in Table 3.3.

using N_2O and O_2, respectively.

When using O_2 as oxidation agent, the oxidation rates for CO and H_2 oxidation on Catalyst B were found to go into saturation at 80°C and 120°C, respectively, *cf.* Figure 3.1(b). One reason for this may be that the catalyst was operated under mass-transport controlled conditions, e.g. when too little active material has been used. On the other hand, this may also be due to CO and O_2 desorption. Despite this, the parallel running fits of the Arrhenius plots indicate again similar activation energies around 39 kJ mol^{-1}, as shown in Table 3.3. These two catalysts where active even at room temperature, although O_2 was a significantly better oxidation agent. For (3.R1), N_2 released from N_2O could be balanced with the CO_2 formed, indicating that the CO_2 does not originate from other sources.

Figure 3.1(c) shows Arrhenius plots for Catalyst C and demonstrates that on this catalyst N_2O is the better oxidation agent for CO, whereas no difference in rate could be found for H_2 oxidation. The activation energy was again very similar for all the four studied reactions. On these large particles an onset of conversion could not be observed below 80°C.

3.1.3 TEM Investigation on Changes in Particle Size

Prior to discussing individual reactions, TEM images of the catalysts (*cf.* Figure 3.2) shall first be analyzed to evaluate the influence of pretreatment and catalytic reactions on the gold particles. Numerical values for the change in particle size of each catalyst are summarized in Table 3.1.

The TEM images in Figure 3.2(a) show typical images of Catalyst A from its state as supplied (i), its state after the pretreatment (ii) and its state after catalytic reactions (iii). The particles may potentially sinter during storage. However, this was not the case, since the average of the particle size in (a) (2.3 ±0.6 nm), based on TEM images of 97 particles, is consistent with that stated by the supplier (2.0 nm). The particles appear predominately in a truncated cuboctahedron shape. Following the pretreatment, the average particle size was determined to be 2.6 ±0.6 nm. The particles themselves were still well dispersed on the support, as can be seen in Image 3.2(a)(ii). Following the catalytic reactions, the gold particles were sintered to 3.6 ±0.8 nm.

The size of the gold particles from Catalyst B stated by the supplier (3.3 nm), was also confirmed, as may be seen in Image 3.2(b)(i). Image 3.2(b)(ii) shows the particles observed after pretreatment, which were only slightly larger. However, after reactions the gold particles' size increased significantly, *cf.* Image 3.2(b)(iii).

Figure 3.2(c) shows Catalyst C, which was formed in-house. Already during preparation, the gold particles sintered from 5.0 nm, as supplied in solution, to 13.3 ±6.5 nm and formed truncated cuboctahedrons. The pretreatment led to further sintering, with the average particle size becoming 16.2 ±6.6 nm. This catalyst did not show any further changes in size after catalytic reactions.

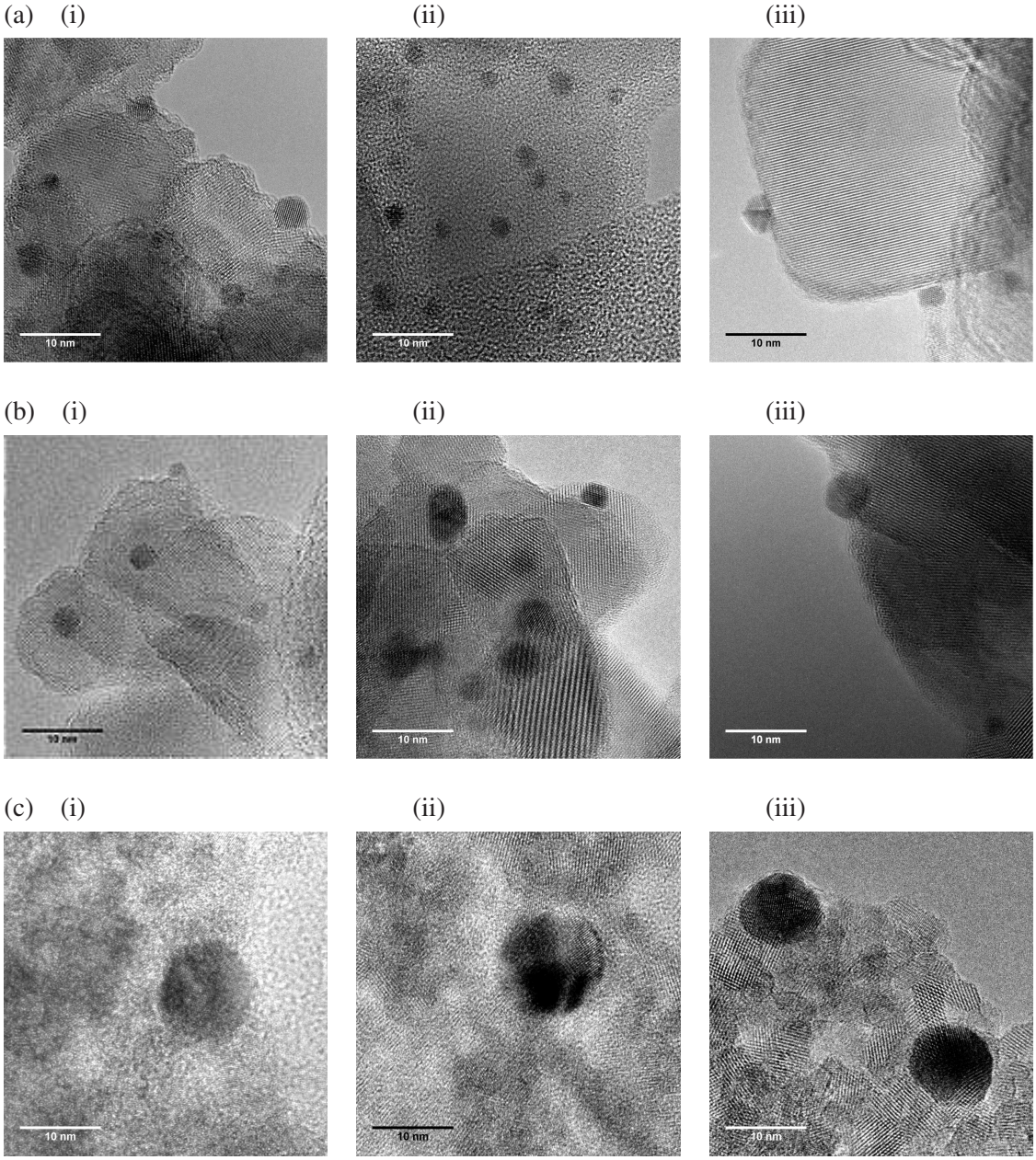

Figure 3.2: Bright field TEM images of TiO_2 supported gold particles of Catalyst A (a), Catalyst B (b) and Catalyst C (c), as they were supplied/prepared (i), after the pretreatment (ii) and after catalytic reactions (iii). A summary of the change in particle size may be found in Table 3.1. The scale bars correspond to 10 nm in each image.

Table 3.1: Average particle size *d* in nm, as determined by TEM, before and after performing oxidation reactions.

d_{Au} / nm	total gold loading	as supplied† or prepared‡	before reaction	after reaction
Catalyst A	62.22 µg	2.3±0.6 †	2.6±0.6	3.6±0.8
Catalyst B	63.96 µg	3.4±0.8 †	3.8±1.1	5.7±3.4
Catalyst C	54.00 µg	13.3±6.5 ‡	16.2±6.6	16.2±6.6

3.2 Oxidation of CO on Au/TiO_2 — A DFT Study

When experimental findings seems to be difficult to interpreted, it is good to have theoretical calculations that the interpretations from the experiments can be compared with. The calculations were mainly performed by Dr. Duncan J. Mowbray and Tao Jiang at the Center for Atomic-scale Materials Design at the Technical University of Denmark.

Since CO oxidation on gold is strongly suggested to occur at low coordinated sites [29, 51, 52], the corner atoms of a truncated cuboctahedron gold particle (*cf.* Section 3.1.3) were modeled by both a Au_{12} cluster and the Au$\{532\}$ surface, which is basically made of kinks and B5 sites only. A model for CO oxidation by O_2 needs to be specified whether the oxidation occurs directly via a CO–O_2 intermediate or an atomic O. The latter one may be assumed to be a good approach for the oxidation reaction when using N_2O instead of O_2.

3.2.1 Theoretical Methodology

All theoretical results have been obtained using the DFT code DACAPO [91]. The Kohn-Sham one-electron valence states were expanded in a plane wave basis set with a 340 eV (25 Ry) kinetic energy cutoff, and a density cutoff of 680 eV (50 Ry). The core electrons were described by Vanderbilt type ultrasoft pseudopotentials [92]. The exchange-correlation potential was described using the RPBE generalized gradient approximation self-consistently [93]. For the Au$\{532\}$ surface, a 4×4×1 Monkhorst-Pack **k**-point sampling was applied in the irreducible Brillouin zone. The surface was modeled by a 1×1-$\{532\}$ unit cell containing 24 Au atoms with periodic boundary conditions, which corresponds to a three-layer slab. The top most layer and the adsorbents were allowed to fully relax. The oxygen adsorption energy was calculated relative to the experimentally obtained formation energy of H_2O from O_2 and H_2 [94]. This avoids difficulties associated with a DFT treatment of the O_2 triplet state in the gas phase [95].

Thermodynamic analysis was carried out using the total energies obtained from the DFT calculations. In this contribution, free energies have been calculated by employing standard formulas

Table 3.2: Activation barriers E_a and adsorption energies E_{ads} in eV for CO and H_2 oxidation by N_2O and O_2 [98].

E / eV	Au{532} surface	Au_{12} cluster
$E_{ads}[O_2]$	-0.28	-0.63[a]
$E_{ads}[CO]$	-0.77	-0.95[a]
$E_{ads}[N_2O]$	-0.08[b]	-0.08[b]
$E_a[CO + O_2 \longrightarrow CO_2 + O]$	—	0.28[a]
$E_a[CO + O \longrightarrow CO_2]$	0.28	—

[a]Ref. [53], [b]Ref. [97]

for the thermodynamics of a classical ideal gas [96]. For a gas-phase species X at temperature T and pressure p, the Gibbs free energy $G_X(p,T)$ is given by

$$G_X(p,T) \quad = \quad E_X + E_{ZPE} + \Delta H(T) - TS(T) + RT\ln(p/p_0),$$

where E_{ZPE} is the zero point energy, $\Delta H(T)$ denotes the enthalpy change due to raising the temperature from 0 K to T, $S(T)$ is the entropy at T, R is the universal gas constant, and p_0 denotes the standard pressure (taken to be 1 bar).

The potential energy of an adsorbed species X*, E_X, is given by $E_{*/X*} - E_*$, where E_* is the energy of the clean surface and $E_{*/X*}$ is the energy of the adsorbate and the surface system. In order to calculate the free energy of this species, we neglect the pressure term, so that the enthalpy change is replaced by the change in internal energy. This leads to the following expression for the free energy $G_X(p,T)$:

$$G_X(p,T) \quad = \quad E_{X*} + E_{ZPE} + \Delta U(T) - TS(T).$$

The forward rate constant for a reaction i may then be expressed in terms of the Gibb's free energies as $k_i = \upsilon_i \exp[-\Delta G/k_B T]$, where $\Delta G = \sum_{X\epsilon\mathcal{P}} G_X - \sum_{X\epsilon\mathcal{R}} G_X$ is the difference of the total Gibb's free energy of the products $\mathcal{P}$ and reactants $\mathcal{R}$ for reaction i, k_B is Boltzmann's constant, and $\upsilon_i \equiv k_B T/h$ is the pre-exponential factor.

The DFT energies for the adsorbed species E_{X*} as well as the activation barriers are given in Table 3.2. For the N_2O adsorption energy, we have used the experimental value given in Ref. [97].

3.2.2 Microkinetic Model

Any heterogeneous catalysis reaction may be expressed in the form

$$R(g) \quad \overset{*}{\longrightarrow} \quad P(g),$$

where R(g) denotes the gas phase reactants, " * " the active sites on the catalyst, and P(g) the products in the gas phase. If the reaction kinetics are assumed to follow a Langmuir–Hinshelwood mechanism, the elementary steps may be written in the form

$$\begin{aligned} \mathrm{X(g)} + * \quad &\rightleftharpoons \quad \mathrm{X}*, \quad \forall\ \mathrm{X} \in \mathcal{R}, \\ \mathrm{R}* \quad &\xrightarrow{\text{rds}} \quad \mathrm{P(g)}. \end{aligned}$$

The reaction rate for the rate determining step (rds) is then

$$r_{\text{rds}} \approx k^{+}_{\text{rds}} \prod_{\mathrm{X}\in\mathcal{R}} \theta_{\mathrm{X}*}, \tag{3.1}$$

where $\theta_{\mathrm{X}*}$ is the coverage of species X on site " * ", and k^{+}_{rds} is the rate constant for the forward rate, which may by assumed dominates the total reaction rate.

Assuming the difference in zero point energies of the products and the reactants ΔE_{ZPE} is much smaller than the activation barrier $E_{\text{a}}[\text{rds}]$, and the entropy of the adsorbed species is much smaller than that of the species in gas phase, $S_{\mathrm{X}*} \ll S_{\mathrm{X(g)}}$, the forward rate constant may be expressed for the rds as

$$k^{+}_{\text{rds}} \approx \frac{k_{\text{B}}T}{h} \exp\left[-\frac{E_a[\text{rds}] - T\sum_{\mathrm{X}\in\mathcal{P}} S_{\mathrm{X(g)}}}{k_{\text{B}}T}\right]. \tag{3.2}$$

Since the adsorption steps are assumed to occur in equilibrium,

$$r_{\mathrm{X}*} = k^{+}_{\mathrm{X}*} p_{\mathrm{X}} \theta_{*} - k^{-}_{\mathrm{X}*} \theta_{\mathrm{X}*} = 0,$$

so that

$$\theta_{\mathrm{X}*} = \frac{k^{+}_{\mathrm{X}*}}{k^{-}_{\mathrm{X}*}} p_{\mathrm{X}} \theta_{*} = K_{\mathrm{X}*} p_{\mathrm{X}} \theta_{*},$$

where p_X is the gas phase pressure of species X, while $K_{\mathrm{X}*}$ is the ratio of the forward to backward rate constants. This may be expressed explicitly in terms of the adsorption energy $E_{ads}[\mathrm{X}]$ and gas phase entropy $S_{\mathrm{X(g)}}$ of species X as

$$K_{\mathrm{X}*} \approx \exp\left[-\frac{E_{\text{ads}}[\mathrm{X}] + TS_{\mathrm{X(g)}}}{k_{\text{B}}T}\right], \tag{3.3}$$

where again $S_{\mathrm{X}*} \ll S_{\mathrm{X}}$ and ΔE_{ZPE} is assumed to be much smaller than the adsorption energy of species X.

3.2.3 Kinetic Picture of CO Oxidation on Nanoparticular Gold

Recent DFT and experimental studies of CO oxidation reactions on a large range of Au nanoparticles have suggested that the active sites are at the particle corners [29, 44, 52]. This is illustrated by the strong correlation between CO activity and the number of corner sites per atom, which is

approximated by assuming the particle shape resembles the top half of a regular cuboctahedron.

The particles considered in the present study are cuboctahedral in shape, as shown in Figure 3.2, and have CO oxidation activities in excellent agreement with the d^{-3} analysis presented by Nørskov *et al.* [51]. As such, the theoretical analysis shall begin by assuming the CO oxidation reactions occur on the corner sites of the Au particles.

First, it shall be considered CO oxidation using N_2O. It has been generally accepted that the reaction kinetics for CO oxidation over a metal surface follow the Langmuir–Hinshelwood mechanism. According to this, the elementary steps of adsorption and desorption are in equilibrium, and (3.R1) may be written in terms of the following elementary steps:

$$\mathrm{CO(g)} + * \quad \rightleftharpoons \quad \mathrm{CO}* \tag{3.R1a}$$

$$\mathrm{N_2O(g)} + ☼ \quad \rightleftharpoons \quad \mathrm{N_2O}☼ \tag{3.R1b}$$

$$\mathrm{CO}* + \mathrm{N_2O}☼ \quad \xrightarrow{\text{rds}} \quad \mathrm{CO_2(g)} + \mathrm{N_2(g)} + * + ☼ \tag{3.R1c}$$

Here we have assumed that CO and N_2O adsorb on different types of corner sites, denoted by " * " and " ☼ " respectively. This is clearly the case for CO oxidation, as may be seen from the transition states depicted in the insets of Figure 3.3.

Since N_2O was found not to dissociate spontaneously on gold, as has also been reported by Gluhoi *et al.* [89], it may be assumed that this reaction requires adsorbed CO* as a reducing agent. However, the overall barrier for (3.R1c) should still be the same as for CO oxidation with atomic O. On the other hand, the desorption of both N_2 and CO_2 should occur spontaneously.

To model the corner sites of a gold nanoparticle for reaction (3.R1c), a Au$\{532\}$ surface has been chosen, which consists of both B5 and kink sites. This allows atomic O to adsorb on the preferred B5 sites while CO adsorbs on the kink sites. This is depicted in the Au$\{532\}$ transition state for (3.R1c), shown in the lower inset of Figure 3.3. Since the Au_{12} cluster model of a corner site [53] does not include B5 sites for atomic O adsorption, it yields an activation barrier for (3.R1c) twice that found for the Au$\{532\}$ surface. For this reason, the Au_{12} model should not be used to model (3.R1c).

Employing the microkinetic model described above, the reaction rate for the rate determining step (rds) r_{rds}, may then be approximated by

$$r_{\mathrm{rds}} \approx \frac{k_{\mathrm{B}}T}{h}\frac{K_{\mathrm{CO}*}K_{\mathrm{N_2O}☼}p_{\mathrm{CO}}p_{\mathrm{N_2O}}}{(1+K_{\mathrm{CO}*}p_{\mathrm{CO}})(1+K_{\mathrm{N_2O}☼}p_{\mathrm{N_2O}})} \exp\left[-\frac{E_{\mathrm{a}}[\mathrm{rds}] - T(S_{\mathrm{CO(g)}} + S_{\mathrm{N_2O(g)}})}{k_{\mathrm{B}}T}\right], \tag{3.4}$$

where $K_{\mathrm{CO}*}$ and $K_{\mathrm{N_2O}☼}$ are given in (3.3). The required activation and adsorption energies for the Au$\{532\}$ surface are provided in Table 3.2 and the gas phase entropies are taken from Ref. [10].

Figure 3.3 shows the temperature dependence of the reaction rate r_{rds}, for the rds of CO oxidation by N_2O on Au$\{532\}$. r_{rds} was found to follow an Arrhenius-like behavior in the low temperature

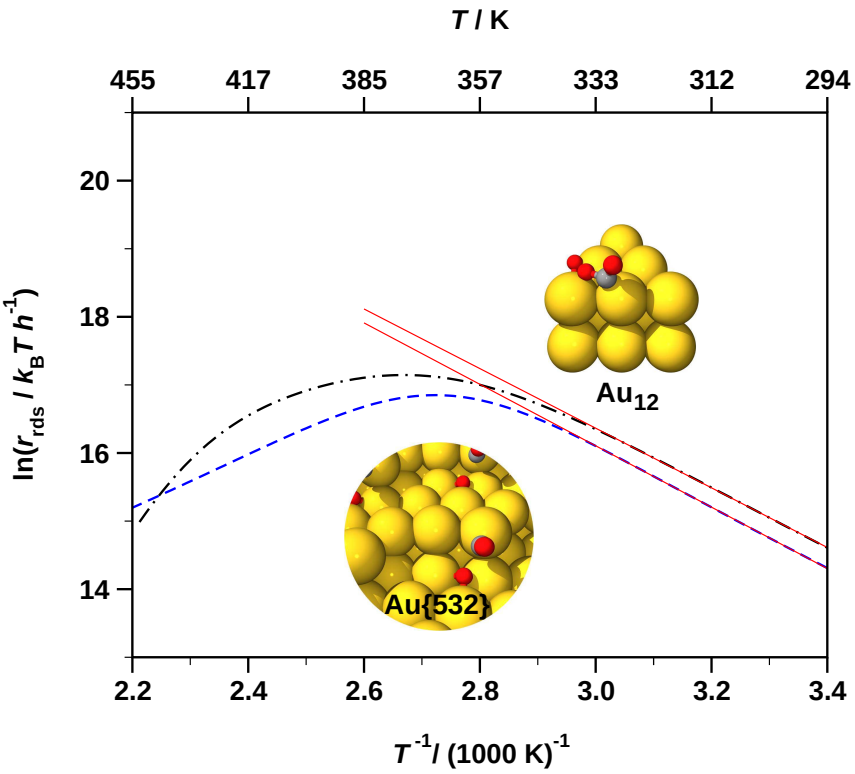

Figure 3.3: Arrhenius plot of the rds reaction rate for CO oxidation by N_2O on Au{532} (blue dashed line) and by O_2 on a Au_{12} cluster (black dash-dotted line) as obtained from the microkinetic model using the DFT transition state structures depicted above [53]. The activation energies (red solid lines) in the low temperature regime (T < 350 K) are shown for ease of comparison with Figure 3.1, and listed in Table 3.2.

regime (T < 350 K). However, at higher temperatures the rate decreases with increasing temperature, with an apex at $T \approx 360$ K.

When using O_2 instead of N_2O to oxidize CO, a Langmuir–Hinshelwood mechanism may again be assumed, so that the elementary steps for (3.R2) may be written as

$$\mathrm{CO(g)} + * \rightleftharpoons \mathrm{CO}* \tag{3.R2a}$$

$$\mathrm{O_2(g)} + {}^{\sun} \rightleftharpoons \mathrm{O_2}{}^{\sun} \tag{3.R2b}$$

$$\mathrm{CO}* + \mathrm{O_2}{}^{\sun} \xrightarrow{\text{rds}} \mathrm{CO_2}* + \mathrm{O}{}^{\sun} \tag{3.R2c}$$

$$\mathrm{CO}* + \mathrm{O}{}^{\sun} \Longrightarrow \mathrm{CO_2(g)} + * + {}^{\sun} \tag{3.R2d}$$

" * " and " ☼ " denote active sites for CO and O_2 respectively, on the Au particle.

Since O_2 is known not to dissociate spontaneously on gold nanoparticles [99], it may be assumed that CO is oxidized directly by O_2 (3.R2c), as discussed in Refs. [53, 65]. Further, (3.R2c) may be assumed to be the rate determining step, so that (3.R2d) occurs relatively quickly. This is justified in the case of high CO coverages, since CO_2 will quickly desorb from the surface.

The gold nanoparticle corner sites were modeled for reaction (3.R2c) using the Au_{12} cluster model described in Ref. [53]. As seen in Table 3.2, such a model yields much higher adsorption energies, particularly for O_2. This is necessary to correctly model (3.R2c) on gold nanoparticles. As shown in the upper inset of Figures 3.3, the transition state for (3.R2d) on the Au_{12} cluster model has the O_2 molecule strongly adsorbed on the corner site, while CO is adsorbed on the edge.

Employing again the microkinetic model, r_{rds} for (3.R2) may be approximated by

$$r_{\text{rds}} \approx \frac{k_{\text{B}}T}{h} \frac{K_{\text{O}_2\text{*}} K_{\text{CO*}} p_{\text{O}_2} p_{\text{CO}}}{(1 + K_{\text{O}_2\text{*}} p_{\text{O}_2})(1 + K_{\text{CO*}} p_{\text{CO}})} \exp\left[-\frac{E_{\text{a}}[\text{rds}] - T S_{\text{CO(g)}}}{k_{\text{B}}T} \right], \tag{3.5}$$

where $K_{\text{CO*}}$ and $K_{\text{O}_2\text{*}}$ are given in (3.3). The necessary activation and adsorption energies for the Au_{12} cluster model are provided in Table 3.2 and the gas phase entropies are taken from Ref. [10].

The temperature dependence of r_{rds} for CO oxidation by O_2 on Au_{12} is shown in Figure 3.3. Again, r_{rds} was found to have an Arrhenius behavior in the low temperature regime (T < 350 K). As with N_2O, we found at higher temperatures the rate decreases with increasing temperature, with an apex at $T \approx 370$ K.

3.3 Trend in Reactivity of CO Oxidation on Gold

Table 3.3 shows the overall trend in activation energies for the reactions measured on Catalysts A, B and C. First, there is a clear size dependence trend from large gold particles with less reactivity to the significantly more reactive smaller ones for all the reactions studied. Second, there is found to be very little difference in activation energy for neither CO nor for H_2 oxidation, irrespectively of the oxidation agent used. This is seen for both experimental and theoretical overall activation barriers, which are in quantitative agreement for Catalyst A (d < 5 nm), in the low temperature regime (T < 350 K), as shown in Table 3.3. However, there is little correlation between the experimental and theoretical reaction rates for the larger Catalyst C. This may be expected, as for larger Au nanoparticles (d > 10 nm), the bulk gold properties may begin to dominate, so that a cluster-based theoretical model is no longer applicable.

It shall first focused on CO oxidation using N_2O according to (3.R1). From the preliminary investigations it may be concluded that in the absence of a reducing agent, the dissociation of N_2O is inhibited. This may be accounted for by the very weak Au–N_2O bond which leads to rapid desorption of N_2O [89]. However, this reaction changes the overall entropy of the system only slightly, since one diatomic and one triatomic species both adsorb and desorb from the surface in (3.R1). This means that although there is only a small N_2O coverage, for high CO coverage experiments the reaction rate should be significant. On the other hand, as seen in Figure 3.3, at higher temperatures (T > 350 K) CO begins to desorb from the surface and the reaction rate begins

Table 3.3: Activation energies in kJ mol^{-1} for CO and H_2 oxidation by O_2 and N_2O, with an uncertainty of ±2 kJ mol^{-1}. Theoretical values obtained using the microkinetic model in the low temperature regime are also provided in parentheses for Catalyst A.

E_a / kJ mol^{-1}	Catalyst A	Catalyst B	Catalyst C
CO + 1/2 O_2	36 (36.4)	38	60
CO + N_2O	37 (37.5)	40	60
H_2 + 1/2 O_2	38	38	61
H_2 + N_2O	39	40	60

to decrease at higher temperatures (T > 360 K). This was impossible to be verified experimentally since gold particle sintering began to occur in this temperature range, as shall be discussed later.

For the case of CO oxidation by O_2 according to (3.R2), there is a significant loss of entropy in the overall reaction, as three diatomic species adsorb, but two triatomic species desorb. Thus a high O_2 adsorption energy is required for the reaction rate to be significant. As this is the case for small gold nanoparticles and the Au_{12} cluster model for a corner site, this model is employed for (3.R2). Even so, at higher temperatures (T > 370 K) the reaction rate is found to decrease significantly as both O_2 and CO begin to desorb from the gold nanoparticle. This may be seen in the reaction rate plots for CO oxidation by O_2 on Catalyst B, shown in Figure 3.1. Here, the reaction rate begins to flatten at about 370 K, in agreement with the theoretical rate shown in Figure 3.3.

Besides the activity, stability is the next most important property of an industrial catalyst. With a view on the gold loading of the catalysts used, noted in Table 3.1, it seems clear that small particles with a high loading are more likely to sinter than with lower loadings. One reason for this is that due to the low melting point of gold [67, 68] or quasi-melting [69], gold particles already become mobile at only slightly elevated temperatures. The larger the particles at a constant loading are, the fewer particles are on the support, and the larger is the distance to their nearest neighbor.

Figure 3.2 illustrates the sintering for different gold particle sizes during the pretreatment, when comparing image (i) with image (ii), as well as during the activity measurements. Since the activity measurements were performed in a sequence (as described above), the change in particle size may be related to 40°C more in heat applied than for the catalytic reactions driven on Catalyst B.

Catalyst A was not heated more than the pretreatment required. This means that the sintering on this catalyst is related only to how the reactions proceeded. Across the general observations published regarding CO oxidation on TiO_2 supported gold using O_2 as an oxidation agent, sintering of nanoparticulate gold has not been reported. Gold nanoparticles have also been found to be a stable catalyst in the presence of H_2 and H_2O [100]. This suggests that the sintering observed on Catalyst A is related to the supply of N_2O. In contrast, the particles of Catalyst C did not significantly sinter, even though the maximum temperature was 80°C higher than the temperature of the pretreatment.

3.4 Summary

Two different reactions were investigated on three TiO_2 supported gold catalysts with two different oxidation agents. Experimental results for CO oxidation on Catalysts A and B agree with both a theoretical model presented here and the literature, following the d^{-3} trend advocated by Nørskov *et al.* [29]. However, Catalyst C was found to have a more bulk-like behavior.

Based on the theoretical model, oxidizing CO by N_2O involves a CO—O transition state, with atomic O adsorbed on the gold B5 sites and CO on the corners. On the other hand, CO oxidation by molecular O_2 occurs via a different reaction pathway, which instead involves a meta-stable CO—O_2 intermediate. In this case, O_2 is strongly adsorbed on gold corner sites while CO is adsorbed on the nearby edge sites (*cf.* Figure 3.2).

However, although the two oxidation agents used proceeded via *different* reaction pathways on *different* active sites, the apparent activation barriers obtained from both theory and experiment were found to be the *same*. From experiment, H_2 and CO oxidation was found to proceed similarly, with common activation energies and rate enhancements when comparing oxidation agents.

Additionally, from the TEM analysis it can be concluded that N_2O oxidation may promote sintering of Au nanoparticles on TiO_2.

CHAPTER 4

Methane Oxidation on Gold

For industry, it is of importance to know how good a catalyst is. Parameters that reflect the catalyst's properties, are activity, stability and selectivity, which this chapter is dedicated to. After identification of the catalyst's properties, optimization may be done by tuning the catalyst's reaction-interacting parameters.

The focus in this chapter is put on low temperature ($\vartheta \leqslant 250^{\circ}\mathrm{C}$) CH_4 oxidation on nano-particulate gold. For determination of the gold's activity, TiO_2 supported gold nanoparticles of different sizes were used. With respect to a metal–support interaction that enhances the activity, different support materials were tested for 2 nm gold particles. The study of particle size and shape showed gold is stabile when CH_4 oxidation proceeds. Although gold is known to be very selective to CO_2 formation [39], traces of C_2H_6 were also found.

4.1 Study of the Effect of Particle Size

The activity of gold for CO oxidation is strongly dependent on the size of the gold catalyst. The aims of this study are to determine whether a similar size dependence is present for gold's activity for CH_4 oxidation, and whether gold is a potential candidate to partially oxidize CH_4 under mild conditions (1 bar, 30°C – 250°C). To approach this challenge, two TiO_2 supported gold catalyst were used:

(A) $Au_{2.0\,nm}/TiO_2$ (1.02 wt% Au), supplied by Project AuTEK [70],
(B) $Au_{3.3\,nm}/TiO_2$ (1.56 wt% Au), supplied by the World Gold Council [71].

The total CH_4 oxidation according to (4.R1) as well as partial CH_4 oxidation (4.R2) shall be considered.

$$CH_4 + 2\,O_2 \longrightarrow CO_2 + 2\,H_2O; \qquad \Delta H^0 \approx -802.3\ \mathrm{kJ\ mol^{-1}} \tag{4.R1}$$

$$CH_4 + \tfrac{1}{2}\,O_2 \longrightarrow CO + 2\,H_2; \qquad \Delta H^0 \approx -185.3\ \mathrm{kJ\ mol^{-1}} \tag{4.R2}$$

Temperature-programmed activity measurements of these supported gold nanoparticles were performed in microreactors and in mini-reactors, that were connected to the QMA and to the GC, respectively. The latter setup was used to confirm the QMA data, since the amount of reaction product was close to the lower detection limit of the QMA setup.

The catalysts used both in the microreactor as well as in the mini-reactor were activated over 10 hours at 100°C. To ensure reproducibility, activity measurements were conducted afterwards with the following scheme for the applied $CH_4 : O_2$ ratio, which was run twice: 2:1, 4:1, 1:2. Reproducibility of the first and the second GC-run was taken as an indication that the catalyst did not change significantly during reactions. For steady-state activity measurements, the temperature was ramped from 50°C to 250°C in steps of 10°C h^{-1} when using the GC and from 75°C to 225°C in steps of 5°C per 5 min when using the QMA.

To avoid the mass-transport controlled regime of the catalyst, self-heating of the exothermic reaction has been kept to a minimum. This can be achieved by operating the catalyst in a range of up to 10% conversion. However, Catalyst A showed already 14% conversion at 220°C. Under these conditions, the greatest amount of heat liberated during the reactions was 7.7 mW.

Concerning the stability of nanoparticular gold, TEM analysis provided information about changes in particle size before and after reaction. Additional HR-TEM images provided both a width estimate and showed which facet of the gold nanoparticle was preferentially attached to the support material.

Prior to the experiments conducted, the average gold particle size was determined to be 2.3 ±0.6 nm for Catalyst A and 3.4 ±0.8 nm for Catalyst B based on a TEM analysis of 97 particles and 60 particles, respectively. Both catalysts are from the same batch as the Catalysts A and B discussed in Chapter 3, shown in the images 3.2(a)(i) and 3.2(b)(i). Thus, the same notation shall be used.

4.1.1 Activity Measurements

At first glance the Arrhenius plot in Figure 4.1 suggests that Catalyst A provided more turnovers than Catalyst B, when comparing the same analysis methods used. This also accounts for the high CO_2 yield measured for CH_4 oxidation on Catalyst A, *cf.* Figure 4.2. Even more important to note is that Catalyst A has a lower apparent activation energy (E_a = 50 ±1 kJ mol^{-1}), than Catalyst B (E_a = 56 ±2 kJ mol^{-1}), *cf.* Table 4.2.

The difference in reaction rate when measured with the QMA or the GC may be related to a morphological change of the catalyst in the GC-runs, since the time the catalyst was exposed to the reactants was 24 hours for each GC measurement as compared to only 3 hours in the case of the QMA. This also accounts for the higher conversion, plotted in Figure 4.2, when the measurement was conducted using a QMA. Since neither CO nor H_2 were detected, the yield of CO_2 is directly given by the consumption of CH_4. The onset of CH_4 oxidation was found at 130°C.

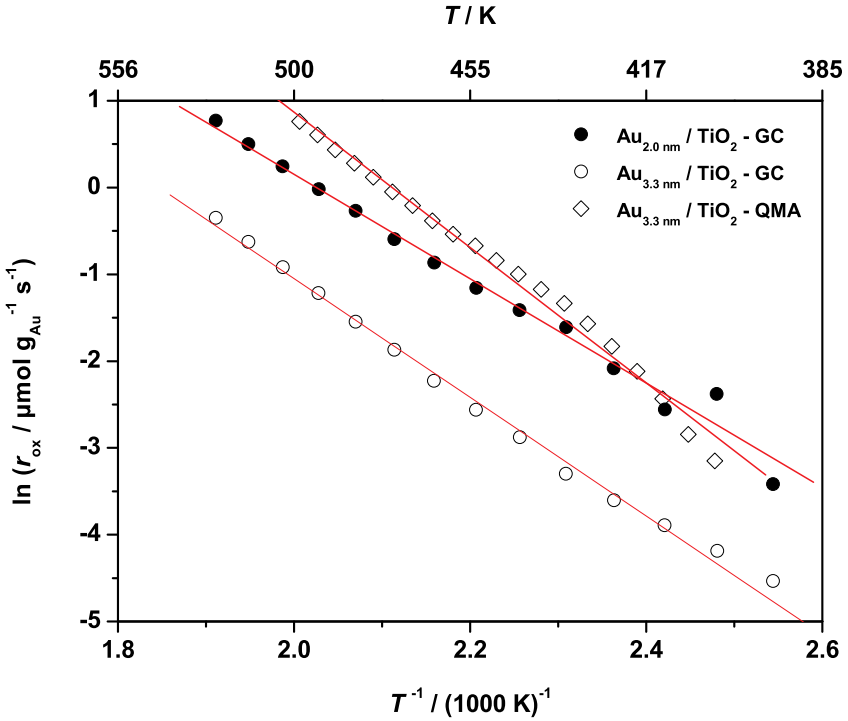

Figure 4.1: Arrhenius plots of the CH_4 oxidation rates for Catalyst A (•) and Catalyst B using the GC (◦) and the QMA (⋄). The uncertainty of E_a is ~ 2 kJ mol^{-1} and 1 kJ mol^{-1}, when using the QMA and the GC setup, respectively.

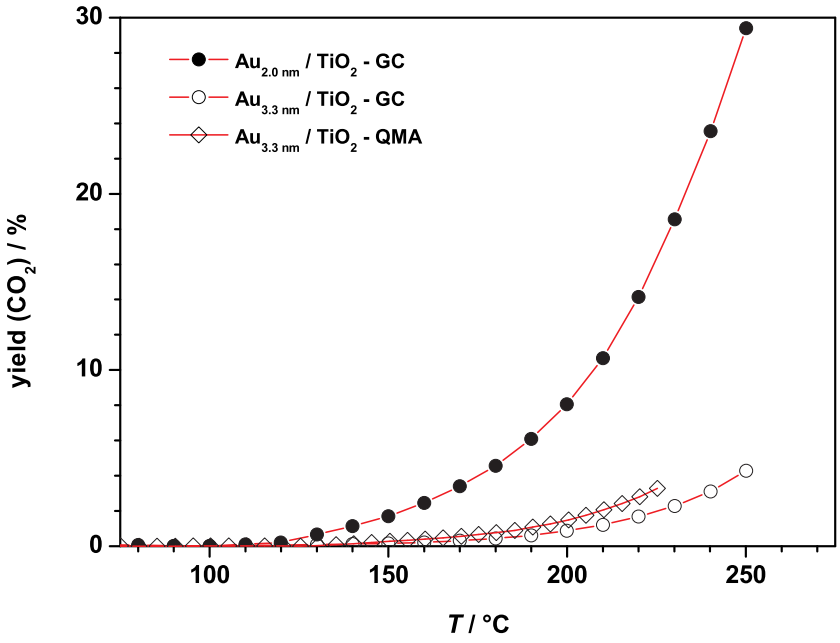

Figure 4.2: CH_4 conversion shows an onset at 130°C for both Catalysts A (•) and B using the GC (◦) and the QMA (⋄).

4.1.2 HR-TEM Analysis

The size distribution of Catalysts A and B was determined using a PHILIPS Technai 20T HR-TEM that was operated at 200 kV. Specimens of the catalyst were taken before and after the temperature-programmed activity measurements, and prepared on a carbon TEM grid.

Besides standard HR-TEM images, a high-resolution image of Catalyst A was acquired using a Jeol 2200 FEG-TEM, operating at 200 kV and with a coefficient of spherical aberration of C_S = -30 µm. Figure 4.3 shows a 2.8 nm gold particle on TiO_2, that has the shape of a cuboctahedron. The inset provides an illustration of the diffraction pattern of the image.

From these data, a 3D reconstruction of the gold particle was possible and it may be assumed that the particle as well as the area around the particle–support interface (blue arrows) are partly oxidized. Additionally, as illustrated in Figure 4.4, some areas seem to be covered by the support material (indicated by black arrows).

The TEM-analysis of Catalyst B after the entire sequence of steady-state CH_4 oxidation measurements in the GC shows that the particles now have a broad range of sizes (2 – 7 nm). By tilting the specimen from -65° to +65°, the three dimensional structure of the particles may be reconstructed. This was done for one particle that represents the determined average size. Figure 4.5 shows a TEM image of a 4.8 nm gold particle with its 3D reconstruction (see inset). This particle is found to adhere to the support via its (111) surface, as indicated by the arrow.

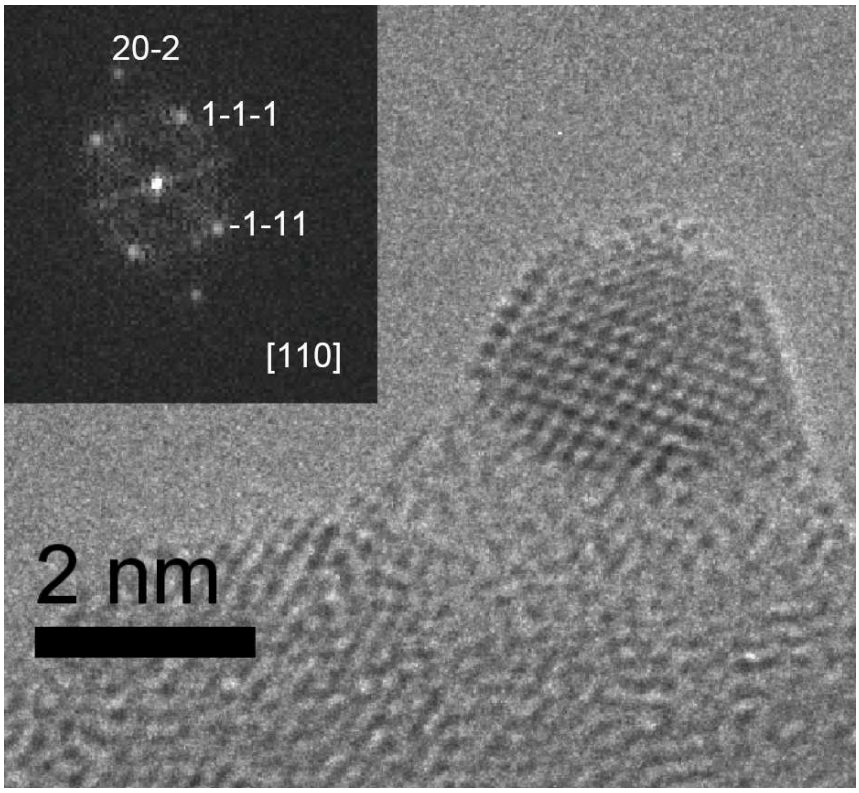

Figure 4.3: High resolution TEM image of a 2.8 nm gold particle of Catalyst A after steady-state activity measurements and the diffraction pattern in the inset.

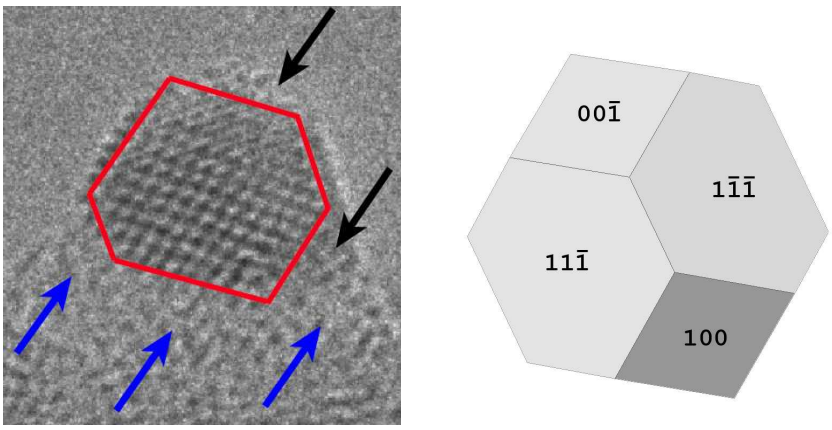

Figure 4.4: Cuboctahedron shape of the particle shown in Figure 4.3. On the left, the blue arrows point at partly oxidized areas, whereas the black arrows indicate areas that are covered by the support. A 3D reconstruction is illustrated on the right.

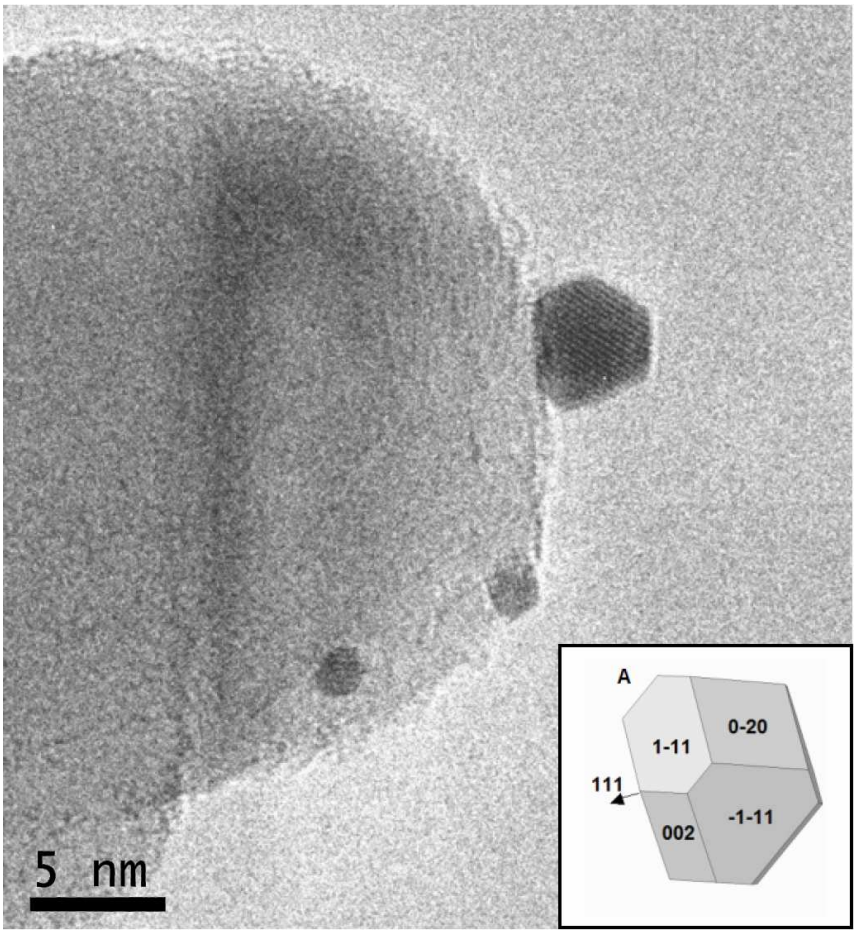

Figure 4.5: High resolution TEM image of a 4.8 nm gold particle of Catalyst B after steady-state activity measurements.

4.1.3 CO and H_2 Oxidation as a Part of the CH_4 Oxidation Pathway

The first step in determining the reaction mechanism is to identify the species formed. In the case of partial oxidation, it can be assumed (due to the stoichiometry of the reaction) that if CO were to be formed during CH_4 oxidation, then H_2 would according to (4.R2) also be formed. In fact, on both catalysts H_2 evolution was not observed, a first indication of the lack of partial oxidation. Furthermore, H_2O formation was observed during the CH_4 oxidation in proportions that match the stoichiometry expected from (4.R1). From this it can be concluded that complete combustion to form CO_2 has occurred.

The parallel running fits for CO and H_2 oxidation in the Arrhenius plot (*cf.* Figure 3.1(a)) indicate similar activation energies for both reactions on Catalyst A. In actual fact, as indicated in Chapter 3, the apparent activation energy for the CO and the H_2 oxidation reactions were determined on both Catalyst A and B to be approximately the same. For ease of comparison, these important results of the previous studies on the oxidation of H_2 and CO presented in Chapter 3, as well as the results of these temperature-programmed activity measurements, are summarized in

Table 4.1: Comparison of activation energies, reaction rates and yields for each, Catalyst A and Catalyst B, determined using the GC.

reaction	E_a / kJ mol^{-1}	$\ln(r_{ox}$ / μmol $g_{Au}{}^{-1}$ $s^{-1})$	yield ($CO_2{}^{\dagger}$, $H_2O^{\ddagger}$) / %
Catalyst A			
$CH_4 : O_2$	50 ±1	0.02 (at 220°C)	14 (at 220°C)†
$CO : O_2$	36 ±1	6.8 (at 60°C)	13 (at 60°C)†
$H_2 : O_2$	38 ±1	5.4 (at 60°C)	3 (at 60°C)‡
Catalyst B			
$CH_4 : O_2$	61 ±4	-1.2 (at 220°C)	2 (at 220°C)†
$CO : O_2$	38 ±0.6	8.2 (at 80°C)	40 (at 80°C)†
$H_2 : O_2$	38 ±0.8	6.4 (at 80°C)	8 (at 80°C)‡

Table 4.1.

The results listed in Table 4.1 suggest that even if CO was formed from partial oxidation, CO and H_2 could easily be post oxidized to CO_2 and H_2O. This is due to the fact that when compared to CH_4 oxidation, the higher reaction rate for CO and H_2 oxidation (which is coupled to their lower apparent activation energies 38 ±0.6 kJ mol^{-1}), indicates that under these reaction conditions these elementary steps would be quasi-equilibrated.

4.2 Study of the Support Effect

Low temperature CH_4 oxidation was studied on 2 nm gold nanoparticles supported on various metal-oxides:

(A) Au/TiO_2 (1.02 wt% Au),
(B) Au/ZnO (0.978 wt% Au),
(C) Au/Al_2O_3 (0.84 wt% Au).

According to the supplier Project AuTEK [70], these catalysts (AURO*lite*™) had been prepared by carefully developed methods involving gold precipitation from solution. A preliminary XRF analysis of each catalyst is taken as proof of an impurity-free sample.

The gas chromatograph did not possess a high enough sensitivity to perform steady-state activity measurements on these catalysts for CH_4 oxidation in microreactors. Consequently, the results presented in this chapter are based on measurements that were conducted in mini-reactors, that were connected to a GC. These mini-reactors are basically quartz glass tubes with approximately

50 times larger reactor volume than that of the microreactors. The reactants used had a purity of 5.5N for CH_4 and 3.5N for O_2.

To ensure reproducibility of the steady-state activity measurements, each catalyst was first activated by a pretreatment of 10 hours at 100°C. A continuous gas flow of CH_4 and O_2 in the ratio of 1:2 as well as a temperature ramp from 30°Cto 250°Cin steps of 10°C h^{-1} was used. The following sequence of $CH_4 : O_2$ ratios was used: 1:2, 1:1, 2:1. The reaction according to the first step of the sequence was re-measured to confirm that the catalyst did not change during the reactions. To verify that the applied gases did not alter the catalysts, the described schemes were run once more in reverse order using a fresh catalyst. For steady-state activity measurements, the temperature was ramped from 30°Cto 250°Cin steps of 10°C h^{-1}.

Self-heating of the catalyst during an exothermic reaction is difficult to avoid, but may be minimized by operating the catalyst in the lower range of its kinetically controlled regime. The greatest amount of heat liberated during the reaction was 16.9 mW when CH_4 and O_2 were applied in the stoichiometric ratio to form CO_2 and H_2O at 250°C.

Besides the activity measurements, the issue of stability was also addressed. A thorough TEM analysis was applied to the catalysts as they were supplied, as well as before and after the activity measurements.

4.2.1 Preliminary Analysis

To confirm the particle size and purity stated by the supplier for each catalyst, both TEM and XRF were used. Since the TEM analysis is discussed separately, it shall only be mentioned here that the average particle size of the catalysts, 2.0 nm, as stated by the supplier, could be confirmed for the Catalysts A and B, whereas Catalyst C was found to be larger (2.8 ±1.3 nm). Since Al_2O_3 is not a reducible metal oxide like TiO_2 or ZnO, upon which oxygen vacancies usually act as anchoring points for deposited nanoparticles, an enhanced sintering effect cannot be excluded. Most probably the gold particles were already sintered during storage.

The XRF analysis of the Catalysts A, B and C as they were supplied does not show significant impurities, *cf.* Figure 4.6. For Catalyst C, the aluminum signal appears very weak. This is reasonable since the sensitivity of the spectrometer is lower for lighter elements. It is recommended to analyze such elements in a helium atmosphere. However, this analysis was conducted without helium background. In point of fact this may explain why possible impurities appear in this spectrum with a stronger peak. In particular, there is a pronounced rhodium signal which is characteristic of the rhodium anode of the spectrometer.

4.2.2 Activity of Gold Nanoparticles

From the Arrhenius plots in Figure 4.7, the apparent activation energy for CH_4 oxidation on the three different catalysts was determined to be approximately the same for the feed gas ratio of

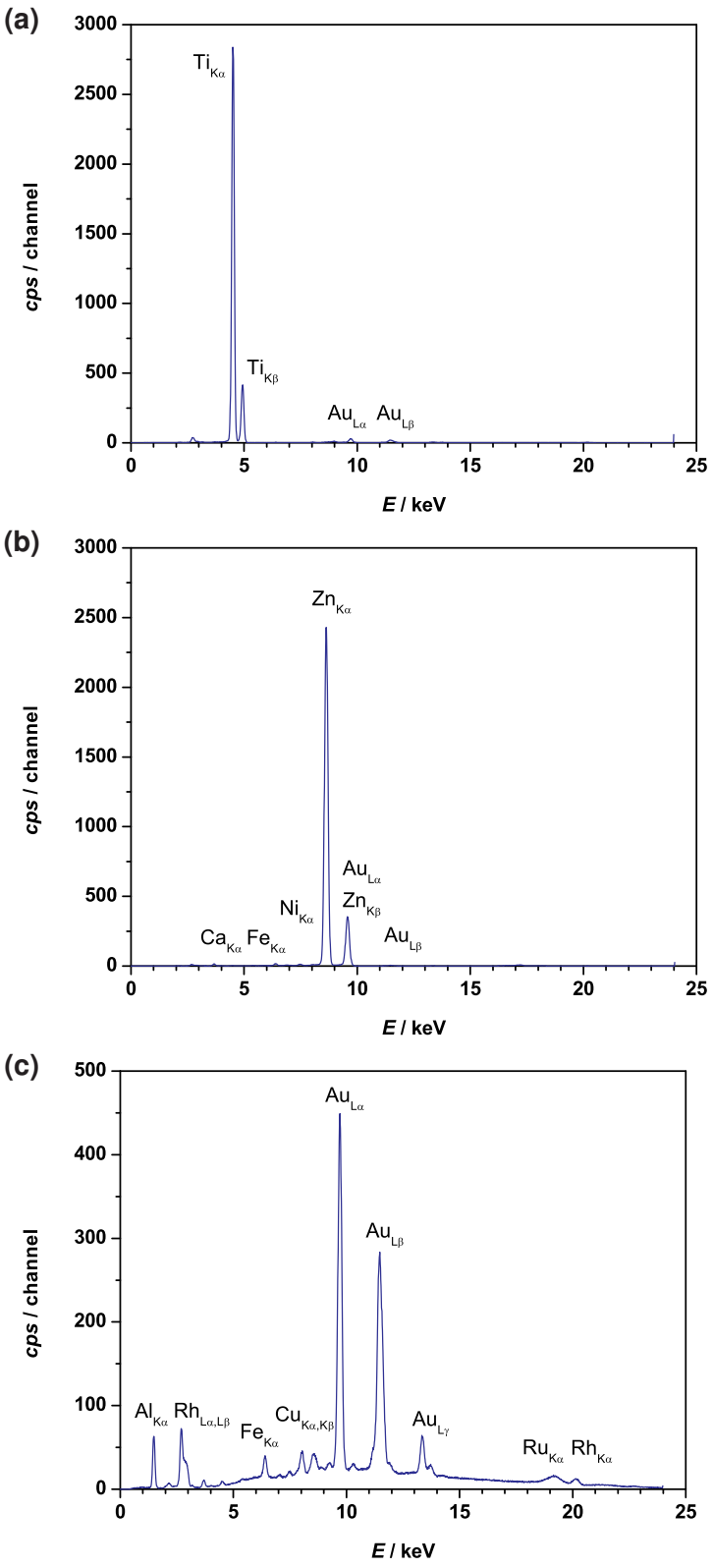

Figure 4.6: XRF analysis of Catalysts A, B and C as they were supplied in the Figures (a), (b) and (c), respectively.

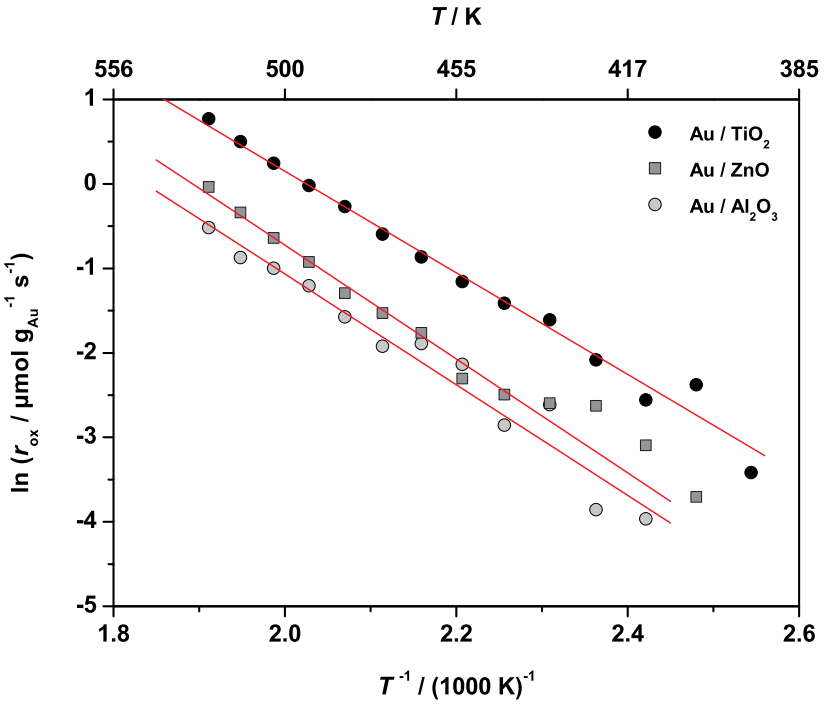

Figure 4.7: Arrhenius plots of the specific CH_4 oxidation rates: Catalyst A (•), Catalyst B (■), Catalyst C (○). The apparent activation energies are summarized in Table 4.2.

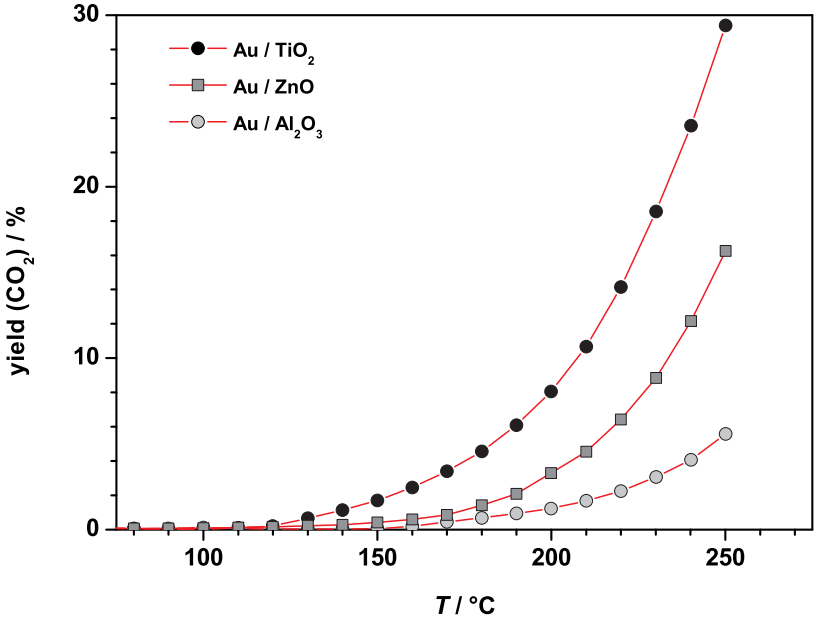

Figure 4.8: CH_4 conversion begins at 130°C when using Catalyst A (•), whereas for the Catalysts B (■) and C (○), the onset of conversion is around 150°C.

Table 4.2: Comparison of activation energies, reaction rates and yield of CO_2 at 250°C as well as the particle size determined using TEM.

	d_{Au} / nm	E_{a} / kJ mol^{-1}	$\ln(r_{\mathrm{ox}}$ / μmol $g_{\mathrm{Au}}{}^{-1}$ $s^{-1})$	yield (CO_2) / %
Catalyst A	1.8 ±0.6	50 ±1.1	0.77	29.4
Catalyst B	2.3 ±0.6	56 ±1.7	-0.04	16.3
Catalyst C	2.8 ±1.0	53 ±3.4	-0.52	5.6

$CH_4 : O_2$ = 1:2. The values are summarized in Table 4.2. The specific CH_4 oxidation rate indicates clearly that Catalyst A was the most active one. For this catalyst, the conversion of CH_4 to CO_2 according to (1.R6) was greatest with 29% at 250°C, as shown in Figure 4.8. Since neither CO nor other organic chemicals were detected for this feed gas ratio, which according to (1.R3) – (1.R5) would be an indication that partial CH_4 oxidation occurs, the yield of CO_2 is directly given by the consumption of CH_4. The onset of CH_4 oxidation was found to be 130°C for Catalyst A. On the other catalysts, CH_4 oxidation did not take place at temperatures below 150°C.

Table 4.2 shows that the support material has only a marginal effect on the apparent reaction energy. The apparent activation energies did not vary significantly. Concerning the specific rate for CH_4 oxidation, Catalyst A provided the highest turnover numbers of all the catalysts tested. This is most probably related to the fact that Catalyst A had the smallest gold nanoparticles. Keeping in mind that all the catalysts used were prepared by the same preparation method, it may be concluded from these results that TiO_2 is a good support for catalytically active gold. Compared to the prior discussion on CO oxidation, it should be noted that the specific oxidation rate for CH_4 oxidation is, however, more than 150,000 times less than that for CO oxidation on a catalyst of the same batch. This was already observed at a temperature of 80°C (as discussed in Chapter 3).

4.2.3 Stability of Gold Nanoparticles

It has to be kept in mind that stability is the next most important property of a catalyst for industry. TEM investigations shall support the analysis of the catalysts with respect to sintering throughout the CH_4 oxidation study. The recording and post-processing of the TEM images were done by Dr. Lionel Cervera–Gontard at the Center for Electron Nanoscopy at the Technical University of Denmark.

The size distribution and shape of the gold particles were probed using a Tecnai 20T TEM operating at 200 kV. Specimens of the catalyst were taken before and after the temperature-programmed activity measurements, and prepared on a carbon TEM grid. Detection of particles in a TEM image is usually performed by transforming the grayscale image into a binary image by *thresholding* the *whole* picture at once using a 'global threshold' value. This approach works well if all of the particles are dark enough with respect to the background intensity in the image, but often fails because of local changes in the contrast of the TEM image. Here, instead, an algorithm based on local thresholding was applied to improve the detection of the particles.

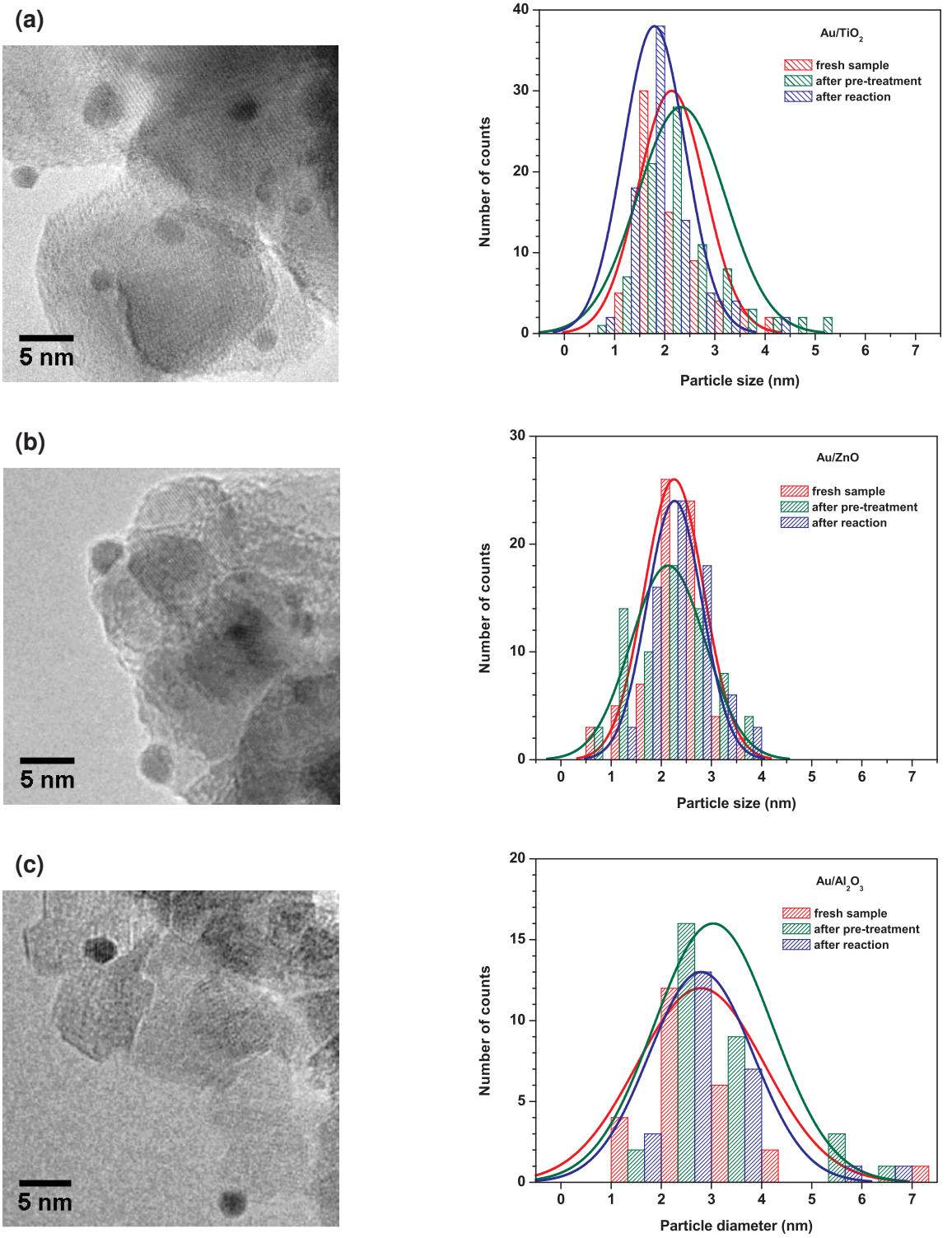

Figure 4.9: TEM analysis of Catalysts A, B and C after CH_4 oxidation reaction together with statistical analysis of the average particle size from all states of the catalyst — fresh (as supplied), after pretreatment and after reaction — in the Figures (a), (b) and (c), respectively.

Figure 4.9(a) shows a typical TEM image of Catalyst A after reaction. Remarkably, the particle size did not change drastically, either during the pretreatment — *cf.* the red and the green distribution curves, or due to methane oxidation — *cf.* the green and the blue distribution curves in the graph below. After the reaction, the gold particles' size was determined to be 1.8 ±0.6 nm based on a TEM analysis of 81 particles. This behavior is in strong contrast to measurements after CO oxidation over a fresh catalyst of the same batch, presented in Chapter 3, where substantial sintering was found. This suggests that CO oxidation on the same material as used for Catalyst A might have been affected by the use of a different oxidation agent, N_2O.

The TEM image in Figure 4.9(b) shows gold particles observed after reaction on Catalyst B. The average particle size was determined to be 2.3 ±0.6 nm. This catalyst was also very stable, since the particle size did not change significantly.

In its 'as supplied' state, Catalyst C contained larger gold particles. The measurement of particle sizes from TEM images was difficult due to the high contrast of the Al_2O_3 crystals supporting the nanoparticles, and curves must be interpreted with caution. However, the size distribution indicates average particle sizes greater than that of the other two catalysts. After the reaction, the average particle size was still 2.8 ±1.0 nm.

From these observations, nanosized gold seems to be inhibited from sintering during CH_4 oxidation. A similar non-sintering phenomenon was reported for alumina supported gold catalysts when $3d$-metal oxides were added [47]. However, it also has to be borne in mind that the catalysts in that study were first calcined at 400°C in O_2, which led to sintering. Thus the particle size and the —still unidentified— active sites available, are not comparable with those of Catalyst C in our study. The results presented in this thesis are based on temperature-programmed reaction experiments that had kept the catalyst at or above 200°C for 30 hours. To clarify whether this observed behavior is associated with CH_4 or OH present during the reaction, further research needs to be done.

4.2.4 Selectivity of Gold Nanoparticles

As can be shown, Catalyst A has the ability to provide the greatest amount of turnovers from CH_4 to CO_2 for an applied feed gas ratio of $CH_4 : O_2$ = 1:2. When screening for other reaction products to determine the selectivity of gold nanoparticles to CO_2, it is worth mentioning that traces of C_2H_6 could only be detected on Catalyst A. This was when the feed gas of reactants was applied in a ratio of $CH_4 : O_2$ = 2:1. Considering the reaction represented by (4.R3) the greatest yield of C_2H_6 would be expected for $CH_4 : O_2$ = 4:1.

$$2\ CH_4 + {}^1\!/_2\ O_2 \longrightarrow C_2H_6 + H_2O; \qquad \Delta H^0 \approx -176.9\ \mathrm{kJ\ mol^{-1}} \tag{4.R3}$$

This could be confirmed in a separate set of measurements, *cf.* Table 4.3. However, the yield only doubled to 0.03% at 250°C, whereas the yield of CO_2 dropped down to 13%. No other products could be detected.

Concerning the measured C_2H_6, three points are worth mentioning: (a) The measurements with a

Table 4.3: Comparison of yields in CO_2 and C_2H_6 for different $CH_4 : O_2$ feed gas ratios applied to Catalyst A at ϑ = 250°C.

$CH_4 : O_2$	yield (CO_2) / %	yield (C_2H_6) / %
1 : 4	24.6	0.01
1 : 2	29.4	0.00
1 : 1	21.8	0.02
2 : 1	16.7	0.02
4 : 1	12.9	0.03

$CH_4 : O_2$ ratio of 4:1 show an enhancement in the C_2H_6 yield compared to those where the ratio is 2:1. First, it may be concluded that C_2H_6 is a byproduct of the reaction studied. Second, since the yield was only 0.03% in C_2H_6, gold has a high selectivity for CO_2. (b) Comparing (1.R4) and (4.R3), C_2H_6 formation is thermodynamically less likely than HCHO formation. The reason why C_2H_6 is instead formed needs further investigation. (c) The presence of C_2H_6 suggests that there must be a pathway to partially oxidize CH_4 such that carbon goes from the oxidation state -Ⅳ to -Ⅲ.

4.3 Oxidation of CH_4 on Au/TiO_2 — A DFT Study

To corroborate the experimental findings presented in this chapter, DFT calculations were carried out by investigating the thermodynamics of CH_4 oxidation on a stepped Au{211} surface. The calculations were mainly performed by Dr. Glenn Jones at the Center for Atomic-scale Materials Design at the Technical University of Denmark.

Prior to the calculations, some of the issues surrounding the {211} surface as a model system shall first be addressed. This particular surface facet was chosen because recent experimental and theoretical work has demonstrated the importance of the B5 site in catalytic activity for N_2 dissociation and CH_4 activation on Ni [101]. If one looks at the {211} surface, it may be seen that the step sites are made up of B5 sites. Therefore this surface is expected to be a good model of the edges and steps present on a nanoparticle. Some care does however need to be taken because corner sites may also be implicated in the activity of a catalyst. In fact, this is the subject of ongoing research. However, in the present case the model should be sufficient to explain the reactivity.

4.3.1 Theoretical Methodology

DFT was used as implemented in the computer code DACAPO [91] using the RPBE exchange correlation functional [93]. Calculations for stepped model gold surfaces were carried out using fcc crystals terminated at the $\{211\}$ facet. Unit cells of (2×1) periodicity were used with a depth of 10 atomic layers (roughly equivalent to 3-close packed layers) and a vacuum region of 10 Å. An electronic planewave cut-off of 340 eV has been used with the Brillouin zone being sampled by a Monkhorst-Pack [102] mesh of 4×4×1 **k**-points. Pseudopotentials of the Vanderbilt [92] type were used to describe the electronic core regions.

As in Chapter 3, thermodynamic analysis was carried out using the total energies obtained from the DFT calculations. The free energies had been calculated by employing standard formulas for the thermodynamics of a classical ideal gas [96]. For a gas-phase species (X) at temperature (T) and pressure (p), the Gibbs free energy ($G_{\mathrm{X}}(p,T)$) is given by:

$$G_{\mathrm{X}}(p,T) \quad = \quad E_{\mathrm{X}} + E_{\mathrm{ZPE}} + \Delta H(T) - TS(T) + RT\ln(p/p_0),$$

where E_{ZPE} is the zero point energy, $\Delta H(T)$ is the enthalpy change due to raising the temperature from 0 K to T, $S(T)$ is the entropy at T, R is the universal gas constant and p_0 is standard pressure (taken to be 1 bar).

The potential energy of the adsorbed species (X*), $E_{\mathrm{X}*}$, is given by: $E_{\mathrm{Au/X}*} - E_{\mathrm{Au}}$, where E_{Au} is the energy of the clean Au surface and $E_{\mathrm{Au/X}*}$ is the energy of the adsorbate and surface system. In order to calculate the free energy of this species, the pressure term was neglected so that the enthalpy change is replaced by the change in internal energy. This leads to the following expression for the free energy ($G_{\mathrm{X}*}(p,T)$):

$$G_{\mathrm{X}}(p,T) \quad = \quad E_{\mathrm{X}*} + E_{\mathrm{ZPE}} + \Delta U(T) - TS(T). \tag{4.1}$$

In contrast to Chapter 3, vibrational frequencies were used to determine E_{ZPE}, $\Delta U(T)$ and $S(T)$, which were calculated within the harmonic approximation. For more details, one is referred to Paper 1.

4.3.2 Thermodynamics of CH_4 Oxidation on Au$\{211\}$

Figure 4.10 illustrates the standard free energy diagram for the stable species present in the oxidation of CH_4 at 450 K. This was constructed using the DFT total energies in combination with the thermodynamic corrections as outlined in the methodology. Three possible pathways were depicted, partial oxidation terminating at CO(g) and H_2(g), also at CO_2(g) and H_2(g) and finally complete combustion to CO_2(g) and H_2O(g). The diagram shows a route which goes via a methoxy intermediate followed by carbonyl species on the surface prior to the formation of CO(g) (CO_2(g)). It was found that if one went via a route of direct dehydrogenation of CH_4 then the thermodynamic barriers were extremely high (in excess of 4 eV for the formation of C* + 2 H_2(g) from CH_4). It can be seen that this route still contains the difficult initial dehydrogenation of

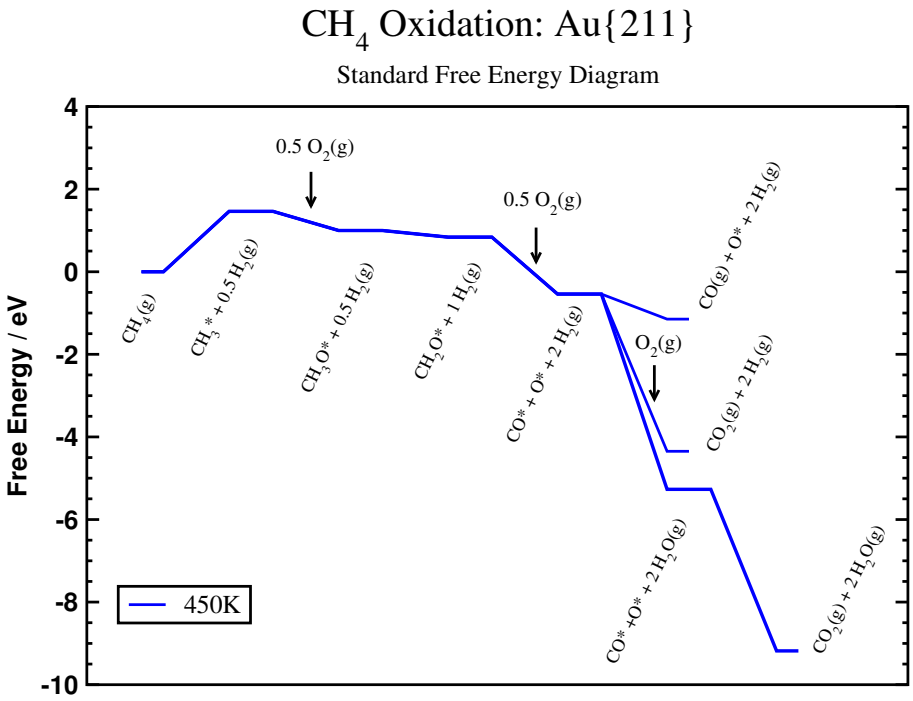

Figure 4.10: Standard free energy reaction profile for the stable intermediates present in the oxidation of CH_4 as determined from DFT.

CH_4, which is 1.4 eV uphill. However, once this step is overcome the pathway is entirely downhill to the products. Here it may be seen that complete combustion is by far the most thermodynamically favored reaction. Consequently (subject to kinetic barriers) one would expect the reaction to proceed to this point. Indeed, this is found to be the case experimentally, where partial oxidation is not observed.

4.4 Summary

As it has been found to be quite challenging to calculate the kinetics for CH_4 oxidation on gold, the experimental results obtained under mild conditions (1 bar, 30°C – 250°C), shall be compared with the findings from a simple theoretical model based only on the thermodynamics.

If one looks at the thermodynamic picture presented from theory, one is able to gain insight into whether a particular reaction is feasible. In fact, what can be seen from Figure 4.10 is that both partial CH_4 oxidation and complete CH_4 combustion are exothermic at 450 K. This means both processes are likely to proceed. However, CO_2(g) formation is more favored and in the absence of kinetic considerations, would dominate the oxidation process. Experimentally, there has never

been observed any evidence for the formation of CO(g) or H_2(g) above that of the background noise.

In order to go beyond the thermodynamic picture, one needs to consider the barriers present in the reaction pathway. Recent work by Nørskov *et al.* has studied the oxidation of CO on a model nanoparticle [29]. Their work demonstrates that there are two possible routes by which complete oxidation can proceed. The first is by reaction with adsorbed atomic oxygen O* (* denotes an adsorbed species). The second is through an intermediate that involves molecular oxygen. This is generally perceived to proceed via a physisorbed precursor. This particular mechanism has also been highlighted in Chapter 3 and actually represents the tail of the reaction pathway of CH_4 oxidation.

From the experimental results on size dependency, it may be concluded that on particles with the sizes investigated here, only complete combustion of CH_4 takes place. It is shown that the lower overall barrier for CO oxidation 36 kJ mol^{-1} *vs.* 50 kJ mol^{-1} for CH_4 oxidation on 2.3 nm Au/TiO_2 and 38 kJ mol^{-1} *vs.* 61 kJ mol^{-1} for CH_4 oxidation on 3.4 nm Au/TiO_2 (*cf.* Table 4.1)). This indicates that under these reaction conditions the post-oxidation of CO proceeds much faster than the oxidation of an adsorbed CH_4 species. Thus, for the overall reaction of CH_4 oxidation, the elementary steps following the formation for CO_2 would be quasi-equilibrated. It is suggested that in a similar fashion the elementary steps for H_2 may well be quasi-equilibrated on TiO_2 supported gold catalysts. Support for this viewpoint is provided by the fact that the overall barrier for H_2 oxidation is much lower as well (38 kJ mol^{-1}). Furthermore, atomic H (liberated from CH_4) might perhaps already form H_2O at an even lower activation barrier. This means that CH_4 oxidation is the rate-limiting step of the overall reaction for the different sizes of gold catalysts tested.

Another interesting issue is the strong tendency to form CO_2 irrespective of the support used (TiO_2, ZnO, Al_2O_3), as can be seen in the activity measurements presented in Section 4.2. During CH_4 oxidation, it was observed that H_2O and CO_2 formed in a stoichiometric ratio as expected from (4.R1). From this result, it may be concluded that complete combustion of CH_4 takes place over all supports. Following the argument above, the rate-limiting step of the overall reaction for each of the support materials tested is again determined by the oxidation of CH_4.

CHAPTER 5

Conclusion and Outlook

In the present work, CH_4 oxidation was investigated on nanoparticulate gold catalysts of different size under mild conditions (p = 1 bar, $\vartheta \leq 250°C$). From the experimental results, it can be concluded that only complete combustion of CH_4 takes place. However, the apparent activation energy was found to be **dependent mainly on the particle size**, while the support material has a minor influence. From a detailed TEM analysis on the size distribution, nanoparticular gold was found to be very stable against sintering.

Experiments were also performed to highlight the elementary steps in the tail of the CH_4 oxidation pathway, which are CO and H_2 oxidation. For CO oxidation, the results obtained on industrial powder catalysts with a particle size below 5 nm are in agreement with the literature and the theoretical model presented. Although the two oxidation agents used proceeds via *different* reaction pathways on *different* active sites, the apparent activation barriers obtained from both theory and experiment were found to be the *same*. These barriers are smaller than the barrier for CH_4 oxidation, and they **do not indicate any dependency on the particle size**. This may be taken as an indication that the number of active sites is constant for small particle sizes, such as the number of corner atoms on clusters and nanoparticles.

For large gold nanoparticles, as they were used in this work, it is clearly shown that the rate determining step for CH_4 oxidation is not associated with the post-oxidation of CO and H_2 liberated from CH_4. From the thermodynamic picture (*cf.* Figure 4.10) the rate determining step is expected to be associated with the initial dissociation of an atomic H from CH_4. This barrier was found to decrease for smaller particle sizes. **If this trend continues**, the rate determining step of CO oxidation may at some point also determine the apparent activation barrier for CH_4 oxidation.

In terms of future work, it may be possible to find a particle size (d') such that the mechanism for CH_4 oxidation is no longer dependent on the rate determining step for CH_4 dissociation, but rather on that for CO oxidation. To clarify this, supported gold catalysts with a gold particle size

below 2 nm should be considered for future study. At such small particle sizes sintering may occur more rapidly, so that other preparation techniques, such as physical vapor deposition become more appropriate. With respect to the microreactors used in this study, the number of active sites will be drastically reduced. Thus, either the amount of catalyst needs to be increased (e.g. by numbering up the microreactors), or a more sensitive gas sampling device needs to be developed. In terms of sensitivity, a cavity ring-down spectrometer may solve the problem.

In general, such results are reasons for optimism that catalysis by gold might be used for more and more non-academic purposes. Although the reaction rate for CH_4 oxidation was determined to be 150,000 times lower than that of CO oxidation, the most important property of an industrial catalyst is selectivity. Thus, potential opportunities for the use of gold in catalysis need to be considered and evaluated carefully by both industry and academia.

APPENDIX A

Fabrication of Microreactors

Micro-fabricated reactors are silicon chips, fabricated on a 350 μm thick silicon wafer. First, the silicon wafer was etched from the back side, to make the inlet and outlet holes, and for certain vacuum applications a 3 μm wide sniffer hole as well. Then, the capillary system and the reactor chamber were etched from the front side. On both sides Advanced Silicon Etching (ASE™) was applied, whose primary technology is based on the so-called Bosch process [103, 104].

Before the etching, the structure of the areas that have to be etched had to be superposed onto the wafer using photo lithography. For this purpose a 2.2 μm thick layer of a photo sensitive polymer was deposited on the whole wafer and exposed to UV light through a metal shadow mask. The UV-light breaks the chemical bonding of the polymer, which can then be dissolved in NaOH and removed from the surface of the wafer. In this way the desired areas are exposed for the etching process, whereas the other surface is protected by the photo resist. Then, the substrate is exposed to a plasma, generated by a radio frequency (RF) electric field, in which sulfur-hexafluoride is dissociated regarding Equation A.R1 [105].

$$\mathrm{SF_6 + e^- \longrightarrow} \begin{cases} \mathrm{SF_5 + F + e^-} & \text{impact dissociation} \\ \mathrm{SF_5^- + F} & \text{dissociative attachment} \\ \mathrm{SF_5^+ + F + 2e^-} & \text{impact ionization} \end{cases} \tag{A.R1}$$

Accelerated SF_5^+ ions etch the silicon wafer by physical bombardmen (an-isotropic), whereas the aggressive fluorine radicals etch chemically (isotropic) and evaporate as SiF_4. After a few seconds, this process is stopped to avoid lateral isotropic etching of the vertical sidewalls of the trenches and the gas composition is changed to C_4F_8. The C_4F_8 plasma deposits a teflon-like polymeric passivation layer of $(CF_2)_n$ on the surface. The protection layer on the horizontal surfaces can be removed by ion bombardment in another cycle of the pulsed plasma etching, whereas surfaces parallel to the ion beam are protected against sidewall etching. These sequentially alternating

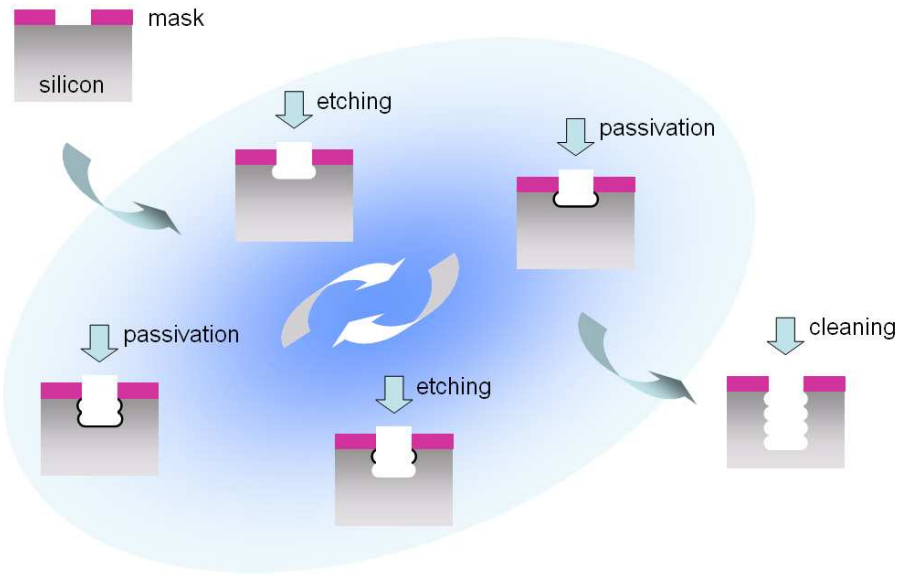

Figure A.1: Schematic drawing of the ASE™-process. Details are explained in the text.

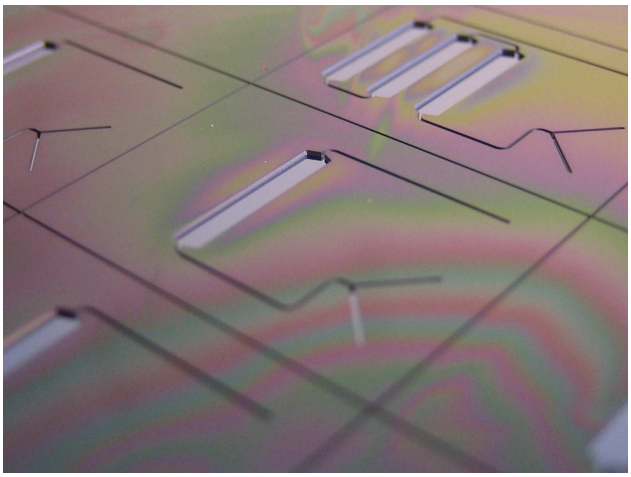

Figure A.2: Close-up of a 10 inch silicon wafer containing 20 microreactors, 16 single bed and 4 multi bed reactors of a standard size of 15 mm × 20 mm chip. The reactor chamber measures (10 × 1.5 × 0.27) mm^3.

etch and passivation steps enhance anisotropic etching [105, 106, 107]. Figure A.1 illustrates this multi-repeated technique, which is applied until the required depth is achieved.

A close-up of the result of an etched wafer is shown in figure A.2. For a more detailed description of the individual fabrication steps, the reader is referred to the PhD thesis of Søren Jensen [105].

APPENDIX B

Agilent 3000 Micro-GC Settings

Table B.1: Settings of the carity-method of the Agilent 3000 Micro-GC used

	column A	**column B**
3000 Micro-GC configuration		
injector type	timed	back-flush
carrier gas	Ar	Ar
column type	5 m PLOT U	10 m mol. sieve
detector type	TCD	TCD
3000 Micro-GC setpoints		
sample inlet temperature / °C	90	same as A
injector temperature / °C	70	90
column temperature / °C	60	70
sampling time / s	10	same as A
inject time / ms	100	100
run time / s	600	600
post run time / s	60	60
pressure equilibration time / s	60	60
column pressure / psi	30.00	30.00
post run pressure / psi	45.00	45.00
detector data rate / Hz	50	50
back-flush time / s	n/a	10.0

Bibliography

[1] M. W. Roberts, *Catal. Lett.* **67**(1), 1 (2000).

[2] B. Hammer and J. K. Nørskov, *Nature* **376**(6537), 238 (1995).

[3] I. Chorkendorff and J. W. Niemantsverdriet, *Concepts of Modern Catalysis and Kinetics*, student edition ed. (John Wiley and Sons Ltd, Weinheim, 2003).

[4] B. Hammer and J. K. Nørskov, *Adv. Catal.* **45**, 71 (2000).

[5] T. Bligaard and J. K. Nørskov, *Electrochim. Acta* **52**(18), 5512 (May 2007).

[6] B. Hammer and J. K. Nørskov, *Theory of adsorption and surface reactions* (Kluwer Academic Publishers, 1997), vol. 331 of *NATO ASI Series E*, p. 285.

[7] M. Boudart, *Chem. Rev.* **95**(3), 661 (May 1995).

[8] G. C. Bond, C. Louis, and D. T. Thompson, *Catalysis by Gold*, 1st ed. (Imperial College Press, 2006).

[9] G. A. Olah and Á. Molnár, *Hydrocarbon Chemistry*, 2nd ed. (Wiley-Interscience, 2003).

[10] D. R. Lide, *Handbook of Chemistry and Physics*, 87th ed. (CRC-Press, 2006–2007).

[11] http://www.naturalgas.org.

[12] V. S. Arutyunov, V. I. Savchenko, V. M. Rudakov, V. N. Blinichev, and A. M. Kutepov, *Theor. Found. Chem. Eng.* **36**(4), 382 (2002).

[13] G. A. Olah, *Angew. Chem.* **44**(18), 2636 (2005).

[14] T. A. Semelsberger, R. L. Borup, and H. L. Greene, *J. Power Sources* **156**(2), 497 (Jun. 2006).

[15] J. Rass-Hansen, H. Falsig, B. Jørgensen, and C. H. Christensen, *J. Chem. Technol. Biotechnol.* **82**(4), 329 (2007).

[16] M. O. Adebajo, *Green Chem.* **9**(6), 526 (2007).

[17] C.-J. Liu, T. Hammer, and R. Mallinson, *Catal. Today* **98**(4), vii (2004).

[18] N. D. Parkyns, C. I. Warburton, and J. D. Wilson, *Catal. Today* **18**(4), 385 (1993).

[19] T. S. Askgaard, J. K. Nørskov, C. V. Ovesen, and P. Stoltze, *J. Catal.* **156**(2), 229 (1995).

[20] T. J. Hall, J. S. J. Hargreaves, G. J. Hutchings, R. W. Joyner, and S. H. Taylor, *Fuel Process. Technol.* **42**(2), 151 (1995).

[21] D. A. Dowden and T. W. Geoffrey, *Oxygenated Hydrocarbons Production*, British patent GB1244001, IMPERIAL CHEMICAL INDUSTRIES LIMITED (1971).

[22] S. Chempath and A. T. Bell, *J. Catal.* **247**(1), 119 (2007).

[23] M. A. Volpe, *Appl. Catal. A-Gen.* **210**(1–2), 355 (2001).

[24] S. Hannemann, J.-D. Grunwaldt, P. Lienemann, D. Gunther, F. Krumeich, S. E. Pratsinis, and A. Baiker, *Appl. Catal. A-Gen.* **316**(2), 226 (2007).

[25] J. Wei and E. Iglesia, *J. Phys. Chem. B* **108**(13), 4094 (2004).

[26] M. P. Andersson, F. Abild-Pedersen, I. N. Remediakis, T. Bligaard, G. Jones, J. Engbæk, O. Lytken, S. Horch, J. H. Nielsen, J. Sehested, *et al.*, *J. Catal.* **255**(1), 6 (Apr. 2008).

[27] B. E. Solsona, T. Garcia, C. Jones, S. H. Taylor, A. F. Carley, and G. J. Hutchings, *Appl. Catal. A-Gen.* **312**, 67 (2006).

[28] F. Abild-Pedersen, *Methane Activation on Ni Model Surfaces Based on Density Functional Theory*, Ph.D. thesis, Center for Atomic-scale Materials Physics (CAMP), Department of Physics, Technical University of Denmark (2005).

[29] B. Hvolbæk, T. V. W. Janssens, B. S. Clausen, H. Falsig, C. H. Christensen, and J. K. Nørskov, *Nano Today* **2**(4), 14 (2007).

[30] A. F. Hollemann, E. Wieberg, and N. Wieberg, *Lehrbuch der anorganischen Chemie*, 101st ed. (de Gruyter, 1995).

[31] P. Pyykkö, *Chem. Rev.* **88**(3), 563 (May 1988).

[32] P. Schwerdtfeger, *J. Am. Chem. Soc.* **111**(18), 7261 (Aug. 1989).

[33] P. Schwerdtfeger, P. D. W. Boyd, S. Brienne, and A. K. Burrell, *Inorg. Chem.* **31**(16), 3411 (Aug. 1992).

[34] P. Schwerdtfeger, *Heteroatom Chem.* **13**(6), 578 (2002).

[35] http://www.iupac.org/.

[36] C. Kittel, *Introduction to Solid State Physics*, 8th ed. (Wiley-VCH, 2005).

[37] M. Haruta, T. Kobayashi, H. Sano, and N. Yamada, *Chem. Lett.* (2), 405 (1987).

[38] A. S. K. Hashmi and G. J. Hutchings, *Angew. Chem.* **45**(47), 7896 (2006).

[39] G. C. Bond and D. T. Thompson, *Catal. Rev.–Sci. Eng.* **41**(3–4), 319 (1999).

[40] D. E. Starr, S. K. Shaikhutdinov, and H.-J. Freund, *Top. Catal.* **36**(1–4), 33 (2005).

[41] H.-J. Freund, *Catal. Today* **117**(1–3), 6 (2006).

[42] M. Valden, X. Lai, and D. W. Goodman, *Science* **281**(5383), 1647 (1998).

[43] M. S. Chen and D. W. Goodman, *Science* **306**(5694), 252 (2004).

[44] T. V. W. Janssens, A. Carlsson, A. Puig-Molina, and B. S. Clausen, *J. Catal.* **240**(2), 108 (2006).

[45] C. Xu, J. Su, X. Xu, P. Liu, H. Zhao, F. Tian, and Y. Ding, *J. Am. Chem. Soc.* **129**(1), 42 (2007).

[46] C. Xu, X. Xu, J. Su, and Y. Ding, *J. Catal.* **252**(2), 243 (2007).

[47] R. J. H. Grisel and B. E. Nieuwenhuys, *Catal. Today* **64**(1–2), 69 (Jan. 2001).

[48] M. Mavrikakis, P. Stoltze, and J. K. Nørskov, *Catal. Lett.* **64**(2), 101 (2000).

[49] Z.-P. Liu, P. Hu, and A. Alavi, *J. Am. Chem. Soc.* **124**(49), 14770 (2002).

[50] N. Lopez and J. K. Nørskov, *J. Am. Chem. Soc.* **124**(38), 11262 (2002).

[51] N. Lopez, T. V. W. Janssens, B. S. Clausen, Y. Xu, M. Mavrikakis, T. Bligaard, and J. K. Nørskov, *J. Catal.* **223**(1), 232 (2004).

[52] T. V. W. Janssens, B. S. Clausen, B. Hvolbæk, H. Falsig, C. H. Christensen, T. Bligaard, and J. K. Nørskov, *Top. Catal.* **44**(1–2), 15 (2007).

[53] H. Falsig, B. Hvolbæk, I. S. Kristensen, T. Jiang, T. Bligaard, C. H. Christensen, and J. K. Nørskov, *Angew. Chemie* **47**, 4835 (2008).

[54] D. T. Thompson, *Top. Catal.* **38**(4), 231 (2006).

[55] R. D. Waters, J. J. Weimer, and J. E. Smith, *Catal. Lett.* **30**(1–4), 181 (1994).

[56] S. Ivanova, C. Petit, and V. Pitchon, *Appl. Catal. A-Gen.* **267**(1–2), 191 (2004).

[57] S. Ivanova, C. Petit, and V. Pitchon, *Gold Bull.* **39**(1), 3 (2006).

[58] C. H. Christensen, B. Jorgensen, J. Rass-Hansen, K. Egeblad, R. Madsen, S. K. Klitgaard, S. M. Hansen, M. R. Hansen, H. C. Andersen, and A. Riisager, *Angew. Chem.* **45**(28), 4648 (2006).

[59] M.-C. Daniel and D. Astruc, *Chem. Rev.* **104**(1), 293 (2004).

[60] M. Haruta, *Catal. Today* **36**(1), 153 (1997).

[61] J. A. van Bokhoven, C. Louis, J. T. Miller, M. Tromp, O. V. Safonova, and P. Glatzel, *Angew. Chem.-Ger. Ed.* **118**(28), 4767 (2006).

[62] M. Haruta, *Gold Bull.* **37**(1–2), 27 (2004).

[63] M. Haruta and M. Date, *Appl. Catal. A-Gen.* **222**(1–2), 427 (2001).

[64] G. C. Bond and D. T. Thompson, *Gold Bull.* **33**(2), 41 (2000).

[65] L. M. Molina and B. Hammer, *Appl. Catal. A-Gen.* **291**(1–2), 21 (Sep. 2005).

[66] Y. Chen, P. Crawford, and P. Hu, *Catal. Lett.* **119**(1–2), 21 (2007).

[67] P. Buffat and J. P. Borel, *Phys. Rev. A* **13**(6), 2287 (1976).

[68] H. Sykes, E. Charles, F. J. Williams, M. S. Tikhov, and R. M. Lambert, *J. Phys. Chem. B* **106**(21), 5390 (2002).

[69] P. M. Ajayan and D. L. Marks, *Phys. Rev. Lett.* **60**(7), 585 (1988).

[70] http://www.mintek.co.za.

[71] http://www.gold.org.

[72] W. Ehrfeld, V. Hessel, and H. Löwe, *Microreactors*, 1st ed. (WILEY-VCH, 2000).

[73] K. Jensen, *Chem. Eng. Sci.* **56**(2), 293 (2001).

[74] G. Kolb and V. Hessel, *Chem. Eng. J.* **98**(1–2), 1 (2004).

[75] L. Kiwi-Minsker and A. Renken, *Catal. Today* **110**(1–2), 2 (Dec. 2005).

[76] S. Jensen, J. L. Olsen, S. Thorsteinsson, O. Hansen, and U. J. Quaade, *Catal. Commun.* **8**, 1985 (2007).

[77] P. L. Mills, D. J. Quiram, and J. F. Ryley, *Chem. Eng. Sci.* **62**(24), 6992 (Dec. 2007).

[78] N. Dongari, A. Agrawal, and A. Agrawal, *Int. J. Heat Mass Transf.* **50**(17–18), 3411 (Aug. 2007).

[79] http://www.danchip.dtu.dk.

[80] http://www.mic.dtu.dk.

[81] J. Liu, *Microsc. microanal.* **10**(1), 55 (2004).

[82] http://www.gfe.rwth aachen.de/downloads/Praktikum_IEHK.pdf.

[83] D. B. Williams and C. B. Carter, *Transmission Electron Microscopy — I. Basics* (Kluwer Academics / Plenum Press, 1996).

[84] D. B. Williams and C. B. Carter, *Transmission Electron Microscopy — III. Imaging* (Kluwer Academics / Plenum Press, 1996).

[85] http://www.microscopy.ethz.ch.

[86] D. C. Joy, A. D. Romig, and J. Goldstein, *Principles of Analytical Electron Microscopy* (Springer, 1986).

[87] http://www.amptek.com.

[88] PANalytical, *MiniPal 4 User's Guide*, PANalytical B.V. (2008) http://www.PANalytical.com.

[89] A. C. Gluhoi, M. A. P. Dekkers, and B. E. Nieuwenhuys, *J. Catal.* **219**(1), 197 (2003).

[90] L. M. Molina and B. Hammer, *Phys. Rev. B* **69**(15), 155424 (2004).

[91] http://wiki.fysik.dtu.dk/dacapo.

[92] D. Vanderbilt, *Phys. Rev. B* **41**(11), 7892 (Apr. 1990).

[93] B. Hammer, L. B. Hansen, and J. K. Nørskov, *Phys. Rev. B* **59**(11), 7413 (1999).

[94] J. K. Nørskov, J. Rossmeisl, A. Logadottir, L. Lindqvist, J. R. Kitchin, T. Bligaard, and H. Jonsson, *J. Phys. Chem. B* **108**(46), 17886 (2004).

[95] S. Kurth, J. P. Perdew, and P. Blaha, *Int. J. Quantum Chem.* **75**, 889 (1999).

[96] J. H. Noggle, *Physical Chemistry*, 3rd ed. (Harper Collins, 1996).

[97] B. E. Nieuwenhuys, A. C. Gluhoi, E. D. L. Rienks, C. J. Weststrate, and C. P. Vinod, *Catal. Today* **100**(1–2), 49 (2005).

[98] Z.-P. Liu, X.-Q. Gong, J. Kohanoff, C. Sanchez, and P. Hu, *Phys. Rev. Lett.* **91**(26), 2661021 (2003).

[99] J. K. Nørskov, T. Bligaard, A. Logadottir, S. Bahn, L. B. Hansen, M. Bollinger, H. Bengaard, B. Hammer, Z. Sljivancanin, M. Mavrikakis, *et al.*, *J. Catal.* **209**(2), 275 (2002).

[100] P. Landon, J. Ferguson, B. E. Solsona, T. Garcia, S. Al-Sayari, A. F. Carley, A. A. Herzing, C. J. Kiely, M. Makkee, J. A. Moulijn, *et al.*, *J. Mater. Chem.* **16**(2), 199 (2006).

[101] F. Abild-Pedersen, O. Lytken, J. Engbæk, G. Nielsen, I. Chorkendorff, and J. K. Nørskov, *Surf. Sci.* **590**(2–3), 127 (2005).

[102] H. J. Monkhorst and J. D. Pack, *Phys. Rev. B* **13**(12), 5188 (1976).

[103] F. Lärmer and A. Schilp, *Anisotropic etching of silicon substrates*, German patent DE4241045-C1, Robert Bosch GmbH (1994).

[104] F. Lärmer and A. Schilp, *Method of anisotropically etching silicon*, US patent US5501893, Robert Bosch GmbH (1996).

[105] S. Jensen, *Inductively Coupled Plasma Etching for Microsystems*, Ph.D. thesis, Department of Micro- and Nanotechnology (MIC), Technical University of Denmark (2004).

[106] A. M. Hynes, H. Ashraf, J. K. Bhardwaj, J. Hopkins, I. Johnston, and J. N. Shepherd, *Sens. Actuator A-Phys.* **74**(1–3), 13 (1999).

[107] H.-C. Liu, Y.-H. Lin, and W. Hsu, *Microsyst. Technol.* **10**(1), 29 (2003).

List of included Papers

PAPER 1

Oxidation of Methane on nanoparticulate Au/TiO_2 at low temperature: a combined microreactor and DFT study

G. Walther, G. Jones, S. Jensen, U. J. Quaade, S. Horch
Catalysis Today (accepted)

PAPER 2

Low Temperature Methane Oxidation on differently supported 2 nm Au Nanoparticles

G. Walther, L. Cervera-Gontard, U. J. Quaade, S. Horch
submitted to Gold Bulletin

PAPER 3

Oxidation of CO and H_2 by O_2 and N_2O on Au/TiO_2 Catalysts in Microreactors

G. Walther, D. J. Mowbray, T. Jiang, G. Jones, S. Jensen, U. J. Quaade, S. Horch
Journal of Catalysis (accepted)

Paper 1

Oxidation of Methane on nanoparticulate Au/TiO_2 at low temperature: a combined microreactor and DFT study

Oxidation of Methane on nanoparticulate Au/TiO_2 at low temperature: a combined microreactor and DFT study

G. Walther[1], G. Jones[1], S. Jensen[2], U. Quaade[3], S. Horch[1, *]

[1] Center for Atomic-scale Materials Design (CAMD), Department of Physics

[2] Department of Micro and Nanotechnology (MIC)

[3] Center for Individual Nanoparticle Functionality (CINF), Department of Physics

Technical University of Denmark, DK-2800 Kgs. Lyngby, Denmark

[*] Corresponding author: horch@fysik.dtu.dk

Herein we present results from experimental and theoretical studies concerning low temperature oxidation of CH_4 over TiO_2 supported Au nanoparticles. Our findings suggest that partial oxidation can not be achieved under these conditions (1 bar, 30°C – 250°C). In order to understand this further, results from CO and H_2 oxidation studies are also presented. The reaction rate for CH_4 oxidation is found to be far lower than the rate for both CO and H_2 oxidation, this goes towards explaining the strong tendency for total CH_4 oxidation. These findings are further corroborated by DFT-calculations investigating the thermodynamics of CH_4 oxidation on a stepped Au(211) surface.

Keywords: Gold; Titanium dioxide; Catalysis; Microreactor; Methane; Oxidation; Particle size

Introduction

There is continued interest to find catalysts which can transform CH_4 into an easily transportable liquid via low-temperature partial oxidation of CH_4. This is mainly due to the fact that large amounts of natural gas are available in areas that are so remote from the energy consumers that there are no pipelines available to transport the gas. Presently, direct liquefaction of CH_4, the main component of natural gas, is the most common process used for shipping in gas tankers. This requires low temperatures and high pressure and is thus not really an economically viable option. Instead, more than 20 billion cubic meters of natural gas are flared annually which has a detrimental effect on the environment [1]. Unfortunately however, no good catalyst is known so far for low-temperature partial CH_4 oxidation. The reason is that methanol dissociates catalytically at lower temperatures than partial methane oxidation occurs. The search is on therefore, to find a catalyst that provides the required selectivity.

The quest for partial oxidation catalysts is also important for the increasing market in CH_4, which represents one of the basic organic chemicals [2]. In this connection, much work is being carried out in order to develop new catalysts that can convert CH_4 into higher-value chemicals [3, 4]. Baiker *et al*. have studied a number of noble metals catalysts to determine their potential for the partial oxidation of CH_4 to CO and H_2. They have recently reported identification of extinction and ignition temperature rates and selectivity between 300°C and 500°C [5]. In an earlier study, Iglesia *et al*. studied the reaction of different gas mixtures containing CH_4, CO_2 and labeled CO over supported platinum clusters [6]. Since identical ^{13}C fractions in CO and CO_2 were determined, Iglesia *et al*. concluded that CO_2 activation is quasi-equilibrated and kinetically irrelevant. Recent studies suggest that there is a condition dependent mechanism for the reforming reaction of CH_4 with CO for-

mation being dominant at lower temperatures and CH_4 activation taking over at higher temperature [7]. However it must be kept in mind that these experiments and calculations are looking at the CH_4 reforming reaction, which is run at temperatures in the range of 600°C – 800°C.

Within the last decade, a new candidate for such a catalyst, nanoparticulate gold, has emerged. Even though gold is often referred to as the noblest of all the metals (it is e.g. inert in an oxygen atmosphere [8]), nanoparticulate gold shows a surprisingly high catalytic activity for CO oxidation in both experimental [9–20] and theoretical studies [19, 21–27]. Beside CO oxidation, many other reactions have been studied on gold catalysts, including the oxidation of hydrocarbons [18, 19, 28–31] and oxygen-containing hydrocarbons [11, 18, 19, 32, 33] as well as the catalysis of hydrogenation of unsaturated substrates [11, 19, 34].

The reason for this surprising activity is still under debate: After the pioneering work of Haruta [9], the activity of gold has been linked to several different effects, e.g. a quantum-size effect [10], support-induced strain [22], charge transfer from the small gold particles to adsorbed oxygen [35] and the role of low-coordinated gold atoms [22, 24–27]. It is clear from these alternative perspectives that more work is required to find the definitive answer to this debate. However it is entirely probable that any of the perspectives are correct under a given set of reaction conditions, and that the apparent results are sometimes the results of experimental or theoretical conditions and probe being used.

Another issue when using gold as a catalyst is the stability of nanoparticulate gold. Since gold has a low melting point, gold nanoparticles become mobile even at low temperatures [36–38], and are observed to sinter into bigger particles [37]. An effective support which is able to keep the gold

particles well dispersed (and the one we also use in this contribution) is TiO_2. However, more study is needed to figure out how this works, and to understand fully how the particles change during reaction.

In the present contribution, we present a combined experimental and theoretical study of low-temperature CH_4 oxidation on nanoparticulate gold supported on TiO_2. We focus particularly on the possible reasons why partial oxidation cannot be achieved. To this end, we compare the experimental findings with a thermodynamic picture for CH_4 oxidation, obtained from density functional theory (DFT) calculations. Additionally, the influence of the reaction to the gold particles was investigated.

Experimental Section

Experimental Setup

Activity measurements of supported gold nanoparticles were performed in microreactors. The capillaries of these silicon devices were etched using deep reactive ion etching (DRIE). The fabrication process is described elsewhere [39, 40]. Figure (1a) illustrates the 280 µm deep capillary system consisting of two inlets, a sniffer hole and one outlet. It allows mixing of undiluted gases on the chip without any danger of explosion. The dimensions of the reactor chamber are (8.0 × 1.5 × 0.2) mm^3. The whole device measures 20 mm × 16 mm × 0.35 mm and is closed with a Pyrex glass lid using anodic bonding. The inlet and outlet holes as well as the sniffer hole are sealed with Viton O-rings to an aluminum interface block. The reactor chamber can be heated by a piece of silicon that

is clamped to it. Temperature is measured with a K-type thermocouple on the top of the reactor. For temperature-ramped activity measurements, temperature is controlled using a PID-controller (Eurotherm). Gas flow is controlled by mass flow controllers (Bronkhorst), operating in the range from 0.02 to 1.00 ml min^{-1} with a precision of 0.02 ml min^{-1}. Via the sniffer hole, the microreactor is connected to a Baltzers quadrupole mass spectrometer (QMA) to analyze the reaction products. Figures (1b) and (1c) show a zoom-in on the 3 µm sniffer hole.

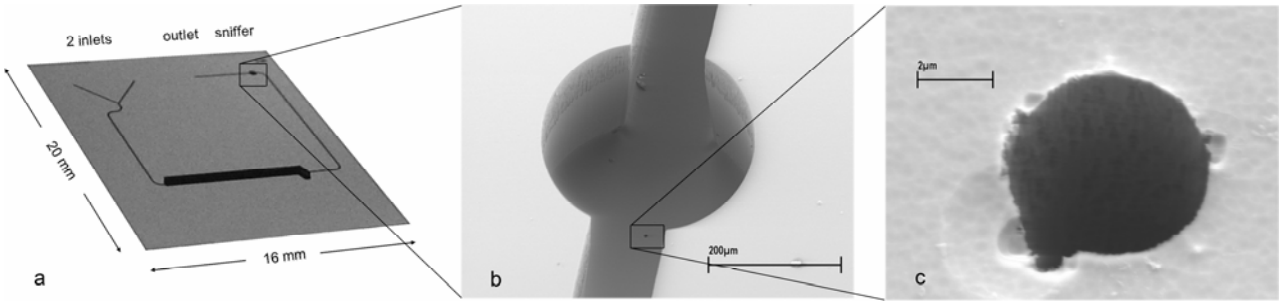

Figure 1: Unloaded silicon microreactor with two inlets to mix gases on the chip, a (8.0 × 1.5 × 0.2) mm^3 sized reactor chamber, a sniffer hole and a single outlet.

To confirm the QMA analysis, an Agilent gas chromatograph (3000A microGC) was used to analyze the reaction products. Since the GC is less sensitive than the QMA, a mini-reactor (quartz glass tube) containing more catalyst material was used in that case to produce larger amounts of the reaction products. The GC has combined columns of 10 m molecular sieve and 3 m PLOT U with 1.0 µl back-flushing, which allows simultaneous analysis of H_2, O_2, N_2, CO, CO_2, H_2O and CH_4 by a thermal conductivity detector (TCD). With argon as the carrier gas, the GC is 15 times more sensitive to H_2 than to CO. To avoid condensing water, formed by the catalytic reactions, the tubing be-

tween the microreactor and the GC is kept at a temperature of 100°C, whereas the capillary of the GC itself is kept at 90°C.

Catalytic Reactions

A 3.3 nm Au/TiO_2 reference catalyst from the World Gold Council was used to study total CH_4 oxidation according to formula (1). We also considered partial CH_4 oxidation (2) and studied therefore the oxidation of CO (3) and H_2 (4) as well, using a fresh catalyst for each reaction.

$CH_4 + 2\,O_2 \rightarrow CO_2 + 2\,H_2O$, $\Delta H^0 = -802.3$ kJ mol^{-1}, (1)

$CH_4 + ½\,O_2 \rightarrow CO + 2\,H_2$, $\Delta H^0 = -185.3$ kJ mol^{-1}, (2)

$CO + ½\,O_2 \rightarrow CO_2$, $\Delta H^0 = -283.0$ kJ mol^{-1}, (3)

$H_2 + ½\,O_2 \rightarrow H_2O$, $\Delta H^0 = -241.8$ kJ mol^{-1}. (4)

Due to the high sensitivity of the GC to hydrogen, the reactants in (4) were diluted with 50% argon. For all reactions discussed, the total flow was kept constant at 1.00 ml min^{-1}.

Self heating of the catalyst during an exothermic reaction is difficult to avoid, but it can be minimized by operating the catalyst in a range up till 10% conversion. The greatest amount of heat liberated during the above reactions was 26.0 mW for CO oxidation, where 40% conversion was already achieved at 80°C.

The catalysts used both in the microreactor as well as in the mini-reactor were deactivated over 18 hours at 100°C. To ensure reproducibility, activity measurements were conducted afterwards with the following scheme for the applied CH_4/O_2 ratio, which was run twice: 2/1, 4/1, 1/2. Reproducibility of the first and the second GC-run was taken as sign for that the catalyst did not change during reactions. For steady-state activity measurements, the temperature was ramped from 50°C to 250°C in steps of 10°C h^{-1} when using the GC and from 75°C to 225°C in steps of 5°C per 5 min when using the QMA.

Particle Analysis

The size distribution and shape of the gold particles were probed using a PHILIPS Tecnai 20T high resolution transmission electron microscope at 200 kV. Specimens of the catalyst were taken before and after the temperature-programmed activity measurements, and prepared on a carbon TEM grid by dropping a suspension of catalyst in ethanol on the grid.

Theoretical Methodology

DFT is used as implemented in the computer code DACAPO using the RPBE exchange correlation functional [41]. Calculations for stepped model gold surfaces were carried out using fcc crystals terminated at the {211} facet. Unit cells of (2×1) periodicity were used with a depth of 10 atomic layers (roughly equivalent to 3-close packed layers) and a vacuum region of 10 Å. An electronic planewave cut-off of 340 eV has been used with the Brillouin zone being sampled by a Monkhorst-

Pack [42] mesh of 4×4×1 k-points. Pseudopotentials of the Vanderbilt [43] type were used to describe the electronic core regions.

Thermodynamic analysis is carried out using the total energies obtained from the DFT calculations. In this paper free energies have been calculated by employing standard formulas for the thermodynamics of a classical ideal gas [44]. For a gas-phase species (X) at temperature (T) and pressure (P), the Gibbs free energy ($G_X^{P,T}$) is given by:

$$G_X^{P,T} = E_X + E_{ZPE} + \Delta H^{0,T} - TS^T + RT\ln(P/P^o),$$

where E_{ZPE} is the zero point energy, $\Delta H^{0,T}$ is the enthalpy change due to raising the temperature from 0 K to T, S^T is the entropy at T, R is the universal gas constant and P^o is standard pressure (taken to be 1 bar).

The potential energy of the adsorbed species (X'), $E_{X'}$, is given by: $E_{Au/X'} - E_{Au}$, where E_{Au} is the energy of the clean Au surface and $E_{Au/X'}$ is the energy of the adsorbate and surface system. In order to calculate the free energy of this species we neglect the pressure term so that the enthalpy change is replaced by the change in internal energy. This leads to the following expression for the free energy ($G_{X'}^{P,T}$):

$$G_{X'}^{P,T} = E_{X'} + E_{ZPE} + \Delta U^{0,T} - TS^T .$$

All vibrational frequencies used to determine E_{ZPE}, $\Delta U^{0,T}$ and S^T are calculated within the harmonic approximation.

It is an unfortunate deficiency on the current implementations of DFT that the exchange correlation functional does not handle self-interaction correctly. This is particularly troublesome for calculations involving the gas phase O_2 molecule and adsorbed CO. In order to overcome these deficiencies of DFT it is possible to apply empirical corrections. This paper has implemented the correction proposed by Abild-Pedersen and Andersson for CO adsorption [45]. In order to correct for the O_2 molecule we make a correction that essentially involves comparing the calculated Gibbs energy of formation for water with that obtained experimentally. Any discrepancy between the two values is attributed to the O_2 molecule, details of the correction implemented herein can be found in appendix 1.

Results

The average gold particle size before activity measurements was determined to be (3.4 ± 0.8) nm based on a TEM analysis of 60 particles. This equals the value stated by the supplier, indicating that the particles had not sintered during storage.

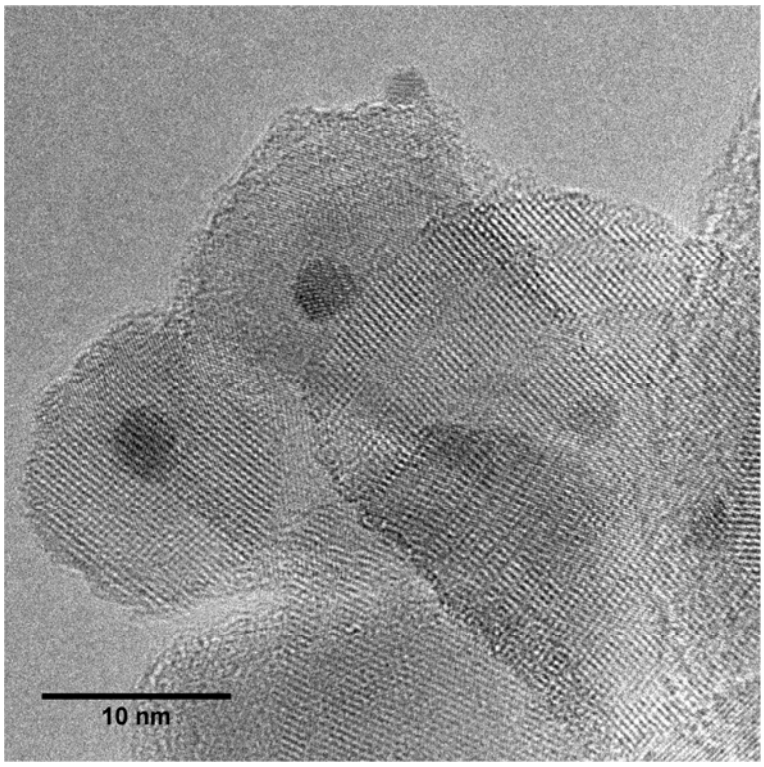

Figure 2: **High resolution TEM image of the catalyst as supplied.**

Methane Oxidation

The apparent activation energy for CH_4 oxidation on these particles was determined to be approximately (60 ± 2) kJ mol^{-1} from the Arrhenius plots in Figure 3. The difference in reaction rate when measured with the QMA or the GC may be related to a morphological change of the catalyst in the GC-runs, since the time the catalyst was exposed to the reactants was 24h for each GC measurement as compared to only 3h in case of the QMA. This accounts also for the higher conversion, plotted in Figure 4, when the measurement was conducted using a QMA. Since neither CO nor H_2 were detected, the yield of CO_2 is directly given by the consumption of CH_4. The onset of CH_4 oxidation was found at 130°C.

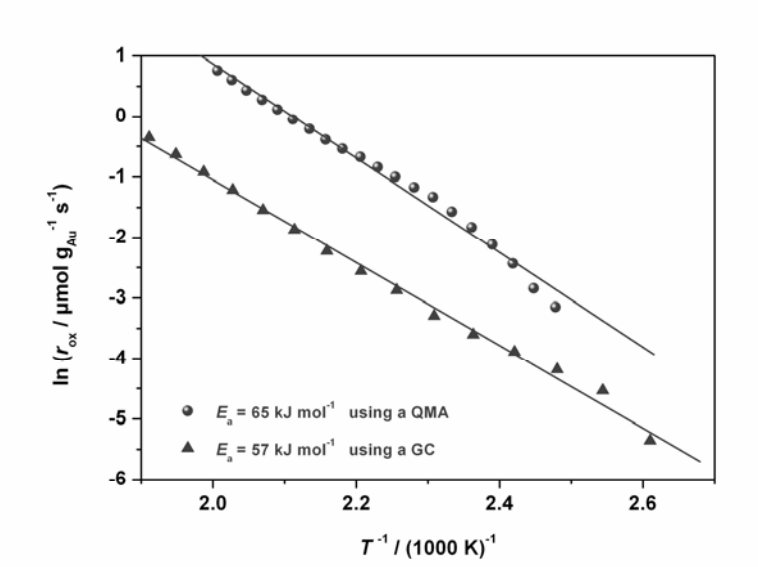

Figure 3: Arrhenius plots of the CH_4 oxidation rates. The uncertainty of E_a is ~ 2 kJ mol^{-1} and 1 kJ mol^{-1} when using the QMA and the GC setup, respectively.

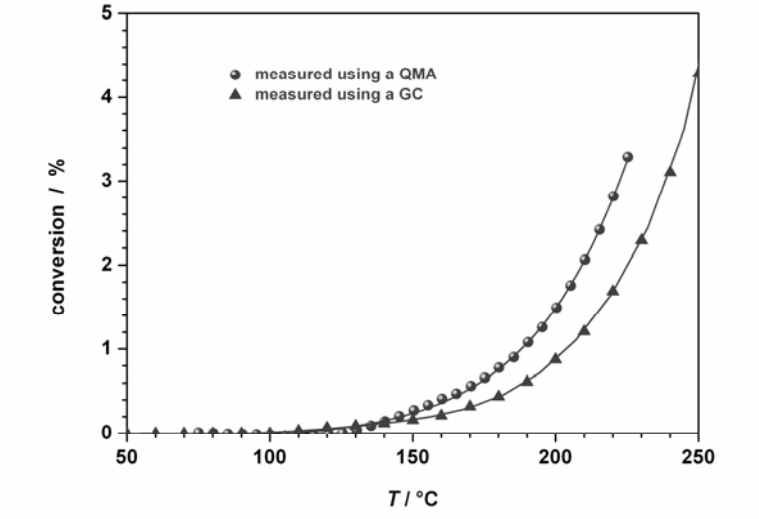

Figure 4: CH_4 conversion shows an onset at 130°C.

TEM-analysis after the entire sequence of steady-state CH_4-oxidation measurements in the GC shows that the particles now have a broad range of sizes (2–7 nm). By tilting the specimen from -65° to +65°, the three dimensional structure of the particles can be reconstructed. We did this for

one particle: Figure 5 shows a TEM image of a 4.8 nm gold particle with its 3D reconstruction (see inset). This particle is found to stick to the support with its (111) surface, as indicated by the arrow.

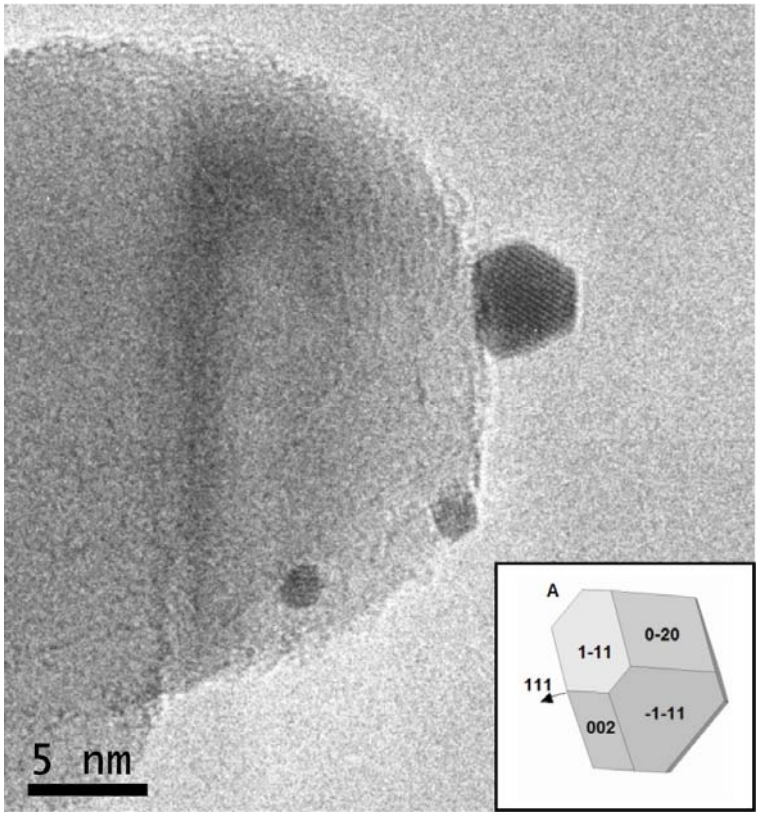

Figure 5: High resolution TEM image of a 4.8 nm gold particle after steady-state activity measurements.

CO and H_2 Oxidation

The parallel running fits for CO and H_2 oxidation in the Arrhenius plot (Figure 6) indicate similar activation energies for both reactions. From the Arrhenius equation, the activation energy could be determined to be (38 ± 0.8) kJ mol^{-1} for CO oxidation. The reaction rate for H_2 oxidation is about 6 times lower than that for CO oxidation. This goes along with the higher conversion of CO than H_2 as function of temperature, represented in Figure 7. For CO oxidation, saturation was already found

at 80°C. For both reactions, a mass balance of the reactants consumed and the products formed was used to verify the results.

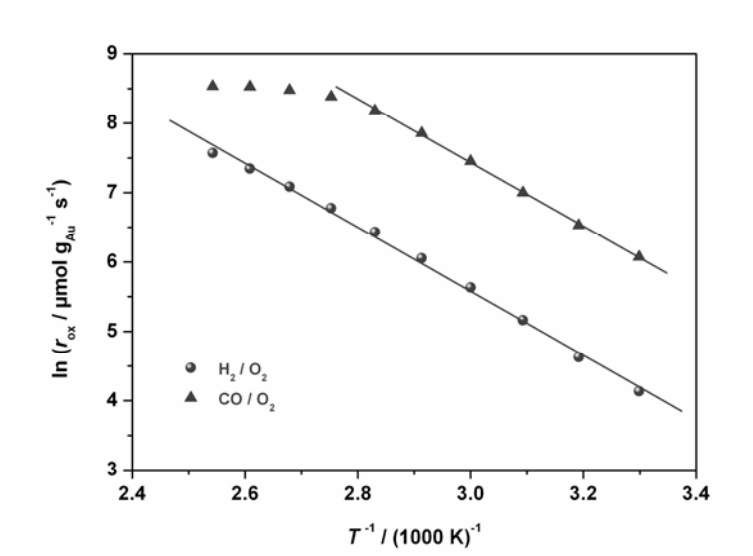

Figure 6: Arrhenius plots of the CO and H_2 oxidation rates determined using the GC.

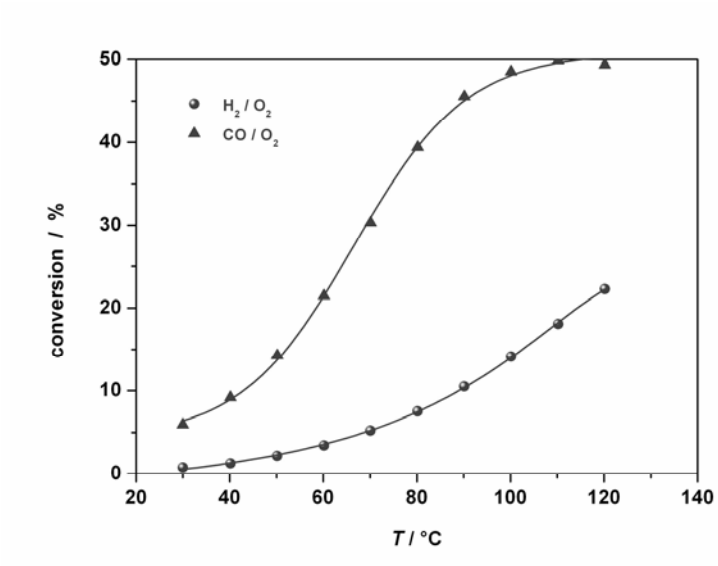

Figure 7: Conversion of CO and H_2.

The particle size of the freshly prepared gold after these sequences of steady-state CO- or H_2-oxidation measurements in the GC was determined to be (5.7 ± 3.4) nm by TEM analysis of 57 particles.

Theoretical Results

Figure 8 illustrates the standard free energy diagram for the stable species present in the oxidation of CH_4 at 450 K. This is constructed using the DFT total energies in combination with the thermodynamic corrections as outlined in the methodology. Three possible pathways are depicted, partial oxidation terminating at CO(g) and H_2(g), also CO_2(g) and H_2(g) and finally complete combustion to CO_2(g) and H_2O(g). The diagram shows a route which goes via a methoxy intermediate followed by carbonyl species on the surface prior to the formation of CO(g) (CO_2(g)). It was found that if one went via a route of direct dehydrogenation of CH_4 then the thermodynamic barriers were extremely high (in excess of 4 eV for the formation of C* + 2 H_2(g) from CH_4). It can be seen that this route still contains the difficult initial dehydrogenation of CH_4, which is 1.4 eV uphill. However once this step is overcome the pathway is downhill all the way to the products. Here we see that complete combustion is by far the most thermodynamically favored reaction and consequently (subject to kinetic barriers) one would expect the reaction to proceed to this point. Indeed this is found to be the case experimentally where partial oxidation is not observed, we will revisit this point in the discussion.

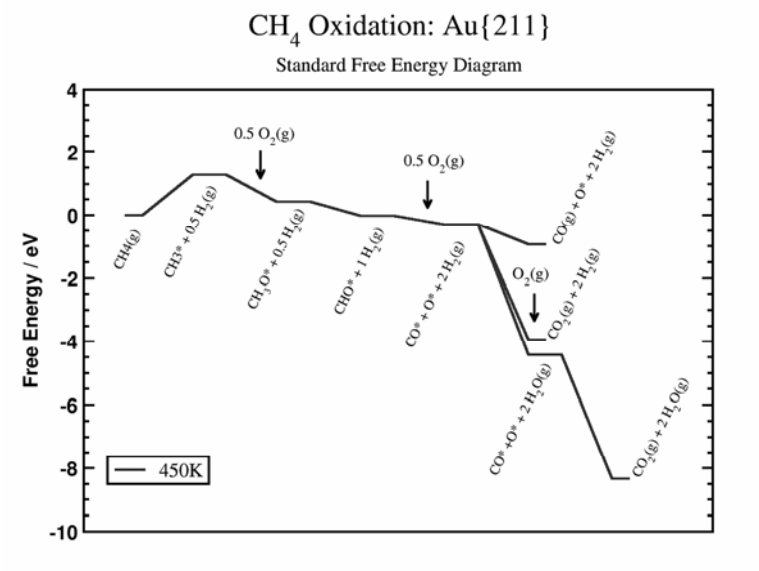

Figure 8: Standard free energy reaction profile for the stable intermediates present in the oxidation of CH_4, as determined from DFT.

Discussion

We shall start by considering the species present, as detected during the experimental run. In the case of partial oxidation, we can assume (due to the stoichiometry of the reaction) that if we were to form CO during CH_4 oxidation, then H_2 would also be formed (2). In fact, we did not observe any H_2 evolution, our first indication of the lack of partial oxidation. Furthermore we did observe water formation during the CH_4 oxidation, in proportions that match the stoichiometry expected from equation (1). From this we can conclude that we have carried out complete combustion to form CO_2.

The results of additional studies on the oxidation of H_2 and CO, their activation barriers, rates and conversions are shown in Table 1. These suggest that even if CO was formed from partial oxidation,

CO and H_2 could easily be post oxidized to CO_2 and H_2O. This is due to the fact that when compared to CH_4 oxidation, the higher reaction rate for CO and H_2 oxidation (which is coupled to their lower apparent activation energies (38 ± 0.6) kJ mol^{-1}), indicates that under these reaction conditions these steps would be equilibrated.

Table 1: Comparison of activation energies, reaction rates and conversion

reaction	E_a / kJ mol^{-1}	ln(r_{ox} / µmol g_{Au}^{-1} s^{-1})	conversion / %
CH_4 / O_2	61 ± 4	0.7 (at 220°C)	2.9 (at 220°C)
CO / O_2	38 ± 0.6	8.3 (at 80°C)	45 (at 80°C)
H_2 / O_2	38 ± 0.8	6.4 (at 80°C)	7 (at 80°C)

We have carried out the theoretical calculations on a {211} surface, and shall first address some of the issues surrounding this as a model system. This particular surface facet has been chosen because recent experimental and theoretical work has demonstrated the importance of the B5 site in catalytic activity for N_2 dissociation and CH_4 activation on Ni [46]. If one looks at the {211} surface, it can be seen that the step sites are made up of the B5 sites. Therefore we expect this surface to be a good model of the edges and steps present on a nanoparticle. Some care does however need to be taken because corner sites may also be implicated in the activity of a catalyst, this in fact is the subject of on going research. However, in our case we anticipate the model to be reasonable in the explanation of reactivity.

If we look at the thermodynamic picture presented from theory we are able to gain insight into whether a particular reaction is feasible. In fact what we see from figure 8 is that both partial CH_4 oxidation and complete CH_4 combustion are exothermic at 450 K, meaning both processes are

likely to proceed. However, CO_2(g) formation is favored far more greatly and in the absence of kinetic considerations would dominate the oxidation process. Experimentally we never observe evidence for the formation of CO(g) or H_2(g) above that of the background noise which concurs well with this simple analysis.

In order to go beyond just the thermodynamic picture, one needs to consider the barriers present in the reaction pathway. Recent work by Nørskov *et al*. has studied the oxidation of CO on a model nanoparticle [27]. Their work demonstrated that there are two possible routes by which complete oxidation can proceed. The first is by reaction with adsorbed atomic oxygen O* (* denotes an adsorbed species). The second is through an intermediate that involves molecular oxygen, this is generally perceived to proceed via a physisorbed precursor. This particular mechanism has also been highlighted by Alavi *et al.* [23]. Both of these works showed good agreement on the relative barrier heights to CO oxidation, with the barrier via the first route being approximately 63 kJ mol^{-1} and that of the second route being 39 kJ mol^{-1}. This is in good agreement with our apparent activation barrier of CO oxidation measured.

Conclusions

In the present paper, we have investigated CH_4 oxidation on TiO_2 supported gold nanoparticles under mild conditions (1 bar, 30°C – 250°C). Our experiments show that only total oxidation of CH_4 occurs. Additional studies of CO and H_2 oxidation strongly suggest that these species can easily be post-oxidized, even if partial CH_4 oxidation has occurred early in the reaction. From DFT calculations, the thermodynamics show that there is a strong tendency for the formation of CO_2, which

means the only way to achieve partial oxidation, is to exploit the variations in barrier heights i.e. we are attempting to form the kinetic product — not a thermodynamic product. On a stepped Au(211) surface, CH_4 dissociation is shown to be thermodynamically unfavorable and the influence of barriers and kinetics on this process are the subject of ongoing work.

Acknowledgements

G. Walther gratefully acknowledges financial support from NABIIT. We thank Lionel Cervera Gontard (Center for Electron Nanoscopy, CEN.DTU) for experimental assistance with taking and analyzing TEM images. The Center for Atomic-scale Materials Design is funded by the Lundbeck Foundation. The authors wish to acknowledge additional support from the Danish Center for Scientific Computing through grant HDW-1103-06.

Appendix

Correction to $O_2(g)$

This basis of this correction lies in taking an experimentally determined value for the formation of water which is obtainable from standard thermodynamic tables. This is then compared to the value obtained using DFT in combination with thermodynamic calculations, the difference between these two values is used to establish the correction required for the O_2 molecule(δ_{O_2}):

$$\delta_{O_2} = 2(\Delta_f G^{o,298}_{Tables} - \Delta_f G^{o,298}_{calc.}).$$

The factor of 2 arises due to the definition of the heat of formation of water being for the formation of one mole of water, from one mole of H_2 gas and half a mole of oxygen gas. We can thus define the standard Gibbs free energy of Reaction as:

$$\Delta_f G^{o,298} = \Delta G^{o,298}_{H_2O} - \Delta G^{o,298}_{H_2} - \tfrac{1}{2}\Delta G^{o,298}_{O_2}.$$

The expression for the Gibbs free energy of the individual species can be found in the theoretical methodology.

Table 2 lists the key values that are required to find the correction, determined both from DFT calculations and by application of the thermodynamics of a classical ideal gas. In parenthesis the values determined from thermodynamic tables are listed, as can be seen there is very little to separate these values from those obtained by theory. The CRC handbook lists the Gibb's free energy of for-

mation at 298 K of water, $\Delta_f G^{o,298}(H_2O)$, as being -228.582 kJ mol^{-1} (-2.37 eV). The potential energy of formation, $\Delta_f E_{DFT}(H_2O)$, is found to be -2.35 eV, which combined with the thermodynamic values leads to a correction of 0.74eV.

Table 2: Thermodynamic Properties calculated from both the partition function and from tabulated values in parenthesis . Enegies /eV.

Species	E_{ZPE}	$\Delta H^{0\text{-}298}$	TS^{298}	$\Delta_f G^{o,298}$
H_2O	0.58(0.56)	0.10(0.10)	0.58(0.58)	-469.63(-469.65)
H_2	0.27(0.27)	0.09(0.09)	0.40(0.40)	-32.07(-32.07)
O_2	0.10(0.10)	0.09(0.09)	0.60(0.63)	-871.13(-871.16)
H_2O - H_2 - ½O_2	0.26(0.24)	-0.03(-0.03)	0.12(0.14)	-2.00(-2.00)

References

[1] V.S. Arutyunov, V.M. Rudakov, V.I. Savchenko, E.V. Sheverdenkin, O.G. Sheverdenkin and A.Yu. Zheltyakov, Theo. Found. Chem. Eng., 36 (2002) 472.

[2] N.D. Parkyns, C.I. Warburton and J.D. Wislon, Catal. Today, 18 (1993) 385.

[3] C.-J. Liu, T. Hammer and R. Mallinson, Catal. Today, 98 (2004) VII.

[4] M.O. Adebajo, Green Chem., 9 (2007) 526.

[5] S. Hannemann, J.-D. Grunwaldt, P. Lienemann, D. Günther, F. Krumeich, S.E. Pratsinis and A. Baiker, Appl. Catal. A, 316 (2007) 226.

[6] J. Wei, E. Iglesia, J. Phys. Chem. B, 108 (2004) 4094.

[7] M.P. Andersson, F. Abild-Pedersen, I.N. Remediakis, T. Bligaard, G. Jones, J. Engbæk, O. Lytken, S. Horch, J.H. Nielsen, J. Sehested, J.R. Rostrup-Nielsen, J.K. Nørskov and I. Chorkendorff, J. Catal., 255 (2008) 6.

[8] J. Kim, E. Samano and B. Koel, Surf. Sci., 600 (2006) 4622.

[9] M. Haruta, Catal. Today, 36 (1997) 153.

[10] M. Valden, X. Lai and D.W. Goodman, Science, 281 (1998) 1647.

[11] G.C. Bond, Catal. Rev. – Sci. Eng., 41 (1999) 319.

[12] M. Haruta, Cat. Tech., 6 (2002) 102.

[13] A.C. Gluhoi, M.A.P. Dekkers, B.E. Nieuwenhuys, J. Catal., 219 (2003) 197.

[14] B. Schuhmacher, V. Plzak, M. Kinne and R.J. Behm, Catal. Lett., 89 (2003) 109.

[15] M. Chen and D.W. Goodman, Science, 306 (2004) 252.

[16] T.V.W. Janssens, A. Carlsson, A. Puig-Molina and B.S. Clausen, J. Catal., 240 (2006) 108.

[17] H.-J. Freund, Catal. Today, 117 (2006) 6.

[19] G.C. Bond, C. Louis and D.T. Thompson, Catalysis by Gold, Imperial College Press, 1. Edition, London, 2006.

[18] D.T. Thompson, Topic. Catal., 38 (2006) 231.

[20] C. Xu, J. Su, X. Xu, P. Liu, H. Zhao, F. Tian, Y. Ding, J. Am. Chem. Soc., 129 (2007) 42.

[21] B. Hammer, J.K. Nørskov, Surf. Sci., 343 (1995) 211.

[22] M. Mavrikakis, P. Stotze, J.K. Nørskov, Catal. Lett., 64 (2000) 101.

[23] Z. Liu, P. Hu and a. Alavi, J. Am. Chem. Soc., 124 (2002) 14770.

[24] N. Lopez and J.K. Nørskov, J. Am. Chem. Soc., 124 (2002) 11262.

[25] N. Lopez, T.V.W. Janssens, B.S. Clausen, Y. Xu, M. Mavrikakis, T. Bligaard and J.K. Nørskov, J. Catal., 223 (2004) 232.

[26] T.V.W. Janssens, B.S. Clausen, B. Hvolbæk, H. Falsig, C.H. Christensen, T. Bligaard, and J.K. Nørskov, Topic. Catal., 44 (2007) 15.

[27] B. Hvolbæk, T.V.W. Janssens, B.S. Clausen, H. Falsig, C.H. Christensen, and J.K. Nørskov, NanoToday, 2 (2007) 14.

[28] R.D. Waters, J.J. Weimer and J.E. Smith, Catal. Lett., 30 (1994) 181.

[29] S. Ivanova, C. Petit, V. Pitchon, Catal. Today, 113 (2006) 182.

[30] S. Ivanova, C. Petit, V. Pitchon, Gold Bulletin, 39 (2006) 3.

[31] B.E. Solsona, T. Garcia, C. Jones, S.H. Taylor, A.F. Carley and, G.J. Hutchings, Appl. Catal. A, 312 (2006) 67.

[32] A.S.K. Hashmi and G.J. Hutchings, Angew. Chem. Int. Ed., 45 (2006) 7896.

[33] C.H. Christensen, B. Jørgensen, J. Rass-Hansen, K. Egeblad, R. Madsen, S.K. Klitgaard, S.M. Hansen, M.R. Hansen, H.C. Andersen and A. Riisager, Angew. Chem. Int. Ed., 45 (2006) 4648.

[34] M.-C. Daniel and D. Astruc, Chem. Rev., 104 (2004) 293.

[35] J.A. v. Bokhoven, C. Louis, J.T. Miller, M. Trommp, O.V. Safonova and P. Glatzel, Angew. Chem., 118 (2006) 4767.

[36] P. Buffat and J.P. Borel, Phys. Rev. A, 13 (1976) 2287.

[37] E. Charls, H. Sykes, F.J. Williams, M.S. Tikhov and R.M. Lambert, J. Phys. Chem. B, 106 (2002) 5390.

[38] P.M. Ajayan and D.L. Marks, Phys. Rev. Lett., 60 (1988) 585.

[39] U.J. Quaade, S. Jensen and O. Hansen, Rev. Sci. Instrum., 75 (2004) 3345.

[40] U.J. Quaade, S. Jensen and O. Hansen, J. Appl. Phys., 97 (2005) 044906.

[41] B. Hammer, L.B. Hansen and J.K. Nørskov, Phys. Rev. B, 59 (1999) 7413.

[42] H.J. Monkhorst and J.D. Pack, Phys. Rev. B, 13 (1976) 5188.

[43] D. Vanderbilt , Phys Rev. B, 41 (1990) 7892.

[44] J.H. Noggle, Physical Chemistry, Little, Brown and Co. 1985.

[45] F. Abild-Pedersen and M.P. Andersson, Surf. Sci., 601 (2007) 1747.

[46] F. Abild-Pedersen, O. Lytken, J. Engbæk, G. Nielsen, I. Chorkendorff and J.K. Nørskov, Surf. Sci., 590 (2005) 127.

Paper 2

Low Temperature Methane Oxidation on differently supported 2 nm Au Nanoparticles

Low Temperature Methane Oxidation on differently supported 2 nm Au Nanoparticles

G. Walther[1], L. Cervera-Gontard[2], U. Quaade[3], S. Horch[1,*]

[1] Center for Atomic-scale Materials Design (CAMD), Department of Physics
[2] Center for Electron Nanoscopy (CEN)
[3] Center for Individual Nanoparticle Functionality (CINF), Department of Physics
Technical University of Denmark, DK-2800 Kgs. Lyngby, Denmark
[*] Corresponding author: horch@fysik.dtu.dk

Low temperature CH_4 oxidation was studied on 2 nm gold nanoparticles supported on various metal-oxides. The differences in reaction rates for the different systems suggest that the support material has an effect on the activity. From TEM analysis, we found that the gold particles were stable in size during the reaction. In addition to full oxidation to CO_2, traces of C_2H_6 were detected when Au/TiO_2 was used, indicating limited partial CH_4 oxidation. TiO_2 was found to be the best support for gold nanoparticles both in terms of activity and gold particle stability.

Keywords: Gold; TiO_2; Al_2O_3; ZnO; Catalysis; Methane; Oxidation; Particle size

Introduction

All fossil fuels are mixtures of hydrocarbons. CH_4 is the most difficult of all hydrocarbons to oxidize. It is obvious that CH_4 is a much more suitable fuel source concerning its higher atomic ratio of H : C. Natural gas sources that mainly consist of CH_4, are so remote from the consumers that transportation of LNG (liquefied natural gas) is often uneconomic. Natural gas that is produced along with oil, is often flared and accounts with more than 20 billion cubic meters annually, and this has a significant detrimental effect on the environment [1]. Thus, there is a keen interest in converting CH_4 catalytically into higher valuable chemicals [2, 3], e.g. methanol, that is one of the seven building blocks in organic chemistry [4]. The reason why no good catalyst has been developed for low temperature partial CH_4 oxidation as yet is the higher reactivity of the products (CH_3OH and HCHO) compared to CH_4 [5]. Thermodynamically, complete combustion to CO_2 and H_2O is more favorable:

$$CH_4 + {}^1/_2\, O_2 \rightarrow CH_3OH \qquad \Delta H^0 = -126.4 \text{ kJ mol}^{-1} \qquad (1)$$

$$CH_4 + O_2 \rightarrow HCHO + H_2O \qquad \Delta H^0 = -284.2 \text{ kJ mol}^{-1} \qquad (2)$$

$$CH_4 + {}^3/_2\, O_2 \rightarrow CO + 2\, H_2O \qquad \Delta H^0 = -519.3 \text{ kJ mol}^{-1} \qquad (3)$$

$$CH_4 + 2\, O_2 \rightarrow CO_2 + 2\, H_2O \qquad \Delta H^0 = -802.3 \text{ kJ mol}^{-1} \qquad (4)$$

There are not very many studies dealing with CH_4 oxidation on gold, although gold has been shown to be surprisingly active for many other reactions, especially CO oxidation [6–24] and oxidation of hydrocarbons [8, 16, 17, 25–31], when it is nanosized on an oxide support . The source of this activity is still unclear. It is suggested to be associated with a quantum-size effect [7], support-induced strain [19], charge transfer from the small gold particles to adsorbed oxygen [32] and the role of low-coordinated gold atoms [19, 21–24]. It has also been suggested that the catalytic activity could perhaps be influenced by a relativistic effect on the 6s orbital of the heavier elements, especially Pt and Au [32a]. The major drawback to gold is its low melting point that can lead to sintering of gold nanoparticles [33–35] and then the activity may not be sufficient for an application at elevated temperatures. For catalytic reactions that take place on gold even at room temperature – such as CO oxidation– sintering of nanoparticulate gold has not been reported to occur.

Recently, we reported that CH_4 oxidation on TiO_2 supported gold nanoparticles proceeds at low temperature with a strong tendency to form CO_2 [36]. Partial oxidation of CH_4 to CO and H_2 has been studied on various other supported noble metal catalysts by Baiker *et al.*, who reported rates and selectivity between 300°C and 500°C [37]. For a Pt/Al_2O_3 catalyst it was recently reported that oxygen-rich surfaces seem to suppress the dissociative adsorption of CH_4, resulting in low CH_4 oxidation activity in excess oxygen [38]. At high temperatures (600°C – 800°C), it has been shown through isotope labeling studies on CH_4 reforming reactions over supported platinum clusters, that CO_2 activation steps are much faster than the kinetically relevant steps for CH_4 chemical conversion to synthesis gas [39]. The authors conclude in that study, that CO_2 activation steps must be quasi-equilibrated and kinetically irrelevant. Recent studies suggest that there is a condition dependent mechanism for the reforming reaction of CH_4 with CO formation being dominant at lower temperatures and CH_4 activation taking over at higher temperature [40].

In the present contribution, we focus on low-temperature CH_4 oxidation on various metal-oxide supported gold catalysts. The main objective in this experimental work is to study the contribution of the metal-oxide support to the catalytic reaction for different support materials. We present our findings based on steady-state activity measurements and TEM analysis. Another issue was to check whether by changing the support one could avoid the final oxidation step of CO to CO_2 at low temperature.

Experimental Section

Experimental Equipment

Steady-state activity measurements of various metal-oxide supported gold catalysts were performed in mini-reactors. These mini-reactors are basically quartz glass tubes that were heated using a hotplate. The temperature was measured with a K-type thermocouple and controlled using a PID-controller (Eurotherm). The reactants, CH_4 (5.5 purity) and O_2 (3.5 purity), were supplied and controlled using mass flow controllers (Bronkhorst). The total gas flow was kept constant for all measurements at 0.50 ml min^{-1}. The reaction products were analyzed using an Agilent gas chromatograph (3000A microGC). The GC has combined columns of 10 m molecular sieve and 3 m PLOT U with 1.0 µl back-flushing, which allows simultaneous analysis of CH_4, O_2, N_2, CO, CO_2, H_2, H_2O, C_2H_6, HCHO and CH_3OH by a thermal conductivity detector (TCD). With argon as the carrier gas, the GC is 15 times more sensitive to H_2 than to CO. To avoid condensation of water, formed by the catalytic reactions, the tubing between the mini-reactor and the GC was kept at a temperature of 100°C, whereas the capillary of the GC itself was kept at 90°C.

Method

Three different 2.0 nm gold catalysts (AURO*lite*™) were supplied by Project AuTEK [41]:

(A) Au/TiO_2 (1.02 wt% Au),
(B) Au/ZnO (0.978 wt% Au),
(C) Au/Al_2O_3 (0.84 wt% Au).

These catalysts had been prepared by carefully developed methods involving gold precipitation from solution [41]. To ensure reproducibility, each catalyst was first activated by a pre-treatment of 10 hours at 100°C and continuous gas flow of CH_4 and O_2 in the ratio of 1:2 as well as a temperature ramp from 30°C to 250°C in steps of 10°C h^{-1}, before the following sequence of CH_4:O_2 ratios was used: 1:2, 1:1, 2:1. The reaction according to the first step of the sequence was re-measured to confirm that the catalyst did not change during the reactions. To verify that the applied gases did not alter the catalysts, the described schemes were run once more in inverse order using a fresh catalyst. For steady-state activity measurements, the temperature was ramped from 30°C to 250°C in steps of 10°C h^{-1}.

Self heating of the catalyst during an exothermic reaction is difficult to avoid, but it can be minimized by operating the catalyst in the lower range of its kinetically controlled regime. The greatest amount of heat liberated during the reaction was 16.9 mW when CH_4 and O_2 were applied in the stoichiometric ratio to form CO_2 and H_2O at 250°C.

Particle Analysis

To confirm the particle size and the purity of the catalyst as stated by the supplier, we used both transmission electron microscopy (TEM) and X-ray fluorescence (XRF). For the latter technique, we used a Minipal 4 X-ray spectrometer (PANalytical). The size distribution and shape of the gold particles were probed using a Tecnai 20T TEM operating at 200 kV. Specimens of the catalyst were taken before and after the temperature-programmed activity measurements, and prepared on a carbon TEM grid. Detection of particles in a TEM image is usually performed by transforming the grayscale image into a binary image by *thresholding* the *whole* picture at once using a 'global threshold' value. This approach works well if all of the particles are dark enough with respect to the background intensity in the image, but often fails because of local changes in the contrast of the

TEM image. Here, instead, an algorithm based on local thresholding was applied to improve the detection of the particles.

Results

The purity of the catalysts used was checked using XRF. Catalyst B contained traces of Fe and Ni, in catalyst C were found traces of Fe and Cu, whereas impurities in catalyst A must have been below the detection limit of the system used. To study the influence of the pre-treatment and the catalytic reactions on the catalysts, TEM images were taken of specimens of the catalysts as supplied, after pre-treatment and after steady-state activity measurements. The average particle size of the catalysts, 2.0 nm, as stated by the supplier, could be confirmed for A and B, whereas C was found to be larger: 2.8±1.3 nm. Since Al_2O_3 is not a reducible metal oxide like TiO_2 or ZnO, to which oxygen vacancies usually are referred to be anchoring points for deposited nanoparticles, an enhanced sintering effect cannot be excluded. Probably, the gold particles were already sintered during storage.

TEM analysis on changes in particle size

Figure 1(a) shows a typical TEM image of Catalyst A after reaction. Remarkably, the particle size did not change drastically, either during the pre-treatment – *cf*. the red and the green distribution curves, or due to methane oxidation – *cf.* the green and the blue distribution curves in the graph below. After the reaction, the gold particles' size was determined to be 1.8±0.6 nm based on a TEM analysis of 81 particles. This behavior is in strong contrast to measurements after CO oxidation over a fresh catalyst of the same batch, that have been conducted at much lower temperatures than applied in this study [42], where substantial sintering was found. Our recent findings for CO oxidation on the same material as used for Catalyst A might have been affected by the use of different oxidation agents: O_2 and N_2O.

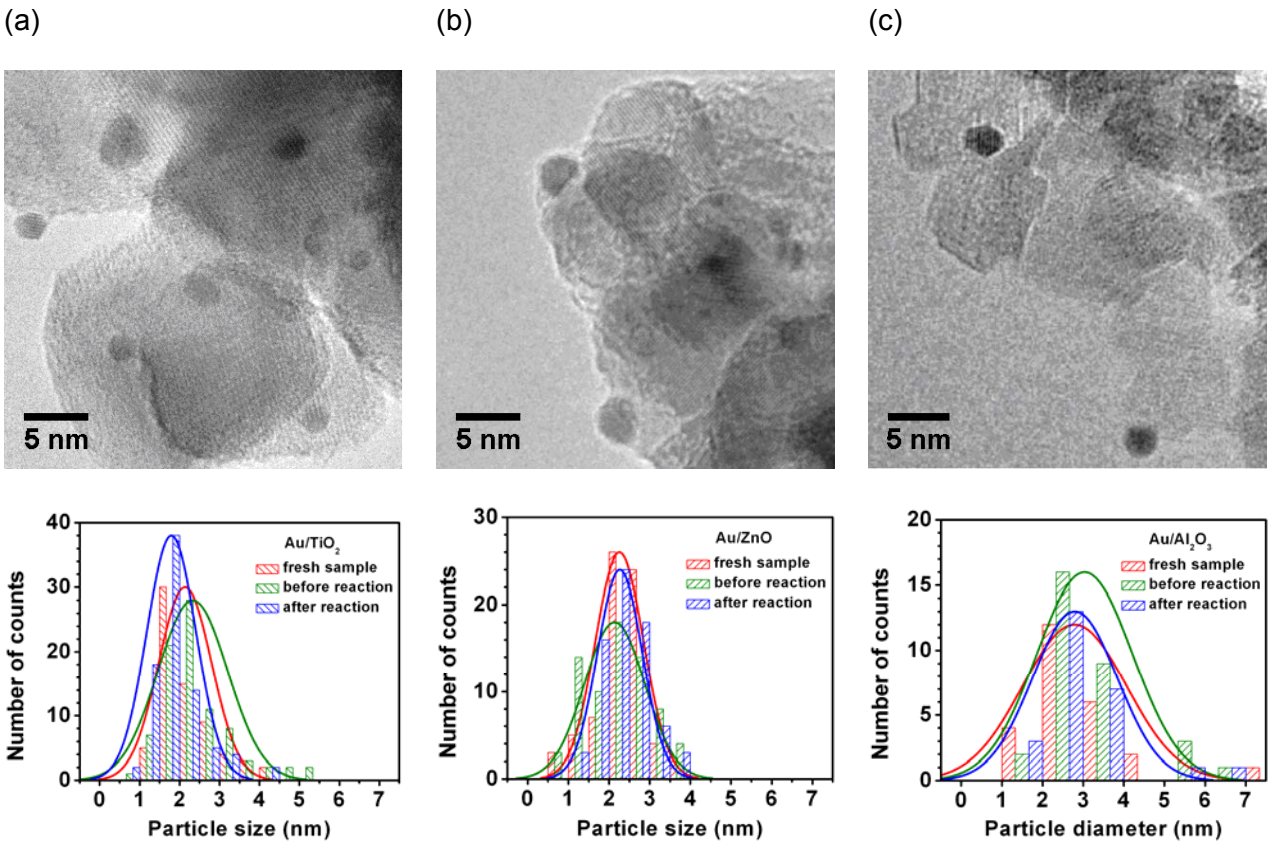

Figure 1
TEM image of the catalysts A, B and C after methane oxidation reactions together with the statistical analysis of the average particle size from all states of the catalysts – fresh (as supplied), after pre-treatment and after reactions – in the figures (a), (b) and (c), respectively.

The TEM image in Figure 1(b) shows gold particles observed after reaction on catalyst B. The average particle size was determined to be 2.3±0.6 nm. Also this catalyst was very stable, since the particle size did not change significantly.

Catalyst C contained right from the beginning bigger gold particles. The measurement of particle sizes from TEM images was difficult due to the high contrast of the Al_2O_3 crystals supporting the nanoparticles, and curves must be interpreted with caution. However, the size distribution indicates average particle sizes greater than that of the other two catalysts. After the reaction, the average particle size was still 2.8±1.0 nm.

Steady-state activity measurements

From the Arrhenius plots in Figure 2, the apparent activation energies for CH_4 oxidation on the three different catalysts evaluated were determined to be approximately the same for the feed gas ratio of CH_4 : O_2 = 1:2. The values are summarized in Table 1. The specific CH_4 oxidation rate indicates clearly that catalyst A was the most active one. For this catalyst the conversion of CH_4 to CO_2 according to equation (4) was greatest with 29% at 250 °C, as is shown in Figure 3. Since neither CO nor other organic chemicals were detected for this feed gas ratio, which according to Equations (1) – (3) would be an indication that partial CH_4 oxidation occurs, the yield of CO_2 is di-

rectly given by the consumption of CH_4. The onset of CH_4 oxidation was found to be 130°C for Catalyst A. On the other catalysts, CH_4 oxidation did not take place at temperatures below 150°C.

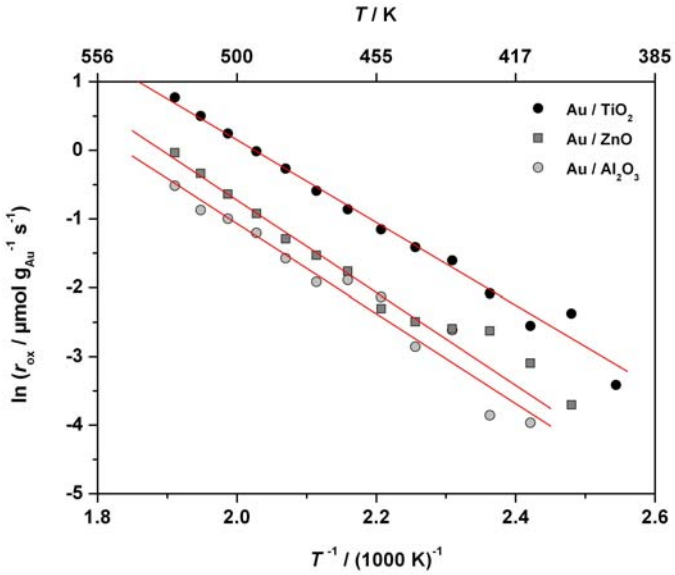

Figure 2
Arrhenius plots of the specific CH_4 oxidation rates: Catalyst A (●), Catalyst B (■), Catalyst C (○). The apparent activation energies are summarized in Table 1.

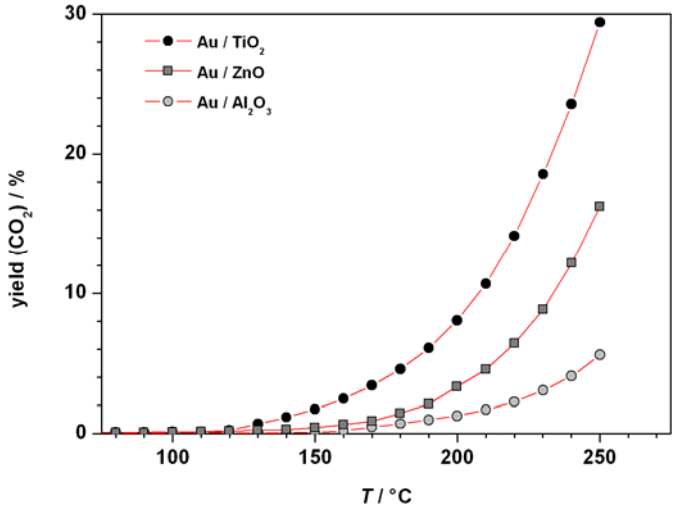

Figure 3
CH_4 conversion begins at 130°C when using Catalyst A (●), whereas for the Catalysts B (■) and C (○), the onset of conversion is around 150°C.

Besides the results shown here for an applied feed gas ratio of CH_4 : O_2 = 1:2, it is worth mentioning that traces of C_2H_6 could only be detected on Catalyst A and when the feed gas of reactants

was applied in a ratio of CH_4 : O_2 = 2:1. Considering the reaction represented by Equation 5 the greatest yield of C_2H_6 would be expected for CH_4 : O_2 = 4:1.

$$2\ CH_4 + {}^1/_2\ O_2 \rightarrow C_2H_6 + H_2O \qquad \Delta H^0 = -176.9\ kJ\ mol^{-1} \qquad (5)$$

This could be confirmed in a separate measurement, but the yield only doubled to 0.03% at 250°C, whereas the yield of CO_2 dropped down to 13%. No other products could be detected.

Discussion

Table 1 shows that the influence from the support material plays a minor role compared with the reduction of the overall reaction barrier: the apparent activation energies did not vary significantly. Concerning the specific rate for CH_4 oxidation, Catalyst A provided the highest turnover numbers of all the catalysts tested. This is probably also to some extent related to the fact that Catalyst A had the smallest gold nanoparticles. If we keep in mind that all the catalysts used were prepared by the same preparation method, it can be concluded from these results that TiO_2 is a good support for catalytically active gold. Compared to CO oxidation, we should note that the specific oxidation rate for CH_4 oxidation is, however, more than 150,000 times less than for CO oxidation on a catalyst of the same batch, already observed at a temperature of 80°C [42].

Table 1
Comparison of activation energies, reaction rates and yield of CO_2 at 250°C as well as the particle size determined using TEM.

	d_{Au} / nm	E_a / kJ mol^{-1}	ln(r_{ox} / µmol g_{Au}^{-1} s^{-1})	yield (CO_2) / %
catalyst A	1.8 ± 0.6	50 ± 1.1	0.77	29.4
catalyst B	2.3 ± 0.6	56 ± 1.7	-0.04	16.3
catalyst C	2.8 ± 1.0	53 ± 3.4	-0.52	5.6

In addition to the activity, we addressed the issue of stability by investigating changes in particle size using TEM. From our observations, nanosized gold seems to be inhibited from sintering during CH_4 oxidation. A similar non-sintering phenomenon was reported for alumina supported gold catalysts when 3*d*-metal oxides are added [43]. But it also has to be borne in mind that the catalysts in that study were first calcined at 400°C in O_2 and this led to sintering. Thus the particle size and the –still unidentified– active sites available, are not comparable with those of Catalyst C in our study. The results presented in this contribution are based on temperature programmed reaction experiments that had kept the catalyst at or above 200°C for 30 hours. To clarify whether this observed behavior is associated with CH_4 or OH present during the reaction, further research needs to be done.

Concerning the measured C_2H_6, three points are worth mentioning:
(a) The measurements with a CH_4 : O_2 ration of 4:1 show an enhancement in the C_2H_6 yield compared to those where the ratio is 2:1. Therefore, we can firstly conclude that C_2H_6 is a by-product of the reaction studied, and secondly that since the yield was only 0.03% in C_2H_6, gold has a high selectivity for CO_2. (b) Comparing equations (2) and (5), C_2H_6 formation is thermodynamically less likely than HCHO formation. The reason why C_2H_6 is formed instead needs further investigations. (c) The presence of C_2H_6 implies that there must be a pathway to partially oxidize CH_4 such that carbon goes from the oxidation state -4 to -3.

Another interesting issue is the strong tendency to form CO_2 irrespective of the support used, as it can be seen in the activity measurements presented. During CH_4 oxidation, we observed H_2O and CO_2 formed in a stoichiometric ratio as expected from Equation (4). From this result, we conclude that complete combustion of CH_4 takes place over all supports. Recent studies [36, 42] show that the lower overall barrier for CO oxidation (36 kJ mol^{-1} *vs*. 50 kJ mol^{-1} for CH_4 oxidation (*cf.* Table 1)) indicates that under these reaction conditions the post-oxidation of CO proceeds much faster than the oxidation of an adsorbed CH_4 species. Thus, for the overall reaction of CH_4 oxidation the elementary steps following the formation for CO_2 would be quasi-equilibrated. It is suggested that in a similar fashion the elementary steps for H_2 may well be quasi-equillibrated on this catalyst. Support for this viewpoint is that the overall barrier for H_2 oxidation is much lower as well (38 kJ mol^{-1}) [42]. Furthermore, atomic H (liberated from CH_4) might perhaps already form H_2O at an even lower activation barrier. This means that CH_4 oxidation is the rate-limiting step of the overall reaction for each of the support materials tested.

Conclusions

In this contribution, we have described investigations on various metal-oxide supported gold catalysts in terms of CH_4 oxidation under mild conditions (1 bar, 30°C – 250°C). Steady-state activity measurements show that CO_2 was formed with a high selectivity by complete combustion of CH_4 irrespective of the support used. Although nanoparticular gold is well known to sinter even at low temperature during other reactions, we did not find any indication of sintering from our TEM analysis. Further research needs to be done to clarify what causes the stability of gold under these conditions. Finally, we conclude that TiO_2 is the best support of those tested.

Acknowledgements

G. Walther gratefully acknowledges financial support from NABIIT and the support of gold catalysts from Project AuTEK. We also thank D.T. Thompson for stimulating discussions.

References

[1] V.S. Arutyunov, V.M. Rudakov, V.I. Savchenko, E.V. Sheverdenkin, O.G. Sheverdenkin and A.Yu. Zheltyakov, *Theo. Found. Chem. Eng.*, 2002, **36**, 472.

[2] C.-J. Liu, T. Hammer and R. Mallinson, *Catal. Today*, 2004, **98**, VII.

[3] M.O. Adebajo, *Green Chem*., 2007, **9**, 526.

[4] N.D. Parkyns, C.I. Warburton and J.D. Wislon, *Catal. Today*, 1993, **18**, 385.

[5] G.A. Olah and Á. Molnár, Hydrocarbon Chemistry, *Wiley-Interscience*, 2003.

[6] M. Haruta, *Catal. Today*, 1997, **36**, 153.

[7] M. Valden, X. Lai and D.W. Goodman, *Science*, 1998, **281**, 1647.

[8] G.C. Bond and D.T. Thompson, *Catal. Rev. – Sci. Eng.*, 1999, **41**, 319.

[9] M. Haruta, *Cat. Tech.*, 2002, **6**, 102.

[10] A.C. Gluhoi, M.A.P. Dekkers and B.E. Nieuwenhuys, *J. Catal.*, 2003, **219**, 197.

[11] B. Schuhmacher, V. Plzak, M. Kinne and R.J. Behm, *Catal. Lett*., 2003, **89**, 109.

[12] M. Chen and D.W. Goodman, *Science*, 2004, **306**, 252.

[13] T.V.W. Janssens, A. Carlsson, A. Puig-Molina and B.S. Clausen, *J. Catal.*, 2006, **240**, 108.

[14] H.-J. Freund, *Catal. Today*, 2006, **117**, 6.

[15] G.C. Bond, C. Louis and D.T. Thompson, Catalysis by Gold, *Imperial College Press, 1. Edition, London*, 2006.

[16] D.T. Thompson, *Topic. Catal.*, 2006, **38**, 231.

[17] C. Xu, J. Su, X. Xu, P. Liu, H. Zhao, F. Tian and Y. Ding, *J. Am. Chem. Soc.*, 2007, **129**, 42.

[18] B. Hammer, J.K. Nørskov, *Surf. Sci*., 1995, **343**, 211.

[19] M. Mavrikakis, P. Stotze, J.K. Nørskov, *Catal. Lett*., 2000, **64**, 101.

[20] Z. Liu, P. Hu and a. Alavi, *J. Am. Chem. Soc.*, 2002, **124**, 14770.

[21] N. Lopez and J.K. Nørskov, *J. Am. Chem. Soc.*, 2002, **124**, 11262.

[22] N. Lopez, T.V.W. Janssens, B.S. Clausen, Y. Xu, M. Mavrikakis, T. Bligaard and J.K. Nørskov, *J. Catal.*, 2004, **223**, 232.

[23] T.V.W. Janssens, B.S. Clausen, B. Hvolbæk, H. Falsig, C.H. Christensen, T. Bligaard, and J.K. Nørskov, *Topic. Catal.*, 2007, **44**, 15.

[24] B. Hvolbæk, T.V.W. Janssens, B.S. Clausen, H. Falsig, C.H. Christensen, and J.K. Nørskov, *NanoToday*, 2007, **2**, 14.

[25] R.D. Waters, J.J. Weimer and J.E. Smith, *Catal. Lett.*, 1994, **30**, 181.

[26] S. Ivanova, C. Petit, V. Pitchon, *Catal. Today*, 2006, **113**, 182.

[27] S. Ivanova, C. Petit, V. Pitchon, *Gold Bulletin*, 2006, **39**, 3.

[28] B.E. Solsona, T. Garcia, C. Jones, S.H. Taylor, A.F. Carley and G.J. Hutchings, *Appl. Catal. A*, 2006, **312**, 67.

[29] A.S.K. Hashmi and G.J. Hutchings, *Angew. Chem. Int. Ed.*, 2006, **45**, 7896.

[30] C.H. Christensen, B. Jørgensen, J. Rass-Hansen, K. Egeblad, R. Madsen, S.K. Klitgaard, S.M. Hansen, M.R. Hansen, H.C. Andersen and A. Riisager, *Angew. Chem. Int. Ed.*, 2006, **45**, 4648.

[31] M.-C. Daniel and D. Astruc, *Chem. Rev.*, 2004, **104**, 293.

[32] J.A. v. Bokhoven, C. Louis, J.T. Miller, M. Trommp, O.V. Safonova and P. Glatzel, *Angew. Chem.*, 2006, **118**, 4767.

[32a] G.C. Bond, *Catal.Today*, 2002, **72**, 5.

[33] P. Buffat and J.P. Borel, *Phys. Rev. A*, 1976, **13**, 2287.

[34] E. Charls, H. Sykes, F.J. Williams, M.S. Tikhov and R.M. Lambert, *J. Phys. Chem. B*, 2002, **106**, 5390.

[35] P.M. Ajayan and D.L. Marks, *Phys. Rev. Lett*., 1988, **60**, 585.

[36] G. Walther, G. Jones, S. Jensen, U. Quaade, S. Horch, *Catal. Today*, accepted.

[37] S. Hannemann, J.-D. Grunwaldt, P. Lienemann, D. Günther, F. Krumeich, S.E. Pratsinis and A. Baiker, *Appl. Catal. A*, 2007, **316**, 226.

[38] E. Becker, P.-A. Carlsson, H. Grönbeck and M. Skoglundh, *J. Catal.*, 2007, **252**, 11.

[39] J. Wei and E. Iglesia, *J. Phys. Chem. B*, 2004, **108**, 4094.

[40] M.P. Andersson, F. Abild-Pedersen, I.N. Remediakis, T. Bligaard, G. Jones, J. Engbæk, O. Lytken, S. Horch, J.H. Nielsen, J. Sehested, J.R. Rostrup-Nielsen, J.K. Nørskov and I. Chorkendorff, *J. Catal.*, 2008, **255**, 6.

[41] http://www.mintek.co.za.

[42] Guido Walther *et al.*, In Preparation.

[43] R.J.H. Griesel and B.E. Nieuwenhuys, *Catal. Today*, 2001, **64**, 69.

Paper 3

Oxidation of CO and H_2 by O_2 and N_2O on Au/TiO_2 Catalysts in Microreactors

Oxidation of CO and H_2 by O_2 and N_2O on Au/TiO_2 Catalysts in Microreactors

G. Walther [a], D. J. Mowbray [a], T. Jiang [a], G. Jones [a], S. Jensen [b], U. J. Quaade [c], and S. Horch [a,*]

[a] *Center for Atomic-scale Materials Design (CAMD), Department of Physics*

[b] *Department of Micro and Nanotechnology (MIC)*

[c] *Center for Individual Nanoparticle Functionality (CINF), Department of Physics*

NanoDTU, Technical University of Denmark, DK-2800 Kgs. Lyngby, Denmark

Abstract

We performed steady-state activity measurements in microreactors to obtain the reaction rates for CO and H_2 oxidation . These reactions were studied on three different gold particle sizes ($d \approx 3.6$, 5.7, 16.2 nm) using either O_2 or N_2O as oxidation agents oxidizing agents. From our TEM analysis, our CO oxidation rates follow the d^{-3} relationship proposed in [*Nano Today* **2**, 14 (2007)]. Density functional theory (DFT) calculations on a Au{532} surface and a Au_{12} cluster, which model corner sites, reproduced the apparent activation barriers of about 37 kJ mol^{-1} for CO oxidation on the smallest nanoparticles by both O_2 and N_2O. For all of the reactions studied, we found the overall activation barrier depended only on the size of the TiO_2 supported gold nanoparticle.

Key words: gold, nanoparticles, catalysis, microreactor, carbon monoxide, hydrogen, oxygen, nitrous oxide, particle size, sintering, TEM

1 Introduction

In the past, gold was not thought to be catalytically active, and was even called "the noblest of all the metals" [1]. However, the discovery by Haruta *et al.* [2] that nano-particulate gold is catalytically active for CO oxidation, has provoked an academic "gold rush". This is evidenced by the exponential increase in gold catalysis publications since the early 1990s [3–6].

* Corresponding author
Email address: horch@fysik.dtu.dk (S. Horch).

Many different experimental studies have been performed to understand gold's activity for CO oxidation. These investigations considered changes of the particle's morphology [7, 8], a structure–activity relationship [9–11], the activity of unsupported nanoporous bulk gold [12, 13], and the influence of the support on the activity [14]. CO oxidation has also been thoroughly studied theoretically using density functional theory (DFT) [1, 6, 15–19]. Besides CO oxidation, many other reactions have been studied on gold catalysts. These include the oxidation of hydrocarbons [5, 20–24] and oxygen-containing hydrocarbons [3–5, 21, 25] as well as the catalytic hydrogenation of organic compounds [4, 5, 26].

In particular, CH_4 oxidation includes in the tail of its oxidation pathway CO oxidation and H_2 oxidation, since it only forms CO_2 and H_2 on gold catalysts [27]. Since there is a keen interest in converting CH_4 into more valuable monocarbon chemicals, it is necessary to first identify both the reaction pathway and active sites for CO and H_2 oxidation by different oxidizing agents.

The reason for this surprising activity is still under debate. After the pioneering work of Haruta [28], the activity of gold has been linked to several different effects. These include quantum-size effects [9], support-induced strain [15], charge transfer from the small gold particles to adsorbed O_2 [29] and the role of low-coordinated gold atoms [6, 15, 17–19].

It has recently been demonstrated that the CO oxidation activity of gold nanoparticles is inversely proportional to the cube of the average particle size ($\sim d^{-3}$), independent of the support material used [30]. This suggests that it is the corner sites which are the most active for CO oxidation by O_2.

The common oxidizing agent for CO oxidation, used in all the above studies was O_2. Very few studies deal with other oxidation agents, such as N_2O, and they focus on the decomposition and reduction of N_2O [31]. Since N_2O is known to readily dissociate into adsorbed atomic O and gas phase N_2 in the presence of CO, the oxidation of CO by N_2O involves atomic O. On the other hand, CO oxidation using O_2 has been shown to also occur via an alternative pathway, which does not include O_2 dissociation [16, 32]. By using these two different oxidizing agents, we may experimentally compare Au nanoparticle activity for two different CO oxidation pathways.

In the present contribution, we compare the reaction rates for CO and H_2 oxidation on three different particle sizes using either O_2 or N_2O as the oxidizing agent. To corroborate our experimental findings, we also modeled the CO oxidation turnover frequency using DFT calculations on the Au$\{532\}$ surface and Au_{12} cluster in a microkinetic model. Our findings suggest that such a model quantitatively describes the kinetics of CO oxidation using small Au nanoparticles ($d < 5$ nm).

2 Methods

2.1 Experimental Equipment

All experiments were performed in microreactors, based on deep reactive ion-etched (DRIE) silicon wafers. Details of the fabrication process are provided in Ref. [33]. Figure 1 illustrates the 280 μm deep capillary system that allows mixing of undiluted gases on the chip, without any danger of explosion. The dimensions of the reactor chamber are (8.0 × 1.5 × 0.2) mm^3. The whole device measures 20 mm × 15 mm × 0.35 mm and is sealed with a Viton sheet. The inlet and outlet holes are sealed with Viton O-rings to a heatable interface block that connects the external tubing to the microreactor. The temperature was measured with a K-type thermocouple and controlled using a PID-controller (Eurotherm). The gas flow was controlled by mass flow controllers (Bronkhorst), operating in the range from 0.02 to 1.00 ml min^{-1} with a precision of 0.02 ml min^{-1} at 1 bar.

The reaction products were analyzed using an Agilent gas chromatograph (3000A microGC). The GC has combined columns of 10 m molecular sieve and 3 m PLOT U with 1.0 μl back-flushing, which allows simultaneous analysis of H_2, O_2, N_2, CO, CO_2, H_2O and N_2O by a thermal conductivity detector (TCD). To avoid condensation of water, formed by the catalytic reaction of H_2, the tubing between the microreactor and the GC was kept at 100°C, whereas the capillary of the GC itself was kept at 90°C.

The catalysts used were 2.0 nm Au particles supported on TiO_2 (AURO$lite^{TM}$, supported by AuTEK [34]), 3.3 nm Au particles supported on TiO_2 powder (reference catalyst, supplied by the World Gold Council [35]), and 5.0 nm Au particles on TiO_2, which we shall denote as Catalysts A, B, and C, respectively. Catalysts A

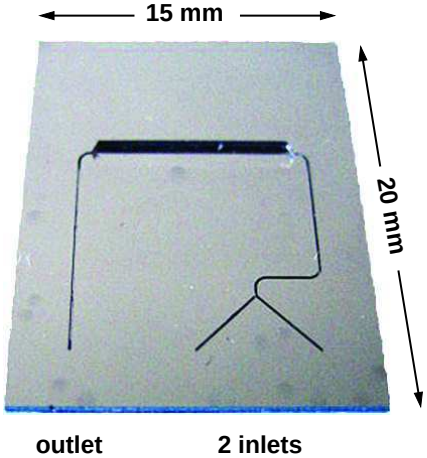

Fig. 1. Unloaded microreactor, based on silicon, with two inlets to mix gases on the chip, a (8.0 × 1.5 × 0.2) mm^3 reactor chamber and a single outlet.

and B were both supported on TiO_2 P25, as stated by the suppliers.

However, Catalyst C was prepared by deposition-precipitation of unconjugated gold colloids (Ted Pella, Inc.) on anatase TiO_2 powder (Millennium Inorganic Chemicals) with an average BET area of 150–300, according to the supplier. For ease of comparison, the gold concentration of the in-house catalysts was carefully adjusted to those of the commercially available samples. The preparation was performed below 50°C to evaporate the solvent. After the catalyst had been dried, it was calcined at 200°C.

2.2 Catalytic Reactions

We studied two different reactions on the three different gold catalysts listed above, using the two different oxidizing agents O_2 (3.5N) and N_2O (2.5N). The overall reactions and heats of formation ΔH^0 [36] are then

$$\mathrm{CO} + \mathrm{N_2O} \rightarrow \mathrm{CO_2} + \mathrm{N_2} \qquad \Delta H^0 \approx \text{-200.9 kJ mol}^{-1} \qquad \text{(R1)}$$

$$\mathrm{CO} + {}^1\!/_2\,\mathrm{O_2} \rightarrow \mathrm{CO_2} \qquad \Delta H^0 \approx \text{-283.0 kJ mol}^{-1} \qquad \text{(R2)}$$

$$\mathrm{H_2} + \mathrm{N_2O} \rightarrow \mathrm{H_2O} + \mathrm{N_2} \qquad \Delta H^0 \approx \text{-159.8 kJ mol}^{-1} \qquad \text{(R3)}$$

$$\mathrm{H_2} + {}^1\!/_2\,\mathrm{O_2} \rightarrow \mathrm{H_2O} \qquad \Delta H^0 \approx \text{-241.8 kJ mol}^{-1} \qquad \text{(R4)}$$

Due to the high sensitivity of the GC to H_2, the reactants in (R4) and (R3) were diluted with 50% argon with the total flow kept constant at 1.00 ml min^{-1} for all reactions.

To minimize the contribution of self-heating of the catalyst during an exothermic reaction, all experiments were performed with a maximum of 10% conversion, except for CO oxidation where 15% was achieved at 60°C on Catalyst A and more than 40% at 80°C on Catalyst B. The greatest amount of heat liberated during the reactions was 26.0 mW.

To ensure reproducibility, we followed the following scheme for all measurements. First, all catalysts were activated. Catalysts B and C, containing the larger particles, were pretreated over 20 hours at 80°C to ensure steady-state activity measurements. On the other hand, due to its high activity and the possibility of sintering, Catalyst A was pretreated for 20 hours at 50°C. These pretreatments were done under stoichiometrically supplied CO and O_2, for the reaction $\mathrm{CO} + {}^1\!/_2\,\mathrm{O_2} \rightarrow \mathrm{CO_2}$, and a total gas flow of 1.00 ml min^{-1}. The CO conversion decreased by 33%, 17%, and 5% before stabilizing for the powder Catalysts A, B, and C, respectively. Temperature programmed activity measurements were then performed in the following sequence of reactions for each catalyst: (R2), (R1), (R3), (R4), (R2), (R1).

Since the maximum temperature reached under these reactions (120°C on Catalyst B and 160°C on Catalyst C) was higher than the temperature of the pretreatment (80°C), the last two steps (re-measurement of (R2) and (R1)) were performed to ensure that the catalysts had not changed during the preceding reactions. Furthermore, to exclude any influence of the applied gases (by e.g. catalyst reduction), the reaction sequence was also conducted in reversed order —starting with (R2)— on a fresh and deactivated catalyst from the same batch. Hereby, the rate differed for each of the reactions (R1) – (R4) studied, but the proportions between (R2) and (R1), and between (R4) and (R3) were similar.

2.3 Particle Analysis

Transmission electron microscopy (TEM) was used to study changes in size of the gold particles. For each catalyst, specimens were taken as the catalysts were supplied, after the pretreatment and after measurements of all four catalytic reactions. The specimens were then prepared on a carbon TEM grid by dropping a suspension of catalyst in ethanol on the grid. These were analyzed using a JEOL 3000F field emission electron microscope, which was operated at 300 kV with a LaB_6 filament as an electron source.

2.4 Theoretical Methodology

All theoretical results have been obtained using the DFT code DACAPO [37]. The Kohn-Sham one-electron valence states were expanded in a plane wave basis set with a 340 eV (25 Ry) kinetic energy cutoff, and a density cutoff of 680 eV (50 Ry). The core electrons were described by Vanderbilt type ultrasoft pseudopotentials [38]. The exchange-correlation potential was described using the RPBE generalized gradient approximation self-consistently [39]. For the Au$\{532\}$ surface, a $4\times4\times1$ Monkhorst-Pack **k**-point sampling was applied in the irreducible Brillouin zone. The surface was modeled by a 1×1-$\{532\}$ unit cell containing 24 Au atoms with periodic boundary conditions, which corresponds to three close-packed layers. The top most layer and the adsorbents were allowed to fully relax. The O_2 adsorption energy was calculated relative to the experimentally-obtained formation energy of H_2O from O_2 and H_2 [40]. This avoids difficulties associated with a DFT treatment of the O_2 triplet state in the gas phase [41].

Thermodynamic analysis was carried out using the total energies obtained from the DFT calculations. It is then possible to obtain free energies by augmenting the DFT total energies with the thermodynamics of a classical ideal gas [42]. For a gas-phase species X at temperature T and pressure p, the Gibbs free energy $G_{\mathrm{X}}(p,T)$ is given by

Table 1
Activation barriers E_a and adsorption energies E_{ads} in kJ mol^{-1} for CO and H_2 oxidation by N_2O and O_2 [44].

E / kJ mol^{-1}	Au{532} surface	Au_{12} cluster
$E_{ads}[O_2]$	-27.0	-60.8[a]
E_{ads}[CO]	-74.3	-91.7[a]
$E_{ads}[N_2O]$	-7.7[b]	-7.7[b]
$E_a[CO + O_2 \rightarrow CO_2 + O]$	—	27.0[a]
$E_a[CO + O \rightarrow CO_2]$	27.0	—

[a]Ref. [30], [b]Ref. [43]

$$G_{\mathrm{X}}(p,T) = E_{\mathrm{X}} + E_{\mathrm{ZPE}} + \Delta H(T) - TS(T) + RT\ln(p/p_0), \tag{1}$$

where E_{ZPE} is the zero point energy, $\Delta H(T)$ denotes the enthalpy change due to raising the temperature from 0 K to T, $S(T)$ is the entropy at T, R is the universal gas constant, and p_0 denotes the standard pressure (taken to be 1 bar).

The potential energy of an adsorbed species X*, E_{X}, is given by $E_{*/\mathrm{X}*} - E_*$, where E_* is the energy of the clean surface and $E_{*/\mathrm{X}*}$ is the energy of the adsorbate and the surface system. In order to calculate the free energy of this species, we neglect the pressure term, so that the enthalpy change is replaced by the change in internal energy. This leads to the following expression for the free energy $G_{\mathrm{X}}(p,T)$:

$$G_{\mathrm{X}}(p,T) = E_{\mathrm{X}*} + E_{\mathrm{ZPE}} + \Delta U(T) - TS(T). \tag{2}$$

The forward rate constant for a reaction i may then be expressed in terms of the Gibb's free energies as $k_i = v_i \exp[-\Delta G/RT]$, where $\Delta G = \sum_{\mathrm{X}\in\mathcal{P}} G_{\mathrm{X}} - \sum_{\mathrm{X}\in\mathcal{R}} G_{\mathrm{X}}$ is the difference of the total Gibb's free energy of the products $\mathcal{P}$ and reactants $\mathcal{R}$ for reaction i, and R is the universal gas constant. The pre-exponetial factor in units of s^{-1} is $v_i \equiv k_{\mathrm{B}}T/h$, where k_{B} is the Boltzmann's constant.

The DFT energies for the adsorbed species $E_{\mathrm{X}*}$ as well as the activation barriers are given in Table 1. For the N_2O adsorption energy, we have used the experimental value given in Ref. [43].

2.5 Microkinetic Model

Using the notation of Ref. [45], we may express any heterogeneous catalysis reaction in the form

$$\mathrm{R(g)} \xrightarrow{*} \mathrm{P(g)}, \tag{R5}$$

where R(g) denotes the gas phase reactants, " * " the active sites on the catalyst, and P(g) the products in the gas phase. If we assume a Langmuir–Hinshelwood mechanism for the reaction kinetics, we may write the elementary steps in the form

$$\mathrm{X(g)} + * \rightleftarrows \mathrm{X}*, \quad \forall\, \mathrm{X} \in \mathcal{R}, \tag{R5a}$$

$$\mathrm{R}* \xrightarrow{\text{rds}} \mathrm{P(g)} + *. \tag{R5b}$$

The turnover frequency for the rate determining step (rds) is then

$$f_{\text{rds}} \approx k^{+}_{\text{rds}} \prod_{\mathrm{X}\in\mathcal{R}} \Theta_{\mathrm{X}*}, \tag{3}$$

where $\Theta_{\mathrm{X}*}$ is the fractional coverage of species X on site " * ", and k^{+}_{rds} is the rate constant for the forward rate, which we assume dominates the total reaction rate.

Assuming the difference in zero point energies of the products and the reactants ΔE_{ZPE} is much smaller than the activation barrier $E_a[\text{rds}]$, and the entropy of the adsorbed species is much smaller than that of the species in gas phase, $S_{\mathrm{X}*} \ll S_{\mathrm{X(g)}}$, we may express the forward rate constant for the rds as

$$k^{+}_{\text{rds}} \approx \frac{k_{\mathrm{B}}T}{h} \exp\left[-\frac{E_a[\text{rds}] - T\sum_{\mathrm{X}\in\mathcal{P}} S_{\mathrm{X(g)}}}{RT}\right]. \tag{4}$$

Since the adsorption steps are assumed to occur in equilibrium, the net rate

$$r_{\mathrm{X}*} = k^{+}_{\mathrm{X}*} p_{\mathrm{X}} \Theta_{*} - k^{-}_{\mathrm{X}*} \Theta_{\mathrm{X}*} = 0, \tag{5}$$

so that

$$\Theta_{\mathrm{X}*} = \frac{k^{+}_{\mathrm{X}*}}{k^{-}_{\mathrm{X}*}} p_{\mathrm{X}} \Theta_{*} = K_{\mathrm{X}*} p_{\mathrm{X}} \Theta_{*}, \tag{6}$$

where p_X is the gas phase pressure of species X, while $K_{\mathrm{X}*}$ is the ratio of the forward to backward rate constants. This may be expressed explicitly in terms of the adsorption energy $E_{ads}[\mathrm{X}]$ and gas phase entropy $S_{\mathrm{X(g)}}$ of species X as

$$K_{\mathrm{X}^*} \approx \exp\left[-\frac{E_{ads}[\mathrm{X}] + TS_{\mathrm{X(g)}}}{RT}\right], \tag{7}$$

where we again assume $S_{\mathrm{X}^*} \ll S_{\mathrm{X}}$ and ΔE_{ZPE} is much smaller than the adsorption energy of species X.

3 Results

3.1 Preliminary Investigations

We shall first focus on the thermodynamically unstable N_2O, when it is applied to the catalyst and to the bare support material only. At temperatures below 160°C no dissociation of N_2O could be measured on either Catalyst B, Catalyst C or bare TiO_2 (Degussa P25). However, in the presence of a reducing agent, e.g. H_2 or CO, N_2O could be reduced over the catalysts, but not over the bare support material [31].

Additionally, CO and O_2 were applied to bare TiO_2 in a stoichiometric ratio of 2:1 to check whether (R2) proceeds on the bare support. This was not the case.

3.2 TEM Investigation on Changes in Particle Size

Prior to discussing individual reactions, we will first analyze TEM images of the catalysts (*cf.* Figure 2) to evaluate the influence of pretreatment and catalytic reactions on the gold particles. Numerical values for the change in particle size of each catalyst are summarized in Table 2.

The TEM images in Figure 2(a) show typical images of Catalyst A from its state as supplied (i), its state after the pretreatment (ii) and its state after catalytic reactions (iii). The particles may potentially sinter during storage. However, this was not the case, since the average of the particle size in (a) (2.3 $\pm$0.6 nm), based on TEM images of 97 particles, is consistent with that stated by the supplier (2.0 nm). The particles appear predominately in a truncated cuboctahedron shape. Following the pretreatment, the average particle size was determined to be 2.6 $\pm$0.6 nm. The particles themselves were still well dispersed on the support, as can be seen in Image 2(a)(ii). Following the catalytic reactions, the gold particles were sintered to 3.6 $\pm$0.8 nm.

The size of the gold particles from Catalyst B stated by the supplier (3.3 nm), was also confirmed, as may be seen in Image 2(b)(i). Image 2(b)(ii) shows the

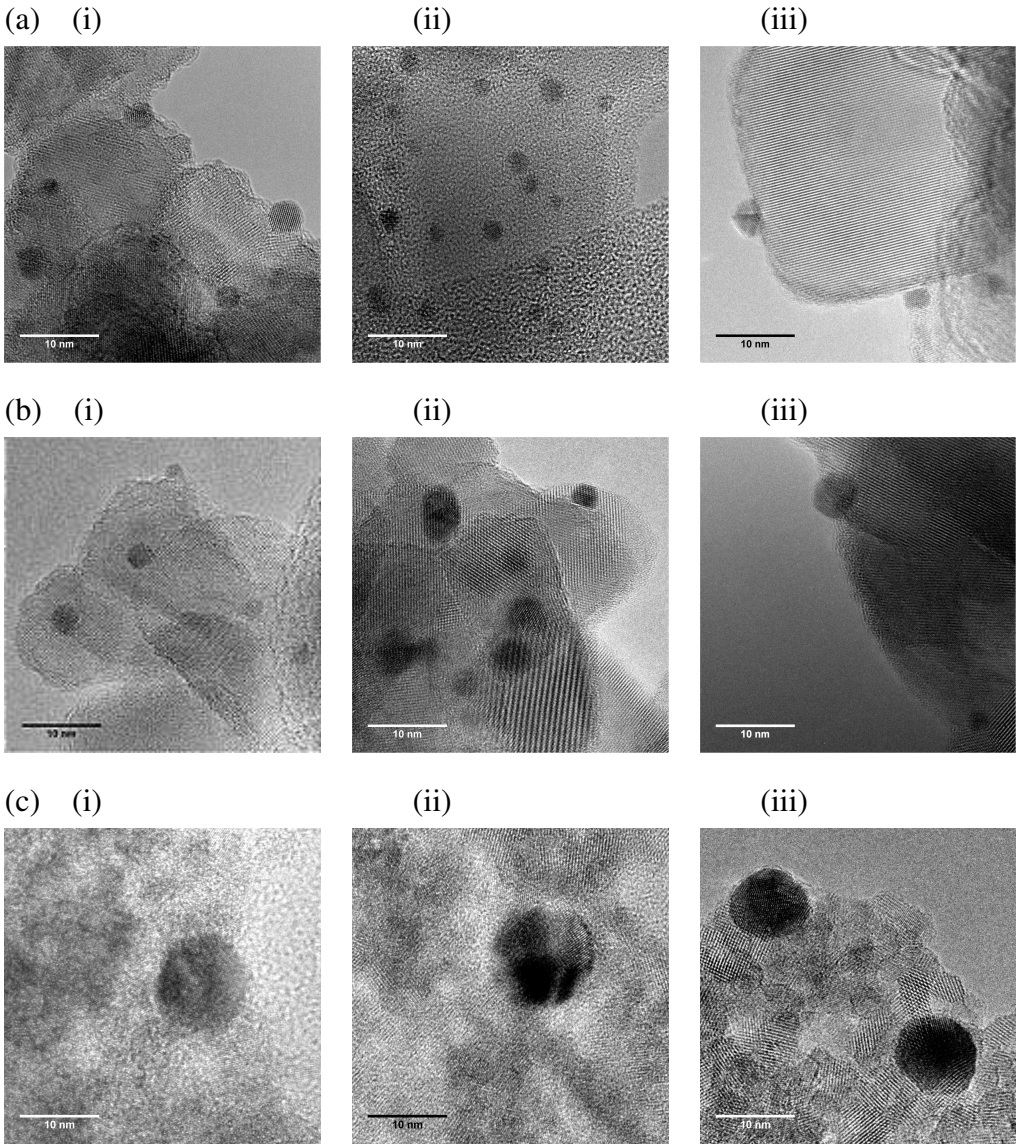

Fig. 2. Bright field TEM images of TiO_2 supported gold particles of Catalyst A (a), Catalyst B (b) and Catalyst C (c), as they were supplied/prepared (i), after the pretreatment (ii) and after catalytic reactions (iii). A summary of the change in particle size may be found in Table 2. The scale bars correspond to 10 nm in each image.

particles observed after pretreatment, which were only slightly larger. However, after reactions the gold particles' size increased significantly, *cf.* Image 2(b)(iii).

Figure 2(c) shows Catalyst C, which was formed in-house. Already during preparation, the gold particles sintered from 5.0 nm, as supplied in solution, to 13.3 $\pm$6.5 nm and formed truncated cuboctahedrons. The pretreatment led to further sintering, with the average particle size becoming 16.2 $\pm$6.6 nm. This catalyst did not show any further changes in size after catalytic reactions.

Table 2
Average TiO_2 supported gold particle size d in nm, as determined by TEM, before and after performing oxidation reactions.

d_{Au} / nm	gold concentration	total gold loading	as supplied† or prepared‡	before reaction	after reaction
Catalyst A	1.02 wt%	62.22 µg	2.3±0.6 †	2.6±0.6	3.6±0.8
Catalyst B	1.56 wt%	63.96 µg	3.4±0.8 †	3.8±1.1	5.7±3.4
Catalyst C	1.60 wt%	54.00 µg	13.3±6.5 ‡	16.2±6.6	16.2±6.6

3.3 Steady-state Activity Measurements

Figure 3(a) shows Arrhenius plots for (R1) – (R4) on Catalyst A. Surprisingly, the activation energies obtained were all approximately 37 kJ mol^{-1}, as may be seen from the parallel linear fits. Table 3 summarizes these and the following activation energies. However, for CO oxidation the reaction rate differs by a factor of 2.7, when comparing the different oxidation agents with each other. For H_2 oxidation, the catalyst behaves similarly. The linear fits run parallel and the reaction rate differs by 3.2. On the Au particles of Catalyst B, which were sintered to 5.7 nm, the trend depicted on Catalyst A continues, but is even more distinct, as shown in Figure 3(b). There is approximately one order of magnitude between the rates of CO oxidation and for H_2 oxidation, using N_2O and O_2, respectively.

For CO oxidation by O_2 on Catalyst B, the reaction rate was found to reach a maximum at about 80°C, *cf.* Figure 3(b). One reason for this may be that the catalyst was operated under mass-transport controlled conditions, e.g. when too little active material has been used. On the other hand, this may also be due to CO or O_2 desorption. Despite this, the parallel running fits of the Arrhenius plots again indicate similar activation energies around 39 kJ mol^{-1}, as shown in Table 3. These two catalysts where active even at room temperature, although O_2 was a significantly better oxidizing agent. For (R1), N_2 released from N_2O could be balanced with the CO_2 formed, indicating that the CO_2 does not originate from other sources.

Figure 3(c) shows Arrhenius plots for Catalyst C and demonstrates that on this catalyst N_2O is the better oxidizing agent for CO, whereas no difference in rate could be found for H_2 oxidation. A very similar apparent activation energy of about 60 kJ mol^{-1} was again found for all the four studied reactions. On these large particles an onset of conversion could not be observed below 80°C.

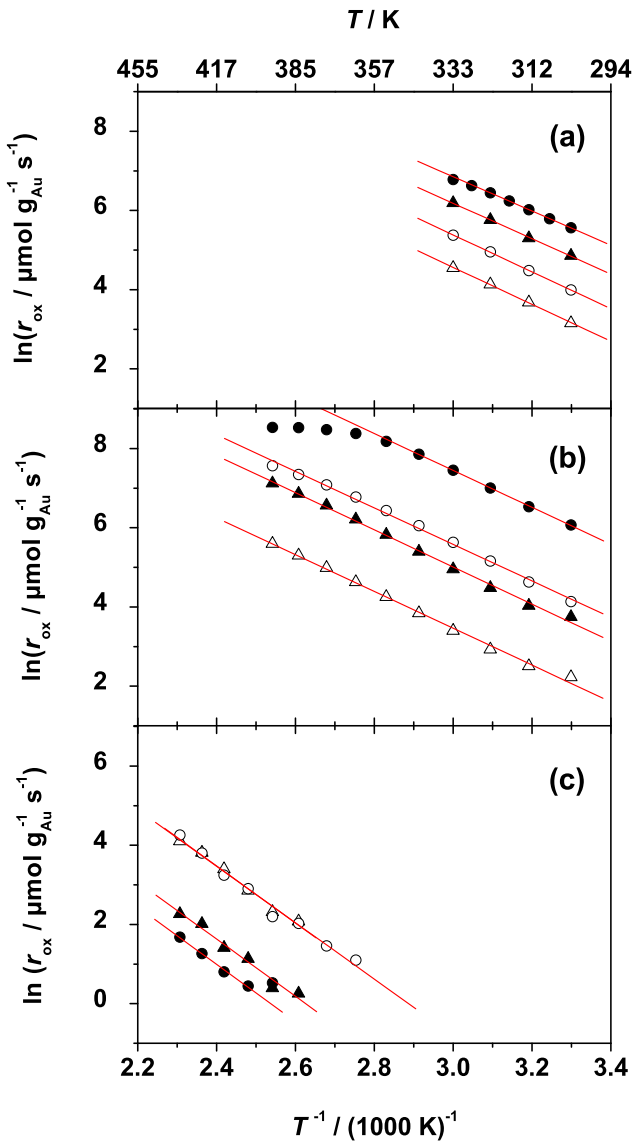

Fig. 3. Arrhenius plots of the activation energies for the four reactions on TiO_2 supported gold particles of Catalyst A (a), Catalyst B (b) and Catalyst C (c): CO + $^1/_2$ O_2 (●), CO + N_2O (▲), H_2 + $^1/_2$ O_2 (○) and H_2 + N_2O (△). An overview of the activation energies is given in Table 3.

3.4 Theoretical Results

It has recently been shown that for small Au nanoparticles ($d \lesssim 5$ nm) at 273 K, experimentally obtained CO oxidation rates follow a d^{-3} relationship, independent of the support material used [6, 11, 19]. This strongly suggests that corner sites are the active sites on small gold nanoparticles, in agreement with recent DFT studies [11, 18]. By extrapolating the linear fit of our CO oxidation rate measurements for Catalyst A to 273 K, *cf.* Figure 3(a), we find an estimated reaction rate of approximately 66 µmol g^{-1} s^{-1} for $d \approx 3.6$ nm. This agrees well with the d^{-3}

relationship of Nørskov *et al.* [6], where a fit to data from over 60 different sources on five different supports is presented. This is not altogether surprising, since this fit was generated by assuming the gold nanoparticle shape is the top half of a regular cuboctahedron, as is the case for our catalysts *cf.* Figure 2.

On the other hand, the reactivity of the Au–TiO_2 interface introduces a d^{-2} correction term to the reaction rate, which becomes important for larger gold nanoparticles similar to Catalyst C. However, due to the computational complexity of properly treating the Au–TiO_2 interface for large nanoparticles, we shall restrict consideration to reactions which occur on the corner sites of the Au particles.

We begin by first considering CO oxidation using N_2O. It has been generally accepted that the reaction kinetics for CO oxidation over a metal surface follow the Langmuir–Hinshelwood mechanism. According to this, the elementary steps of adsorption and desorption are in equilibrium, and (R1) may be written in terms of the following elementary steps:

$$\mathrm{CO(g)} + * \rightleftarrows \mathrm{CO}* \tag{R1a}$$

$$\mathrm{N_2O(g)} + {}^{\star} \rightleftarrows \mathrm{N_2O}^{\star} \tag{R1b}$$

$$\mathrm{CO}* + \mathrm{N_2O}^{\star} \xrightarrow{\text{rds}} \mathrm{CO_2(g)} + \mathrm{N_2(g)} + * + {}^{\star} \tag{R1c}$$

Here we have assumed that CO and N_2O adsorb on different corner sites, denoted by " * " and " * " respectively. This is clearly the case for CO oxidation, as may be seen from the transition states depicted in the insets of Figure 4.

Since we found N_2O does not dissociate spontaneously on gold, as has also been reported by Gluhoi *et al.* [31], we assume this reaction requires adsorbed CO* as a reducing agent. However, the overall barrier for (R1c) should still be the same as for CO oxidation with atomic O. On the other hand, the desorption of both N_2 and CO_2 should occur spontaneously.

To model the corner sites of a gold nanoparticle for reaction (R1c), we have chosen a Au$\{532\}$ surface, which consists of both B5 and kink sites. This allows atomic O to adsorb on the preferred B5 sites while CO adsorbs on the kink sites. This is depicted in the Au$\{532\}$ transition state for (R1c), shown in the lower inset of Figure 4. Since the Au_{12} cluster model of a corner site [30] does not include B5 sites for atomic O adsorption, it yields an activation barrier for (R1c) twice that found for the Au$\{532\}$ surface. For this reason, the Au_{12} model should not be used to model (R1c).

Employing the microkinetic model described above, the turnover frequency for the rate determining step (rds) f_{rds} in s^{-1}, may then be approximated by

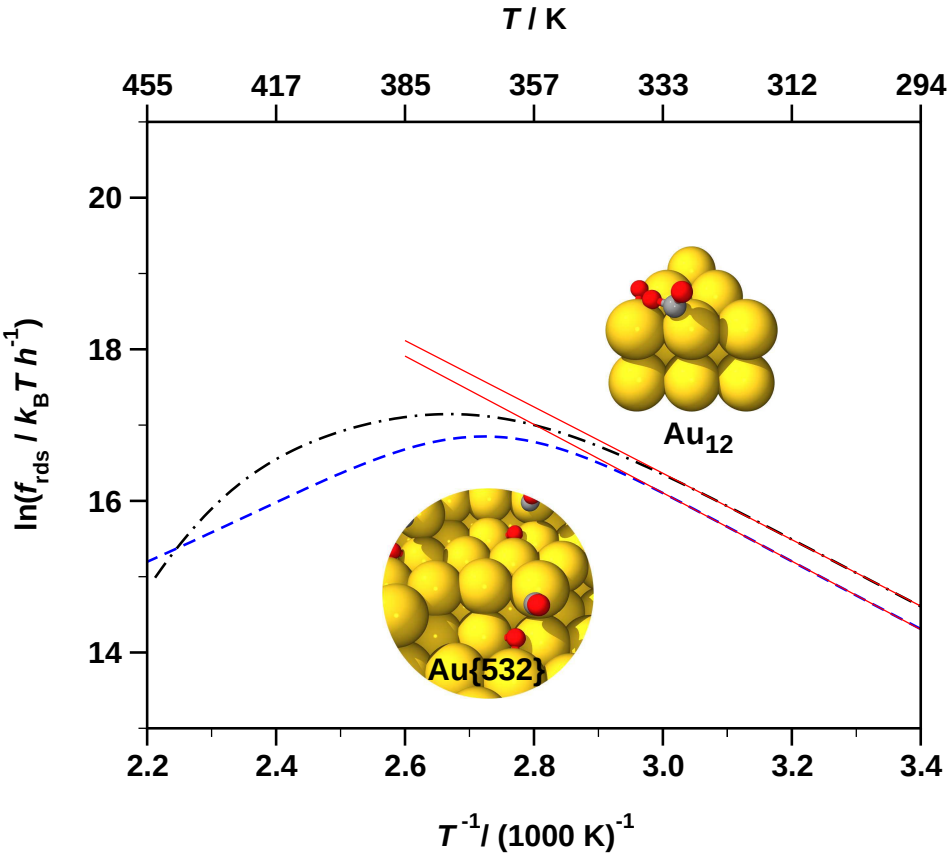

Fig. 4. Arrhenius plot of the rds turnover frequency f_{rds} in $k_{\text{B}}T/h \approx 10^{13}$ s^{-1} for CO oxidation by N_2O on Au$\{532\}$ (blue dashed line) and by O_2 on a Au_{12} cluster (black dash-dotted line) as obtained from the microkinetic model using the DFT transition state structures depicted above [30]. The apparent activation barriers (red solid lines) in the low temperature regime ($T < 350$ K) are shown for ease of comparison with Figure 3, and listed in Table 1.

$$f_{\text{rds}} \approx \frac{k_{\text{B}}T}{h} \frac{K_{\text{CO}*} K_{\text{N}_2\text{O}*} p_{\text{CO}} p_{\text{N}_2\text{O}}}{(1 + K_{\text{CO}*} p_{\text{CO}})(1 + K_{\text{N}_2\text{O}*} p_{\text{N}_2\text{O}})} \exp\left[-\frac{E_a[\text{rds}] - T(S_{\text{CO(g)}} + S_{\text{N}_2\text{O(g)}})}{RT} \right], \tag{8}$$

where $K_{\text{CO}*}$ and $K_{\text{N}_2\text{O}*}$ are given in (7). The required activation and adsorption energies for the Au$\{532\}$ surface are provided in Table 1 and the temperature dependent gas phase entropies are interpolated using data from Ref. [36].

Figure 4 shows the temperature dependence of the turnover frequency f_{rds}, for the rds of CO oxidation by N_2O on Au$\{532\}$. We found f_{rds} follows an Arrhenius-like behavior in the low temperature regime ($T < 350$ K). However, at higher temperatures the turnover frequency decreases with increasing temperature, with an apex at $T \approx 360$ K.

When using O_2 instead of N_2O to oxidize CO, we may again assume a Langmuir–

Hinshelwood mechanism, so that the elementary steps for (R2) may be written as

$$\mathrm{CO(g)} + * \rightleftarrows \mathrm{CO}* \tag{R2a}$$
$$\mathrm{O_2(g)} + {}^{\text{☼}} \rightleftarrows \mathrm{O_2}^{\text{☼}} \tag{R2b}$$
$$\mathrm{CO}* + \mathrm{O_2}^{\text{☼}} \xrightarrow{\text{rds}} \mathrm{CO_2}* + \mathrm{O}^{\text{☼}} \tag{R2c}$$
$$\mathrm{CO}* + \mathrm{O}^{\text{☼}} \Rightarrow \mathrm{CO_2(g)} + * + {}^{\text{☼}} \tag{R2d}$$

where " * " and " ☼ " denote active sites for CO and O_2 respectively, on the Au particle.

Since O_2 is known not to dissociate spontaneously on gold nanoparticles [46], we assume CO is oxidized directly by O_2 (R2c), as discussed in Refs. [30, 47]. We further assume (R2c) is the rate determining step, so that (R2d) occurs relatively quickly. This is justified in the case of high CO coverages, since CO_2 will quickly desorb from the surface.

To model the gold nanoparticle corner sites for reaction (R2c), we have used the Au_{12} cluster model described in Ref. [30]. As seen in Table 1, such a model yields much higher adsorption energies, particularly for O_2. This is necessary to correctly model (R2c) on gold nanoparticles. As shown in the upper inset of Figures 4, the transition state for (R2d) on the Au_{12} cluster model has the O_2 molecule strongly adsorbed on the corner site, while CO is adsorbed on the edge.

Again employing our microkinetic model, f_{rds} for (R2) may be approximated by

$$f_{\text{rds}} \approx \frac{k_{\text{B}}T}{h} \frac{K_{\text{O}_2{}^{\text{☼}}} K_{\text{CO}*} p_{\text{O}_2} p_{\text{CO}}}{(1 + K_{\text{O}_2{}^{\text{☼}}} p_{\text{O}_2})(1 + K_{\text{CO}*} p_{\text{CO}})} \exp\left[-\frac{E_a[\text{rds}] - TS_{\text{CO(g)}}}{RT}\right], \tag{9}$$

where $K_{\text{CO}*}$ and $K_{\text{O}_2{}^{\text{☼}}}$ are given in (7). The necessary activation and adsorption energies for the Au_{12} cluster model are provided in Table 1 and the temperature dependent gas phase entropies are interpolated using data from Ref. [36].

The temperature dependence of f_{rds} for CO oxidation by O_2 on Au_{12} is shown in Figure 4. We again found f_{rds} has an Arrhenius behavior in the low temperature regime ($T < 350$ K). As with N_2O, we found at higher temperatures the turnover frequency decreases with increasing temperature, with an apex at $T \approx 370$ K.

4 Discussion

Table 3 shows the overall trend in apparent activation energies for the reactions measured on Catalysts A, B and C. First, there is a clear size dependence trend from large gold particles with less reactivity to the significantly more reactive smaller

Table 3
Apparent activation energies in kJ mol^{-1} for CO and H_2 oxidation by O_2 and N_2O, with an uncertainty of ± 2 kJ mol^{-1}. Theoretical values obtained using the microkinetic model in the low temperature regime are also provided in parentheses for Catalyst A.

E_a / kJ mol^{-1}	Catalyst A	Catalyst B	Catalyst C
CO + $1/2$ O_2	36 (36.4)	38	60
CO + N_2O	37 (37.5)	40	60
H_2 + $1/2$ O_2	38	38	61
H_2 + N_2O	39	40	60

ones for all the reactions studied. Second, there is very little difference in the apparent overall activation barrier for CO or H_2 oxidation, irrespective of the oxidizing agent used. This is seen for both experimental and theoretical apparent activation barriers, which are in quantitative agreement for Catalyst A ($d < 5$ nm), in the low temperature regime ($T < 350$ K), as shown in Table 3. However, there is little correlation between the experimental reaction rate and theoretical turnover frequency for the larger Catalyst C. This may be expected, as for larger Au nanoparticles ($d >$ 10 nm), the bulk gold properties may begin to dominate, so that a cluster-based theoretical model is no longer applicable.

Clearly it would be desirable to get a direct comparison between measured rates and calculated turnover frequencies. However, such a comparison requires atomic resolution characterisation of the particles in question. Given the large dispersity in particle size for our catalysts we are unable to provide such experimental detail. However, it should be born in mind that the trends for the theoretical turnover frequency should match those of the experimental rate, as shown in Table 3.

We shall first focus on CO oxidation using N_2O according to (R1). From the preliminary investigations it may be concluded that in the absence of a reducing agent, the dissociation of N_2O is inhibited. This may be accounted for by the very weak Au–N_2O bond which leads to rapid desorption of N_2O [31]. However, this reaction changes the overall entropy of the system only slightly, since one diatomic and one triatomic species both adsorb and desorb from the surface in (R1). This means that although there is only a small N_2O coverage, for high CO coverage experiments the reaction rate should be significant. On the other hand, as seen in Figure 4, at higher temperatures ($T > 350$ K) CO begins to desorb from the surface and the turnover frequency begins to decrease at higher temperatures ($T > 360$ K). We were unable to verify this experimentally since we found gold particle sintering began to occur in this temperature range, as shall be discussed later.

For the case of CO oxidation by O_2 according to (R2), there is a significant loss of entropy in the overall reaction, as three diatomic species adsorb, but two triatomic species desorb. Thus a high O_2 adsorption energy is required for the reaction rate to

be significant. As this is the case for small gold nanoparticles and the Au_{12} cluster model for a corner site, we employ this model for (R2). Even so, we find at higher temperatures ($T > 370$ K) the reaction rate decreases significantly as both O_2 and CO begin to desorb from the gold nanoparticle. This may be seen in the reaction rate plots for CO oxidation by O_2 on Catalyst B, shown in Figure 3. Here, the reaction rate begins to flatten at about 370 K, in agreement with the theoretical turnover frequency shown in Figure 4.

Besides the activity, stability is the next most important property of an industrial catalyst. With a view on the gold loading of the catalysts used, noted in Table 2, it seems clear that small particles with a high loading are more likely to sinter than with lower loadings. One reason for this is that due to the low melting point of gold [48, 49] or quasi-melting [50], gold particles already become mobile at only slightly elevated temperatures. The larger the particles at a constant loading are, the fewer particles are on the support, and the larger is the distance to their nearest neighbor.

Figure 2 illustrates the sintering for different gold particle sizes during the pretreatment, when comparing image (i) with image (ii), as well as during the activity measurements. Since the activity measurements were performed in a sequence (as described above), the change in particle size may be related to 40°C more in heat applied than for the catalytic reactions driven on Catalyst B.

Catalyst A was not heated more than the pretreatment required. This means that the sintering on this catalyst is related only to how the reactions proceeded. Across the general observations published regarding CO oxidation on TiO_2 supported gold using O_2 as an oxidizing agent, sintering of nanoparticulate gold has not been reported. Gold nanoparticles have also been found to be a stable catalyst in the presence of H_2 and H_2O [51]. This suggests that the sintering observed on Catalyst A is related to the supply of N_2O. In contrast, the particles of Catalyst C did not significantly sinter, even though the maximum temperature was 80°C higher than the temperature of the pretreatment.

5 Conclusions

We have investigated two different reactions on three TiO_2 supported gold catalysts with two different oxidizing agents. Experimental results for CO oxidation on Catalysts A and B agree with both our theoretical model and the literature, following the d^{-3} trend advocated by Nørskov *et al.* [6]. However, for Catalyst C we found more bulk-like behavior.

Based on our theoretical model, we find oxidizing CO by N_2O involves a CO–O transition state, with atomic O adsorbed on the gold B5 sites and CO on the corners.

On the other hand, CO oxidation by molecular O_2 occurs via a different reaction pathway, which instead involves a meta-stable intermediate CO–O_2. In this case, O_2 is strongly adsorbed on gold corner sites while CO is adsorbed on the nearby edge sites (*cf.* Figure 2).

However, although the two oxidizing agents used proceeded via *different* reaction pathways on *different* active sites, the apparent overall activation barriers obtained from both theory and experiment were found to be the *same*. From experiment, we found that H_2 and CO oxidation proceed similarly, with common activation barriers and rate enhancements when comparing oxidizing agents.

Additionally, from our TEM analysis we conclude that N_2O oxidation may promote sintering of Au nanoparticles on TiO_2, since significant sintering has not been found for CO and H_2 oxidation on gold nanoparticles using O_2 [27, 51].

Acknowledgments

The authors gratefully acknowledge support in the form of catalysts provided by Project AuTEK. We also thank F. B. Grumsen for assistance with taking TEM images, and T. Bligaard for useful discussions. G. Walther and D. J. Mowbray also acknowledge financial support from NABIIT. The Center for Atomic-scale Materials Design is funded by the Lundbeck Foundation. The authors also acknowledge support from the Danish Center for Scientific Computing through grant HDW-1103-06.

References

[1] B. Hammer, J. K. Nørskov, Nature 376 (1995) 238–240.
[2] M. Haruta, T. Kobayashi, H. Sano, N. Yamada, Chem. Lett. (1987) 405–408.
[3] A. S. K. Hashmi, G. J. Hutchings, Angew. Chem. 45 (2006) 7896.
[4] G. C. Bond, D. T. Thompson, Catal. Rev.–Sci. Eng. 41 (1999) 319–388.
[5] G. C. Bond, C. Louis, D. T. Thompson, Catalysis by Gold, 1st Edition, Imperial College Press, 2006.
[6] B. Hvolbæk, T. V. W. Janssens, B. S. Clausen, H. Falsig, C. H. Christensen, J. K. Nørskov, Nano Today 2 (2007) 14–18.
[7] D. E. Starr, S. K. Shaikhutdinov, H.-J. Freund, Top. Catal. 36 (2005) 33–41.
[8] H.-J. Freund, Catal. Today 117 (2006) 6–17.
[9] M. Valden, X. Lai, D. W. Goodman, Science 281 (1998) 1647–1649.
[10] M. S. Chen, D. W. Goodman, Science 306 (2004) 252–255.
[11] T. V. W. Janssens, A. Carlsson, A. Puig-Molina, B. S. Clausen, J. Catal. 240 (2006) 108–113.
[12] C. Xu, J. Su, X. Xu, P. Liu, H. Zhao, F. Tian, Y. Ding, J. Am. Chem. Soc. 129 (2007) 42–43.

[13] C. Xu, X. Xu, J. Su, Y. Ding, J. Catal. 252 (2007) 243–248.
[14] R. J. H. Grisel, B. E. Nieuwenhuys, Catal. Today 64 (2001) 69–81.
[15] M. Mavrikakis, P. Stoltze, J. K. Nørskov, Catal. Lett. 64 (2000) 101–106.
[16] Z.-P. Liu, P. Hu, A. Alavi, J. Am. Chem. Soc. 124 (2002) 14770–14779.
[17] N. Lopez, J. K. Nørskov, J. Am. Chem. Soc. 124 (2002) 11262–11263.
[18] N. Lopez, T. V. W. Janssens, B. S. Clausen, Y. Xu, M. Mavrikakis, T. Bligaard, J. K. Nørskov, J. Catal. 223 (2004) 232–235.
[19] T. V. W. Janssens, B. S. Clausen, B. Hvolbæk, H. Falsig, C. H. Christensen, T. Bligaard, J. K. Nørskov, Top. Catal. 44 (2007) 15–26.
[20] B. E. Solsona, T. Garcia, C. Jones, S. H. Taylor, A. F. Carley, G. J. Hutchings, Appl. Catal. A-Gen. 312 (2006) 67–76.
[21] D. T. Thompson, Top. Catal. 38 (2006) 231–240.
[22] R. D. Waters, J. J. Weimer, J. E. Smith, Catal. Lett. 30 (1994) 181–188.
[23] S. Ivanova, C. Petit, V. Pitchon, Appl. Catal. A-Gen. 267 (2004) 191–201.
[24] S. Ivanova, C. Petit, V. Pitchon, Gold Bull. 39 (2006) 3–8.
[25] C. H. Christensen, B. Jorgensen, J. Rass-Hansen, K. Egeblad, R. Madsen, S. K. Klitgaard, S. M. Hansen, M. R. Hansen, H. C. Andersen, A. Riisager, Angew. Chem. 45 (2006) 4648–4651.
[26] M.-C. Daniel, D. Astruc, Chem. Rev. 104 (2004) 293–346.
[27] G. Walther, G. Jones, S. Jensen, U. J. Quaade, S. Horch, Catal. Today(accepted).
[28] M. Haruta, Catal. Today 36 (1997) 153–166.
[29] J. A. van Bokhoven, C. Louis, J. T. Miller, M. Tromp, O. V. Safonova, P. Glatzel, Angew. Chem.-Ger. Ed. 118 (2006) 4767–4770.
[30] H. Falsig, B. Hvolbæk, I. S. Kristensen, T. Jiang, T. Bligaard, C. H. Christensen, J. K. Nørskov, Angew. Chemie 47 (2008) 4835–4839.
[31] A. C. Gluhoi, M. A. P. Dekkers, B. E. Nieuwenhuys, J. Catal. 219 (2003) 197–205.
[32] L. M. Molina, B. Hammer, Phys. Rev. B 69 (2004) 155424.
[33] U. J. Quaade, S. Jensen, O. Hansen, J. Appl. Phys. 97 (2005) 44906.
[34] http://www.mintek.co.za.
[35] http://www.gold.org.
[36] D. R. Lide, Handbook of Chemistry and Physics, 87th Edition, CRC-Press, 2006–2007.
[37] http://wiki.fysik.dtu.dk/dacapo.
[38] D. Vanderbilt, Phys. Rev. B 41 (1990) 7892–7895.
[39] B. Hammer, L. B. Hansen, J. K. Nørskov, Phys. Rev. B 59 (1999) 7413–7421.
[40] J. K. Nørskov, J. Rossmeisl, A. Logadottir, L. Lindqvist, J. R. Kitchin, T. Bligaard, H. Jonsson, J. Phys. Chem. B 108 (2004) 17886–17892.
[41] S. Kurth, J. P. Perdew, P. Blaha, Int. J. Quantum Chem. 75 (1999) 889–909.
[42] J. H. Noggle, Physical Chemistry, 3rd Edition, Harper Collins, 1996.
[43] B. E. Nieuwenhuys, A. C. Gluhoi, E. D. L. Rienks, C. J. Weststrate, C. P. Vinod, Catal. Today 100 (2005) 49–54.
[44] Z.-P. Liu, X.-Q. Gong, J. Kohanoff, C. Sanchez, P. Hu, Phys. Rev. Lett. 91 (2003) 2661021–2661024.

[45] M. Boudart, G. Djéga-Mariadassou, Kinetics of heterogeneous catalytic reactions, Princeton University Press, 1984.
[46] J. K. Nørskov, T. Bligaard, A. Logadottir, S. Bahn, L. B. Hansen, M. Bollinger, H. Bengaard, B. Hammer, Z. Sljivancanin, M. Mavrikakis, Y. Xu, S. Dahl, C. J. H. Jacobsen, J. Catal. 209 (2002) 275–278.
[47] L. M. Molina, B. Hammer, Appl. Catal. A-Gen. 291 (2005) 21–31.
[48] P. Buffat, J. P. Borel, Phys. Rev. A 13 (1976) 2287–2298.
[49] H. Sykes, E. Charles, F. J. Williams, M. S. Tikhov, R. M. Lambert, J. Phys. Chem. B 106 (2002) 5390–5394.
[50] P. M. Ajayan, D. L. Marks, Phys. Rev. Lett. 60 (1988) 585–587.
[51] P. Landon, J. Ferguson, B. E. Solsona, T. Garcia, S. Al-Sayari, A. F. Carley, A. A. Herzing, C. J. Kiely, M. Makkee, J. A. Moulijn, A. Overweg, S. E. Golunski, G. J. Hutchings, J. Mater. Chem. 16 (2006) 199–208.